



*Dottorato di ricerca*

In

**INGEGNERIA STRUTTURALE,  
GEOTECNICA E RISCHIO SISMICO  
XXXIII CICLO**

**Earthquake Early Warning and  
Preparatory Phase Detection through the  
use of Machine Learning Techniques**

*Antonio Giovanni Iaccarino*

**Relatore**

Prof. Matteo Picozzi

**Coordinatore**

Prof. Luciano Rosati

## Index

List of Figures.....	4
List of Tables.....	5
<b>1. Introduction</b> .....	<b>6</b>
1.1. Earthquake Early Warning.....	6
1.2. Earthquake preparatory phase.....	9
1.3. Machine learning.....	10
1.4. Thesis Content.....	12
<b>2. Onsite Earthquake Early Warning: Predictive Models for Acceleration Response Spectra Considering Site Effects</b> .....	<b>13</b>
2.1. Introduction.....	14
2.2. Dataset and pre-processing.....	16
2.3. Method: mixed-effect regression.....	18
2.4 Results.....	20
2.4.1 Model calibration.....	20
2.4.2 Model validation: Leave-one-out cross-validation.....	26
2.4.3 Analysis of random effect vs. period.....	27
2.4.4 Implications of random effects for an onsite EEW decision alert system.....	29
2.5 Conclusion.....	32
<b>3. Earthquake Early Warning System for Structural Drift Prediction using Machine Learning and Linear Regressors</b> .....	<b>33</b>
3.1 Introduction.....	34
3.2 Datasets and methods.....	36
3.2.1 Datasets.....	36
3.2.2 P-wave features.....	37
3.2.3 Case studies.....	38
3.2.4 Linear least square regression.....	39
3.2.5 Machine Learning regressors.....	39
RF regressor.....	39
GB regressor.....	40
SVM regressor.....	40
KNN regressor.....	40
Validation process.....	40
3.3 ANX and SRC analysis.....	41
3.3.1 Least Square Regression models.....	41
3.3.2 Machine Learning Regression.....	43
3.4 Japanese dataset analysis.....	47

## Index

3.4.1	Least Square Regression Laws .....	47
3.4.2	Machine Learning Regression.....	48
3.4.3	Residual analysis.....	49
3.5	US dataset application.....	53
3.5.1	Least Square Regression Laws .....	53
3.5.2	Bias analysis.....	54
3.5.3	Bias correction.....	56
3.6	Conclusions.....	57
<b>4.</b>	<b>Forecasting the Preparatory Phase of Induced Earthquakes by Recurrent Neural Network .....</b>	<b>59</b>
4.1.	Introduction.....	60
4.2.	Features.....	65
4.2.1.	Features computation and general working outline.....	65
4.2.2.	Duration of event groups and inter-event time .....	65
4.2.3.	Moment Magnitude and Moment rate.....	66
4.2.4.	b-value and completeness magnitude $M_c$ .....	66
4.2.5.	Fractal Dimension.....	66
4.2.6.	Nearest-neighbor distance, $\eta$ , analysis .....	67
4.2.7.	Shannon's Information Entropy .....	67
4.3.	Methods .....	68
4.3.1.	Recurrent Neural Networks and ML layers .....	68
4.3.2.	Step-by-step description of data-analysis by RNN .....	70
4.4	Results .....	71
4.4.1	Observing seismicity occurrence from features perspective .....	71
4.4.2	RNNs tuning trough cross-validation on a training dataset .....	73
4.4.3	Training RNN1 and RNN2 .....	74
4.4.4	Testing RNN1 and RNN2.....	76
4.4.5	Conceptualization of an alert algorithm.....	76
4.5	Discussion .....	78
<b>5.</b>	<b>Conclusions .....</b>	<b>79</b>
<b>6.</b>	<b>References.....</b>	<b>81</b>
	Appendix.....	94
	Work done in STELTEL S.R.L.....	94
	<b>Curriculum vitae.....</b>	<b>95</b>

## List of Figures

Figure 2-1: Map of the events and accelerometric stations used in the study .....	17
Figure 2-2: Example of seismic waveforms and RSA .....	18
Figure 2-3: RSA (cm/s <sup>2</sup> ) for the period of 0.5 s vs. the Pd (cm) . .....	21
Figure 2-4: Normalized residuals for Pd for the periods T = 0.15 s, T = 0.5 s, and T = 1.5 s.....	23
Figure 2-5: H/V ratio computed for the stations: NCR; FOC; T1212; and T1221 .....	24
Figure 2-6: Normalized, and corrected residuals for Pd for the period T equal to 0.3 s.....	24
Figure 2-7: Normalized residuals for Pd considering the EC8 classes for nine periods.....	25
Figure 2-8: Comparison between standard deviation of the residuals with and without correction.....	27
Figure 2-9: $\delta S2S^{Pd-Sta}$ vs. period (T) for each class.....	28
Figure 2-10: The ‘normalized’ curves clusters obtained by the K-means clustering.....	28
Figure 2-11: EEW performances with and without station correction terms .....	30
Figure 3-1: Map of the dataset used in the study .....	36
Figure 3-2: Dr versus Pd of the ANX dataset for three different windows .....	41
Figure 3-3: Predicted Dr versus Real Dr for three different windows for ANX and SRC datasets.....	45
Figure 3-4: Predicted Dr versus Real Dr of the test set for the Japanese dataset for 3s windows .....	48
Figure 3-5: Decomposition of the residuals of Dr prediction for Japanese test set.....	52
Figure 3-6: Decomposition of the residuals of Dr prediction for US dataset using Japanese model.....	55
Figure 4-1: Schematic illustration of the processes anticipating and following a large earthquake .....	61
Figure 4-2: Map of the catalogue of The Geysers .....	63
Figure 4-3: Overview of the RNN-based preparatory phase prediction .....	65
Figure 4-4: Distribution of events before and after the first M4 earthquake.....	72
Figure 4-5: Standardized features of the training M4 series .....	73
Figure 4-6: RNN1 and RNN2 predictions and performances on training and testing sets.....	75
Figure 4-7: Application of RNN1 and RNN2 combined into a prototype of alert system. ....	77

## List of Tables

Table 2-1: Acronyms and Symbols used in this work. ....	19
Table 2-2: Coefficients of Eqs. (3, 4, 5, and 6) for all considered periods. ....	20
Table 2-3: $\sigma$ and $\sigma_{ss}$ for Eqs. (3, 4, 5, and 6) for the considered periods.....	21
Table 3-1: Dataset summary .....	37
Table 3-2: Least square regression results, ANX dataset .....	42
Table 3-3: Least square regression results, SRC dataset .....	43
Table 3-4: ML regression results, ANX dataset.....	46
Table 3-5: ML regression results, SRC dataset .....	46
Table 3-6: Least square regression results, Japanese dataset .....	47
Table 3-7: ML regression results, Japanese dataset.....	49
Table 3-8: Least square regression results, complete dataset .....	53
Table 3-9: $R^2$ scores for US dataset corrected drift prediction.....	57

# 1. Introduction

My PhD project is classified as “Innovative PhD with industrial characterization” (“*Dottorati Innovativi con caratterizzazione industriale*”) in the national project PON RI 2014-2020 (*Programma Operativo Nazionale FSE-FESR Ricerca e Innovazione*). The principal characteristic of these kind of PhDs is the fact that the research is done in collaboration with a private company (in my case, STELTEL S.R.L.) and a foreign university (in my case, the ISTERre at *Université Grenoble Alpes* in Grenoble, France). The aim of the partnership is development of scientific products of industrial interest.

Earthquakes represent one of the major natural hazards for many countries (e.g., Italy, Japan, California, etc..) affecting the life of many people from small villages to big cities. The main topic of my thesis concerns the reduction of seismic risk. I developed this topic following two ways, the Earthquake Early Warning (EEW), and the detection of the preparatory phase for large events.

The EEW systems represent a practical way to mitigate the seismic risk of cities and infrastructures, to reduce human losses, and to increase the people resilience. They are based on the fast detection and characterization of the upcoming strong ground motion from an earthquake. Then, these systems are able to make some automatic actions such as alerting the population, stopping trains, etc.

The preparatory phase of the earthquakes is a topic still on debate in literature. Some authors state that the main earthquakes are triggered by cascading processes that are completely stochastic. Other authors think that, before a major earthquake, there are seismic and aseismic processes that load stress on the fault and that can be detected. The last hypothesis leads to the possibility of the earthquake predictability that would bring to a strong reduction of the seismic risk.

To achieve my results, I chose to explore the use of machine learning (ML) techniques. These methods have a long history, but their use has been limited for many years due to the lack of computational power. In the last decades, the use of ML methods is exponentially incremented in all the scientific field and in the seismology itself.

## 1.1. Earthquake Early Warning

The first abstract idea for an EEW system was conceived by Cooper (1868), his idea was to install a sort of detector for earthquake near the fault able to send a warning message through telegraph cables to the city of San Francisco where an “Earthquake bell” would have alerted the population. Despite this, the first implementation of EEW was the UrEDAS (Urgent Earthquake Detection and Alarm System; Bito and Nakamura, 1986; Nakamura and Saita, 2007) in Japan, this automated system is able to stop the train when a dangerous event is detected by the seismic network along the railway preventing possible derailments.

The idea of EEW is based on the differential between the velocities of the involved phenomena. In fact, the main phases of the earthquake, P and S waves, travel at about 6 km/s and 3.3 km/s respectively while any alerting system, from telegraph to 5G, brings the message at (nearly) the speed of light. Moreover, P-waves are faster but less destructive than the S-waves. So, an EEW system can analyze seismic data in real-time to detect and characterize the earthquake size using the first seconds of P-wave signals. Generally, by these pieces of information, an EEWS attempts to predict the ground motion parameters (e.g., Peak Ground Acceleration, PGA) at a specified target or a region anticipating the arrival of destructive waves.

## 1. Introduction

EEW systems have seen rapid development only over the last decades, mainly due to the improvements in telecommunication, data storage, and computer technologies. It is worth noting that these technological advances have been accompanied by significant scientific progress, and EEWSs are becoming increasingly precise and efficient. Several countries have built or are testing EEWS, for instance: California, Japan, Italy, Mexico, and China (Allen and Kanamori, 2003; Hoshiba et al., 2008; Espinosa-Aranda et al., 2009; Peng et al., 2011; Satriano, Elia, et al., 2011).

Following Satriano, Wu, et al. (2011), we can divide the EEW systems into two main families: onsite and regional systems. The onsite approach uses a single station, or a seismic network, installed near the target. Whereas, in the regional systems the seismic network is placed near a seismogenic zone, normally far from the target area to protect. Furthermore, onsite systems use only P-waves information to directly predict ground motion through empirical scaling laws. On the other hand, regional EEWSs analyze P-waves and S-waves information from stations close to the epicenter estimating the source parameters and then, predicting the ground motion at the target using GMPEs (Ground Motion Prediction Equation).

Allen and Melgar (2019) made a very comprehensive study on the regional EEW system by identifying three main approaches: point-source, finite-fault, and ground-motion driven.

In the first approach, as the name suggests, the earthquake is located as a point-source. The main goal of this kind of EEW systems is to alert the target as quick as possible, but there are two main limitations to this objective. The first one is that it is not possible to reduce the alert time at zero, and so there will be always an area that will be hit by the earthquake before the alert (the blind zone). In particular, Kuyuk and Allen (2013) showed how the blind zone is strictly dependent by the network density, the denser the network, the smaller the blind zone. The other limit is that the uncertainty of the magnitude estimation increases with the decreasing of the time-window. This is mainly due to the fact that for larger magnitude events, the rupture duration is in the order of seconds, so a window too small is not able to provide enough information on the source size (Yamada and Mori, 2009; Minson et al., 2018).

An example of this approach is the PRESTo platform (Satriano, Elia, et al., 2011). This system automatically detects the P phases arrivals using FilterPicker (Lomax et al., 2012), then the events is declared if a certain number of arrivals are coherent in time and space with a common seismic source. The location is done using the RTLoc technique (Real Time Location, Satriano et al., 2008) that exploits both the arrivals data and the intrinsic information given by the not-triggered stations. At the same time, PRESTo estimates the magnitude in an evolutionary way using the RTMag method (Real Time Magnitude, Lancieri and Zollo, 2008). This technique computes the magnitude using a Bayesian formulation of the empirical relation with Peak of Displacement (Pd) computed on P and S phases (when available), and the hypocentral distance.

Other point-source techniques have as main objective the precise characterization of the on-going earthquake. Tarantino et al. (2019) used a Bayesian approach to compute the focal mechanism of the earthquake using as input the real-time estimation of peak of acceleration (Pa), velocity (Pv), and displacement (Pd) measured on the P-wave at the stations of a network. The same real-time P-wave features can be used to compute the logarithm of P-wave amplitude curves (LPDT; Colombelli and Zollo, 2015; Nazeri et al., 2017). Then, these latter curves can be used to determine seismic moment, magnitude, rupture duration, source radius and stress drop of the upcoming earthquake.

While these simple systems are pretty fast and accurate to alert the targets for moderate to strong events, they tend to fail for very strong events. In these cases, indeed, the point-source approximation is no more reliable to describe the event, and this leads to an underestimation of the ground motion (Hoshiba and Ozaki, 2014; Chung et al., 2020). To mitigate these kind of problems, new approaches try to estimate in real-time the geometry and size of the source (Allen and Melgar, 2019). A good example is the FinDer algorithm (Maren Böse et al., 2012; Böse et al., 2018) that is able to retrieve the strike and the linear size of

## 1. Introduction

the source interpolating the recorded ground motion. Other techniques use real-time high-rate GPS data to invert the static-slip directly on the fault (Grapenthin et al., 2014; Minson et al., 2014; Crowell et al., 2016). Some studies demonstrated that these techniques do not suffer of magnitude saturation (Ohta et al., 2012; Wright et al., 2012) and can provide ground motion predictions more reliable than point-source algorithms (Colombelli et al., 2013).

Finally, the ground-motion driven algorithms directly predict the ground motion at the target without inferring anything about the source. This approach is relatively recent (Hoshiaba and Aoki, 2015; Kodera et al., 2018) and its basic idea is to use the ongoing ground motion data to predict the same in the next 20s. In particular, PLUM (Propagation of Local Undamped Motion, Hoshiaba and Aoki, 2015) uses data assimilation to create a dense map of real-time intensity and then uses the radiative transfer theory to forecast to propagation of the energy. The main advantage of this approach is the fact that it implicitly considers the extension of the source from its radiation field. Moreover, it can also handle multiple contemporary events.

The onsite EEW systems are usually simpler than the regional ones because they directly predict the ground motion at the site to protect exploiting P-wave amplitude measures and empirical models. In the last decades, different techniques concerning the onsite EEWS have been proposed. Wu and Kanamori (2005, 2008) firstly proposed the use of P-wave parameters such the peak of displacement ( $P_d$ ) and the predominant period ( $\tau_c$ ) measured on the first 3 seconds of P-wave, predicting the moment magnitude ( $M_w$ ) from  $\tau_c$  and the Peak of Ground Velocity (PGV) using  $P_d$ . Colombelli et al. (2015) use a continuous fuzzy variable that combines peak of acceleration ( $P_a$ ), velocity ( $P_v$ ), and  $P_d$  measured on the entire P-wave. This variable is an increasing step-like function, and it is used to directly declare the alert when a threshold is overcome. The method usually declares the with an alert time greater than 3s.

In Caruso et al. (2017), the authors measure  $P_d$  and the dominant period ( $\tau_c$ ) on a window of up to 3 seconds of P-wave to predict PGV (Peak Ground of Velocity) and then classify the event in a range of magnitude and distance. Brondi et al. (2015) considered the parameter integral of the squared velocity ( $IV^2$ ) measured on P-wave window of maximum length equal to 3s. This study showed that  $IV^2$  well correlates with both the peak ground velocity and the Housner Intensity, with the latter being recognized by engineers as a reliable proxy for damage assessment.

Spallarossa et al. (2019) introduced in the onsite earthquake early warning (EEW) a partially non-ergodic perspective from the site effects point of view. These authors showed, indeed, that by using  $P_d$  and  $IV^2$  and partially non-ergodic models the accuracy of the PGV predictions can be improved with respect to ergodic models derived for other regions of the world. Since being site-specific is an inherent characteristic of onsite EEW applications, the improved accuracy and precision of the PGV predicted for a target protection translate in a better customization of the alert protocols for automatic actions.

Moreover, many studies presented engineering application of EEW systems (Iervolino et al., 2007; Cheng et al., 2014; Ptilakis et al., 2016; Cremen and Galasso, 2021). These studies used a particular type of EEW procedure: the Performance-Based EEW (PBEEW; Grasso, 2005; Iervolino, 2011). This procedure can be seen as a real-time extension of the PBEE (Performance-Based Earthquake Engineering; Cornell and Krawinkler, 2000). Here, indeed, the earthquake potential is computed using the real-time estimation of magnitude and distance provided by an EEW system (Iervolino et al., 2006). Since the PBEEW systems need the location and the characterization of the event but also a good estimation of the ground motion at the target, they usually are based on a hybrid network that uses both regional and onsite information (Iervolino et al., 2006; Iervolino, 2011; Ptilakis et al., 2016).

In my PhD, I studied onsite EEW procedures for the prediction of parameters of engineering interest. In the first work (Chapter 2), I propose the real-time prediction of the response spectra of acceleration (RSA) at nine different periods using  $P_d$  and  $IV^2$  on 3s window. Here, I used a mixed-effect

## 1. Introduction

regression to consider site-effect correction terms for each station. In the second work (Chapter 3), I proposed an onsite single station EEW methodology to directly predict the structural drift using data recorded by in-building sensors from Japanese and US structures. In this work, I compared linear least square regression models, non-linear machine learning techniques using, as inputs, three P-wave parameters  $P_d$ ,  $IV^2$ ,  $ID^2$  (Integral of squared Displacement) measured at 1s, 2s, and 3s.

### 1.2. Earthquake preparatory phase

The second topic of research has been the earthquake preparatory phase. This is usually represented by a cluster of seismicity that precedes and triggers a large event. These events are called foreshocks and different studies (Dieterich, 1978; Jones and Molnar, 1979; Abercrombie and Mori, 1996) have shown that they are often present before large magnitude events. However, since the foreshocks and the precursory patterns are non-systematic, the background physical processes generating foreshocks and the preparatory phase is not fully understood yet and matter of debate (Kanamori, 1981).

Two main contrasting models have been proposed concerning foreshocks generations. According to some authors (Das and Scholz, 1981; Ohnaka, 1992; Mignan, 2012), foreshocks are related to a tectonic loading process associated to aseismic slip, which represents a deviation from the normal behavior of seismicity (Mignan, 2014). This model would support the existence of a preparatory phase for large earthquakes, leaving us with the hope that in future earthquakes will be predictable.

By contrast, for other authors (Helmstetter and Sornette, 2003; Felzer et al., 2004) foreshocks result from a triggering process that is part of the normal behavior of seismicity (i.e., following the concept of Self-Organized Criticality), for which events can cascade into a larger one without any clear, yet, background driving process. The key practical aspect of this model is that the probability of a large event in a short period (e.g., one week) following to the occurrence of foreshocks is very low, and therefore of limited use.

Over the last decade, significant advances have been obtained in this research field thanks to the availability of high-resolution seismic catalogs, which resulted from efforts done by the seismological community in increasing the number of dense seismic networks deployed nearby active faults and in the development of advanced event detection techniques.

A recent, systematic review on the initiation of large earthquakes (Kato and Ben-Zion, 2021) has highlighted that their generation is the result of complex, multiscale processes where the tectonic environment and external factors (e.g., natural and/or anthropogenic inputs that impact on the local stress-field) interact. The resultant integrated generation model proposes a progressive localization of shear deformation around a rupture zone, which evolves into a final rapid loading (i.e., generating foreshocks) of a localized volume nearby the hypocenter of the major dynamic rupture. Such kind of process might be universal. Indeed, similar patterns of damage evolution across a fault zone have been found also studying the temporal and spatial distribution and characteristics of acoustic emissions during triaxial tests on rock samples (Dresen et al., 2020).

Like the last one, other studies based on laboratory tests shed light on what happens before a rupture. Goebel et al. (2013) showed that, in acoustic experiments, the occurrence of an event is not fully stochastic, but it is preceded by a decrease of the b-value indicating that the seismicity tends to self-organize just before an important event. Trugman et al. (2020) demonstrated that in shear cycle experiments both foreshock cascades and aseismic loading are present before the main stick-slip events. Furthermore, in these experiments was no possible to identify any clear and unique pattern in the location of the foreshocks, this indicates a high level of complexity even for this simple and controlled systems. Despite

## 1. Introduction

this complexity, studies like Rouet-Leduc et al. (2017) and Bolton et al. (2019), proved that, using machine learning techniques, it is possible to predict the occurrence of the main slip events in laboratory.

During my PhD, we developed a machine learning methodology able to identify the preparatory phase of induced events using catalogue data from The Geysers, a geothermal area in California (Chapter 1). This is a very active area with a dense seismic network, so it represents a perfect natural laboratory for such a study. We applied a recurrent neural network on features extracted from catalogue information to detect the preparatory phase. Our results hint the presence of a detectable preparatory phase (from few hours to two days before the main) also for induced events at The Geysers.

### 1.3. Machine learning

Machine learning (ML) techniques are nowadays widely used in all the scientific fields, including seismology. These techniques can easily extract very complex models directly from the data without adding prior model information. There are three main families of ML: classifiers, regressor, and clustering algorithms (Raschka and Mirjalili, 2017). The first two classes are also called supervised ML because they need a training with the labeled input data. The difference between classifiers and regressors is that the label of the former ones refers to discrete values (classes) while the latter ones predict continuous values. Moreover, many ML techniques can be used both as classifiers and as regressors, this is because a continuous label can be seen as a dense series of discrete labels. Finally, the clustering algorithms find the similarities between unlabeled data grouping them in different classes (clusters).

An important class of ML techniques are the Neural Networks (NN). A NN is an ensemble of neurons organized in various layers, each one with a certain number of neurons (also called nodes or units). An artificial neuron is a mathematical function that can be linear or not between input and output, which depends on coefficients whose optimization is done by a training. As example, a fully connected neuron gives as output a linear combination of all the inputs, also adding a bias. When the NN presents a large number of layers, we talk about Deep Learning.

It is important to understand that, despite the final model of a ML technique will be very complex, it will be always a mathematical function and almost completely data driven. So, if training process is well done, the final results will be trustworthy.

Recently, the machine learning techniques have been increasingly used as in seismology as in earthquake forecasting and EEW studies (Kong et al., 2019).

As said in the previous chapter, many studies showed that it is possible to predict main events at laboratory scale using machine learning techniques. As example, Rouet-Leduc et al. (2017) used a random forest classifier to forecast stick-slip failure. On the other hand, Bolton et al. (2019) showed that the use of unsupervised techniques can highlight changes in the micro-events before the events dividing the foreshocks from the background seismicity. Moreover, Corbi et al. (2019) used the gradient boosting to predict the main failure in simulated seismic cycle for a subduction zone at laboratory-scale. Since the growth of these techniques, Johnson et al. (2021) proposed a competition for laboratory earthquake forecasting.

Beyond the laboratories, many applications have been proposed for the forecasting of real earthquakes. Mignan and Broccardo (2020) did a comprehensive review of 77 studies of NN application in earthquake prediction. Despite the interesting results, the authors found that complex models tend to provide similar results as the logistic regression models based on empirical laws such as the Gutenberg-

## 1. Introduction

Richter law (Gutenberg and Richter, 1942, 1956). In the end, the study pointed out that the NNs “so far do not seem to provide new insights into earthquake predictability”.

With the regard of EEW framework, many studies involving ML can be cited. In Kong et al. (2016) and Allen et al. (2019), MyShake smartphone app is presented that is the first example of distributed regional EEW system. The app uses a NN to distinguish seismic events from the normal noise turning each smartphone in a seismic sensor. Then, when an event is detected, the input is sent to a central server that confirms, or not, the event looking at the geographical positions of the ongoing detections. Then, MyShake computes the location and the magnitude using the smartphone data.

In Jozinović et al., (2020) a regional EEW system developed for Central Italy. It uses the continuous raw waveforms from 39 stations as inputs for a deep convolutional NN to predict ground motion parameters in the area. The authors show that the system is able to well predict the ground motion at 10s after the origin time meaning that they can provide useful alerts far from the epicenter. Since the system does not need to locate the event, this should be considered a ground-motion driven algorithm. Despite it is suitable for online application, the method can work only in an off-line configuration, for now.

In Münchmeyer et al. (2021), the authors present TEAM (Transformer Earthquake Alerting Model) that is an all-in-one EEW system able to detect an event, to compute the PGA probability density at the chosen targets and to alert the target where PGA exceeds a given threshold. The method is again based on a deep convolutional NN coupled with an attention based NN, the first analyzes the waveforms from the network in real-time extracting useful features that are fed in input of the second NN that computes the PGA probability densities.

In Böse et al. (2012), the authors present an onsite method that uses the integral of absolute acceleration (IAA), velocity (IAV), and displacement (IAD) computed on the three components (on different windows from 0.25s to 10s), and the station Vs30 (a total of 10 features) as inputs for an ensemble of NN to predict magnitude, distance and PGV. In Hsu et al. (2013), a support vector regressor is used to compute the Peak Ground of Acceleration (PGA) using  $P_a$ ,  $P_v$ ,  $P_d$ ,  $\tau_c$ ,  $IV^2$ , and the cumulative absolute velocity (CAV) all computed on a 3s window.

Other notable works are Mousavi and Beroza (2020a, and 2020b), here the authors use deep neural networks, in different configurations, to locate the event and compute the magnitude using the raw data waveforms from a single station. Nonetheless, these works are not yet developed as EEW techniques since they use both P and S waves information.

In this thesis, we present different application of machine learning techniques. In the first work (Iaccarino et al., 2020b; Chapter 2), we did a clustering analysis using the K-means method on the station correction terms for the RSA prediction. Our aim was to find a correlation with the EC8 site classification of the station finding no clear relation. In Chapter 3, we present a work where we used 4 different machine learning non-linear regressors (Random Forest, Gradient Boost, SVM, KNN) to predict structural Drift from P-wave parameters. In the end, the third work (Picozzi and Iaccarino, 2021; Chapter 1) is based on the use of a Recurrent Neural Network to detect the preparatory phase of induced earthquakes in The Geysers, California.

## 1. Introduction

### 1.4. Thesis Content

In this thesis I present 3 different works developed during the PhD. These three works are already published.

As said, my research has been focused on onsite EEW techniques oriented to the seismic risk reduction for buildings. As matter of fact, in the first work (Iaccarino et al., 2020; Chapter 2), "Onsite earthquake early warning: Predictive models for acceleration response spectra considering site effects" , we presented an EEW method that predict Response Spectra of Acceleration (RSA) at nine different periods from P-wave parameters (i. e.,  $P_d$  and  $IV^2$ ) on 3s window. RSA is a ground motion parameter of particular interest for structural engineers since it better correlates with structural damage than peak parameters such as PGA and PGV (Elenas and Meskouris, 2001). To account for site-effects, we retrieved a partially non-ergodic model using a mixed-effect regression analysis. This procedure helped us to reduce the prediction uncertainty. Finally, we analyzed the correction terms by station, and we found that the stations with the more positive ones (grater RSA) were the same stations to have amplification effects highlighted by H/V analysis. Furthermore, our models improve the EEW performances both in terms of true negatives and false positives.

The second work I present, "Earthquake Early Warning System for Structural Drift Prediction using Machine Learning and Linear Regressors" (Iaccarino et al., 2021; Chapter 3), uses data recorded from in-building sensors from Japanese and Californian structures. Here, we developed a method to predict Structural Drift using P-wave features (i. e.,  $P_d$ ,  $IV^2$ , and  $ID^2$ ) from 1s, 2s, and 3s windows. We studied the effects of the complexity of the dataset on the predictions subdividing the Japanese dataset in three subsets: data from one building; data from buildings with the same material of construction; entire dataset. From this study, we found that the variability of the dataset plays a key role in the predictions increasing the uncertainties of the predictions for the complete dataset. Moreover, we compared the performances of linear least square models and non-linear machine learning regressors finding that the last ones perform always better. In the end, we tried to export the model retrieved on Japanese buildings to the Californian buildings, finding that the drift predictions are underestimated by a bias. We proposed to correct this bias using magnitude dependent correction terms, finding that the linear models are more able to adapt in these conditions.

In the end, I present "Forecasting the Preparatory Phase of Induced Earthquakes by Recurrent Neural Network" (Chapter 1; Picozzi and Iaccarino, 2021). Here, we used catalogue information from a very complete dataset of the Californian geothermal area, The Geysers. From the catalogue, we chose 8 events with  $M > 3.9$ , and we selected the first 5 as training set and rest as testing set. Then, we extracted 9 features as time-series: the b-value and completeness magnitude,  $M_c$ , of the Gutenberg-Richter law; the fractal dimension of hypocenters,  $D_c$ ; the generalized distance between pairs of earthquakes,  $\eta$ ; the Shannon's information entropy,  $h$ ; the moment magnitude,  $M_w$ , and moment rate,  $\dot{M}_0$ ; the total duration of event groups,  $\Delta T$ , and the inter-event time,  $\Delta t$ . We wanted to assess the possibility to detect changes in time of these features that can be related to deviations from the background seismicity. We built two Recurrent Neural Networks, one to detect preparatory phase the other to detect the aftershocks phase. The method is able to discriminate both the preparatory phase and the aftershock phase on the testing set. In the end, merging the predictions of two methods, we found that all the three events in testing set present a preparatory phase that lasts from 4 hours to 2 days before the main event.

## 2. Onsite Earthquake Early Warning: Predictive Models for Acceleration Response Spectra Considering Site Effects

Antonio Giovanni Iaccarino<sup>1</sup>, Matteo Picozzi<sup>1</sup>, Dino Bindi<sup>2</sup>, and Daniele Spallarossa<sup>3</sup>

<sup>1</sup>University of Naples Federico II, Italy

<sup>2</sup>Helmholtz Centre Potsdam, GFZ German Research Centre for Geosciences, Germany

<sup>3</sup>University of Genova, Italy

Published in *Bulletin of the Seismological Society of America* (Iaccarino et al., 2020)

doi: 10.1785/0120190272.

## 2. Onsite Earthquake Early Warning: Predictive Models for Acceleration Response Spectra Considering Site Effects

### 2.1. Introduction

Currently, seismologists and engineers worldwide are called to contribute to mitigating the seismic risk to cities and infrastructure. One possible way to achieve this goal is represented by Earthquake Early Warning Systems (EEWS), which are highly technological infrastructures devoted to real-time, automatic detection and characterization of earthquakes, rapid assessment of the associated seismic hazard for sites at different epicentral distances, and prompt delivery of alerts through fast telecommunication networks. An alert is generally released when one or several ground motion parameters predicted at a target exceed a selected threshold, considered representative of a given damage level.

Although the main concept was proposed some time ago, EEWS have seen rapid development only over the last decade, mainly due to the improvements in telecommunication, data storage, and computer technologies. It is worth noting that these technological advances have been accompanied by significant scientific progress, and EEWSs are becoming increasingly precise and efficient. Several countries have built or are testing EEWS, for instance: California, Japan, Italy, Mexico, and China (e.g. Allen and Kanamori, 2003; Weber et al., 2007; Hoshihara et al., 2008; Espinosa-Aranda et al., 2009; Peng et al., 2011). A comprehensive review of concepts, methods, and recent developments in EEWS is provided by Allen and Melgar (2019). Hereinafter, we only briefly summarize the main EEWS concept, and we refer the readers to that publication for further background. The EEWS alert capability is related to the different propagation velocity of the slower S- and surface waves (the destructive ones) with respect to the faster P-waves. The time between the arrival of S-waves at a target site to be protected and the time when the alert is released (typically between one and a few seconds after the P-wave arrival time) is called lead time. The blind zone is defined as the area, with the extension being a function of network geometry, telemetry, and earthquake hypocenter location, within which the alert is not possible because the lead time is negative (the S-waves reach the target before it gets an alert). The lead time and blind zone are commonly used to evaluate the EEWSs performances, as well as the capability to predict correct ground motion levels at targets (Meier, 2017).

There are two main typologies of EEWS, regional and onsite (Satriano, Wu, et al., 2011). The main difference between the two approaches is that in the regional EEWS, the seismic network is built around a well-known seismogenic area that can damage targets at a certain distance; while, in an onsite one, a network (or eventually a single seismic station) is placed near the target, irrespective of the location of seismic threats. Regional EEWSs can be further divided into three model categories: point-source, finite fault, and ground motion-driven algorithms (Allen and Melgar, 2019). Point-source algorithms are generally fast, but their magnitude estimations saturate for very large magnitude earthquakes (Hoshihara and Ozaki, 2014). To remove the magnitude saturation effect, finite fault algorithms try to constrain in real-time the dimension and the geometry of the fault (Crowell et al., 2009; M. Böse et al., 2012; Minson et al., 2014). Finally, ground motion-driven approaches use the data recorded at the nearer stations to predict directly the ground motion at the target, without looking for the estimation of source parameters (Hoshihara, 2013; Hoshihara and Aoki, 2015; Kodera et al., 2018). Clearly, both regional and onsite approaches have pros and cons. Regional EEWSs can accurately estimate earthquake locations and magnitudes but are prone to the large uncertainty in ground motion prediction equations, which are used to predict the expected S-wave ground motion levels at target sites. Regional approaches are useful in cases where it is necessary to monitor a single or a few seismogenic areas, and several targets are placed outside the blind zone. For earthquakes located close to the target, onsite EEWS generally have lead times greater than regional ones, while the opposite is true at higher epicentral distances (Satriano, Wu, et al., 2011). This makes onsite approaches particularly suitable for targets located within the regional systems' blind zone. These systems exploit empirically calibrated relationships between the P-wave and S-wave amplitudes (Allen and Kanamori, 2003), which allows forecasting the intensity of ground motion or damage at targets (Kanamori,

## 2. Onsite Earthquake Early Warning: Predictive Models for Acceleration Response Spectra Considering Site Effects

2005; Wu and Kanamori, 2008; Böse et al., 2009; Zollo et al., 2010; Picozzi, 2012; Colombelli et al., 2015; Parolai et al., 2015). For instance, Brondi et al. (2015) exploited the “integral squared velocity” ( $IV^2$ ) and the “peak of displacement” (Pd) to predict the peak ground velocity (PGV) and Housner Intensity (IH). Caruso et al. (2017), instead, proposed an EEW platform called SAVE (on-Site Alert leVEl) that uses the Pd and the dominant period ( $\tau_c$ ) to predict PGV, magnitude, and the distance classification.

It is worth noting, however, that the empirical relationships proposed so far for onsite EEW have, to our knowledge, all been calibrated without considering station-to-station variability (Kanamori, 2005; Wu et al., 2006; Wu and Kanamori, 2008; Böse et al., 2009; Zollo et al., 2010; Picozzi, 2012; Wang and Wu, 2014; Brondi et al., 2015; Colombelli et al., 2015; Caruso et al., 2017). Therefore, the predictive EEW relations incorporate the response of the installation site into the ground motion aleatory variability. As we will show in this work, inclusion of correction terms for site effects significantly contribute to the decrease in the uncertainty in the ground motion level predicted at a target. In this study, the term “site effects” is meant in a broad sense. Primarily, we refer to those waveform alterations related to the effects of subsurface geology, but we also mean those effects related to the response of hosting structures, as installations for EEW onsite purposes are often performed within buildings or infrastructure (Fleming et al., 2009; Picozzi et al., 2011; Picozzi, 2012; Parolai et al., 2015; Petrovic and Parolai, 2016).

In the following, we calibrate and assess onsite EEWS predictive relationships between P-wave based parameters and acceleration response spectra (RSA). The RSA belongs to the spectral ordinates family (Gupta, 1993). Because the response spectra are constructed measuring the maximum response of a single-degree-of-freedom (SDOF) oscillator when it is excited by a seismogram, RSA amplitudes better correlate with structural damage than peak parameters such as peak ground acceleration (PGA) and velocity (PGV) (Elenas, 2000). Moreover, the development of onsite EEW models for RSA(T) at different periods of T facilitates tailoring the EEW predictions to the elastic response of the target building. However, the developed methodology can be easily extended to PGV, PGA or, eventually, other parameters considered more representative of the shaking intensity and damage potential for a specific EEW application. The use of response spectra in EEWS has been already proposed by Convertito et al. (2008) for regional EEWS, where the RSA(T) were estimated in real time from the predominant periods, the earthquake magnitude, and location. In this study, we investigate the scaling relationships between RSA (T) and two P-wave features, namely, the integral squared velocity ( $IV^2$ ) and the peak displacement (Pd), and we highlight the importance of the contribution of site-effects to the variability of calibrated EEW onsite models. This issue has been previously addressed in a few studies. Hoshiba (2013) proposed building relative frequency-dependent site amplification factors by deconvolving the waveforms recorded at the site with those recorded at a reference station; then, these site amplification factors were used to predict the ground motion intensity at the given site by exploiting the ground motion level measured at sites already hit by earthquakes. Zhao and Zhao (2019) presented an onsite EEW model for the S-to-P wave RSA spectral ratio [ $R(T) = RSA_S(T)/RSA_P(T)$ ] of both the first 3 s of waveforms and the full ones considering the vertical component of ground motion. In the same work, site-effects were modeled through a piece-wise linear additional term controlled by the averaged shear-wave velocity over the uppermost 30 m at the site. Finally, Spallarossa et al. (2019) presented an onsite EEW model for PGV using Pd and  $IV^2$  as P-wave features and developing a partially non-ergodic approach based on a mixed-effect regression where the site effects were treated as random effects.

In this study, we analyze a dataset of 58 earthquakes with moment magnitudes between  $M_w$  3.7 and 6.5 belonging to the Central Italy 2016–17 sequence (Luzi et al., 2017). With this dataset, we examine the model relationship between RSA at nine periods with respect to the EEW proxies of Pd and  $IV^2$  measured considering a time window starting from the P-wave onset and lasting 3 s or ending at the S-wave arrival for short epicentral distances. We focused on methodological aspects and performed retrospective, off-line analyses of earthquake recordings; hence, the P and S phases were manually picked from the records. The

## 2. Onsite Earthquake Early Warning: Predictive Models for Acceleration Response Spectra Considering Site Effects

choice of the P-waves window length was critical. As discussed by Zollo et al. (2010), for large magnitude events ( $M_w > 7$ ), an overly narrow window could not include enough information for the large earthquakes with long duration ruptures, leading to saturation of the parameters for large earthquakes. However, the 3 s EEW time-window length used in this study was considered adequate for correctly analyzing the higher magnitude earthquakes characterizing the Italian Apennine seismicity. Finally, it is worth noting that for earthquakes with magnitudes larger than 6, near source sites can experience non-linear site-effects (Guéguen et al., 2019), but the development of site-specific empirical relationships accounting for non-linear response of unconsolidated sediments is beyond the scope of this work.

Similarly to Spallarossa et al. (2019), we apply a regression analysis with random effects to explore the site-specific variability of the predicted ground shaking (in terms of RSA) by considering two different grouping levels: in the first one, the random effects are assigned unique values for each station; in the second one, stations are grouped considering the soil classification according to the European (EC8) classification (European Committee for Standardization, 2004). Subsequently, we present the results of a validation analysis using the leave one out technique (Stone, 1974) and K-means clustering (Lloyd, 1982; Pedregosa et al., 2011). Finally, we analyze the performance of a hypothetical probabilistic alert decision module applied to the data from two stations with significant site amplification, showing that onsite EEWS applications that include site effects in their predictive models provide more precise alerts.

### 2.2 Dataset and pre-processing

We analyze 58 earthquakes from the 2016–17 Central Italy sequence with  $M_w$  between 3.7 and 6.5, selecting recordings at 199 stations of the RAN (*Rete Accelerometrica Nazionale*; Gorini et al., 2010) located at hypocentral distances smaller than 150 km. The RAN consists of approximately 500 digital strong motion stations with data telemetry and time synchronization by GPS, spread over the higher seismic hazard areas of Italy. RAN data are collected, validated, and made available by the ITACA 2.0 database (Luzi et al., 2008; Pacor et al., 2011). We estimate the EEW parameters  $P_d$  and  $IV^2$  following the procedure proposed by Caruso et al. (2017). The processing consists of sensitivity correction, trend removal, P- and S-phase identification and manual picking, and single and double integration to obtain the velocity and displacement records. The  $P_d$  are measured on bandpass-filtered displacement using a Butterworth filter between 0.075–20 Hz to remove the long-period drift after the double integration.

The integral of the squared velocity ( $IV^2$ ) is defined as

$$IV^2 = \int_t^{t+\Delta t} v^2(t) dt \quad (1)$$

where the integral is computed over a window of length  $\Delta t$  after the first P-wave arrival time, and  $v^2$  is the ground motion velocity squared. Kanamori et al. (1993) and (Matteo Picozzi et al., 2017) showed that when  $IV^2$  is computed on direct S-waves, it provides information on energy radiated by the rupture process. Following Caruso et al. (2017), the signal-to-noise ratio (SNR) associated with the record is obtained as

$$SNR = 20 * \log \frac{P_d}{P_d^{noise}} \quad (2)$$

where  $P_d^{noise}$  is computed for the 5 s preceding the P-wave arrival on the vertical trace.

Because one of our targets is to investigate the impact of site-specific effects on onsite EEW models, we selected only stations with at least five recordings with  $SNR > 14$ . The final database used for the calibration of the EEWS relations is composed of 1029 records at 100 stations (Figure 2-1).

## 2. Onsite Earthquake Early Warning: Predictive Models for Acceleration Response Spectra Considering Site Effects

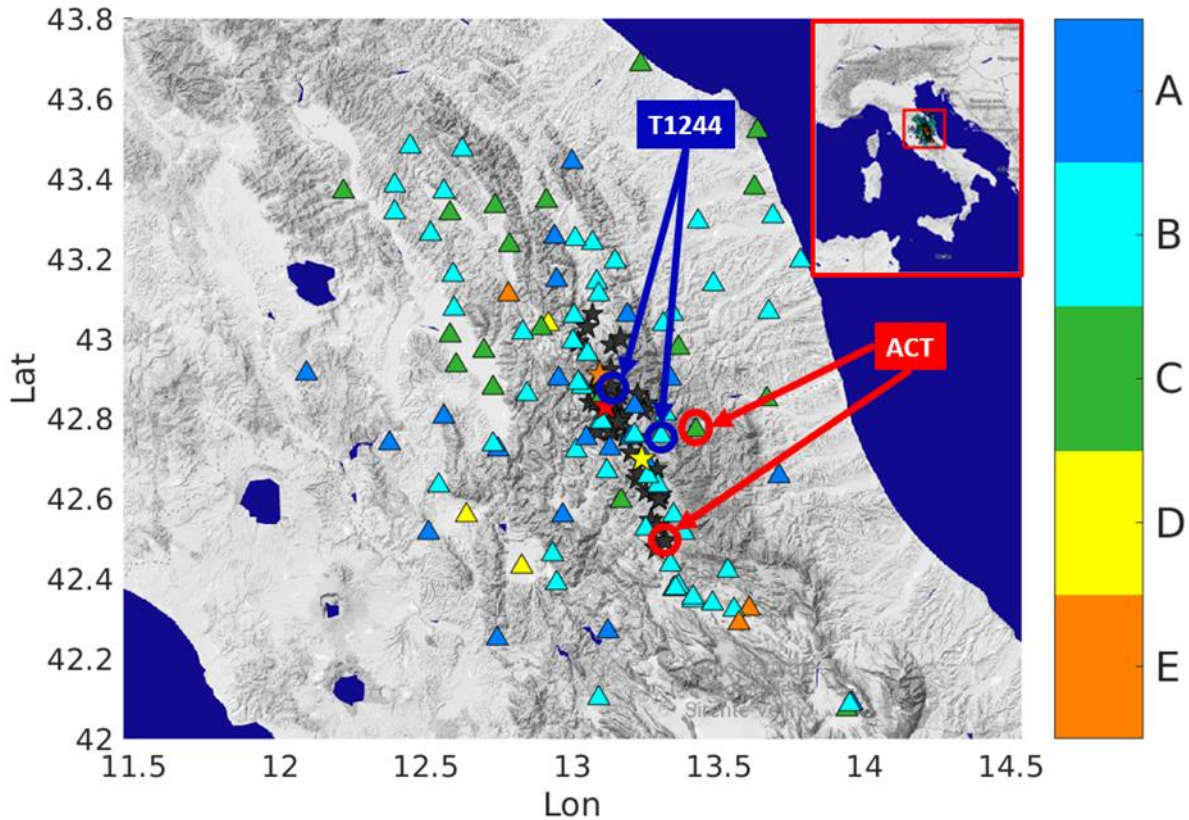


Figure 2-1: Map of the events (stars) and accelerometric stations (triangles) used in this work. The stations are colored according to their EC8 classification (see color bar). The three mainshocks of the Central Italy sequence are colored: 08/24/2016  $M_w$  6.0, Amatrice earthquake (yellow star), 10/26/2016  $M_w$  5.9, Visso (orange star), and 10/30/2016  $M_w$  6.5, Norcia earthquake (red star); while all the other earthquakes are shown as black stars. We also highlighted the ACT and T1244 stations and the earthquakes for which we show waveforms and RSA in other figures.

We computed the RSA for each horizontal component following the processing scheme proposed by (Paolucci et al., 2011) and we combined the two horizontal RSAs considering the quadratic mean. We used a damping ratio equal to 0.05 and selected the RSA amplitude for nine periods,  $T$  ( $T = 0.1, 0.15, 0.2, 0.3, 0.5, 0.75, 1.0, 1.5,$  and  $2.0$  s). Figure 2-2a shows, as an example, the recordings at the ACT and T1244 stations for two earthquakes with magnitude  $M_w$  5.4, with similar epicentral distances (33 and 22 km, respectively) and azimuths, but different EC8 classifications (Figure 2-1); the ACT station is classified as C (large site effects are expected), while T1244 is classified as B (rigid soils where moderate site effects are expected). For the EEW parameters, ACT has  $P_d$  equal to 0.030 cm and  $IV^2$  equal to 0.054  $\text{cm}^2/\text{s}$ , while T1244 has  $P_d$  equal to 0.034 cm and  $IV^2$  equal to 0.050  $\text{cm}^2/\text{s}$ . Since the P-wave features extracted from stations ACT and T1244 are similar, ergodic onsite EEW models predict similar ground shaking levels for S-waves at these two sites. Indeed, ACT showed significantly larger S-wave amplitude than T1244 (PGA values are 112  $\text{cm}/\text{s}^2$  and 76.7  $\text{cm}/\text{s}^2$  for ACT and T1244, respectively), although ACT is located at a larger epicentral distance than T1244. Figure 2-2b and 2-2c show that the RSA values for ACT are almost one order of magnitude larger than for T1244.

## 2. Onsite Earthquake Early Warning: Predictive Models for Acceleration Response Spectra Considering Site Effects

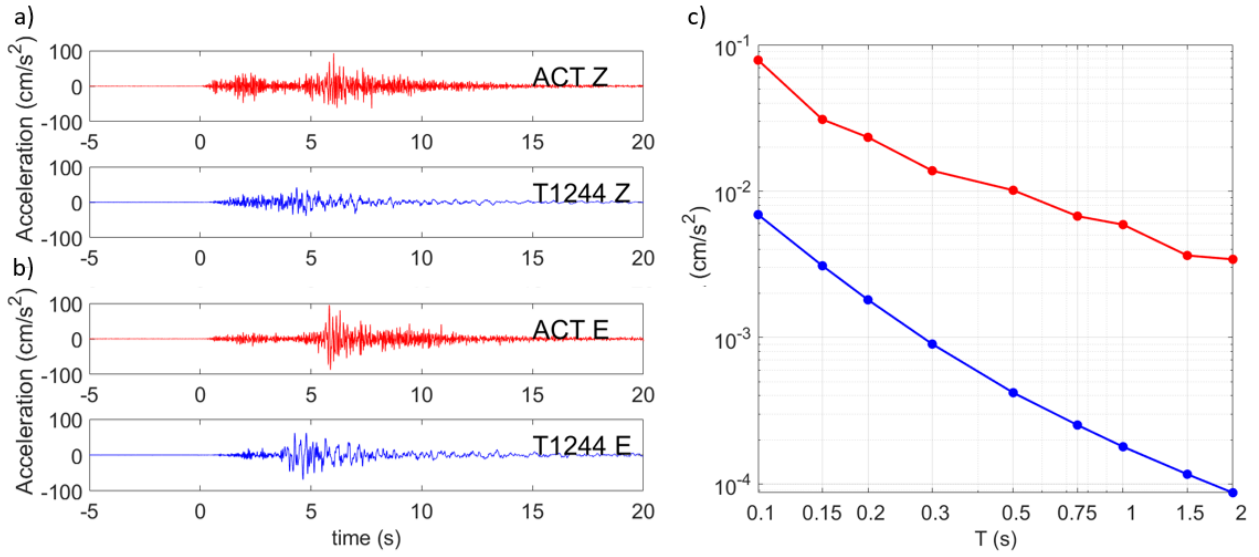


Figure 2-2: a) and b) Vertical and E-W accelerations (cm/s<sup>2</sup>) at the ACT (red) and T1244 (blue) stations. c) the same as a), but for RSA (cm/s<sup>2</sup>) vs. period T (s).

### 2.3. Method: mixed-effect regression

The development of ground motion prediction equations (GMPE) for probabilistic seismic hazard assessment requires that data from multiple stations are jointly analyzed to overcome the limitation of the temporal sampling available at single stations, assuming that the spatial variability can be mapped to the temporal variability (Anderson and Brune, 1999). The same assumption is usually made when developing onsite EEW models (see, among others, Wu et al., 2006; Wu and Kanamori, 2008; Zollo et al., 2010; Brondi et al., 2015; Colombelli et al., 2015; Caruso et al., 2017). Because the GMPE accounts for site effects in a relatively simple manner, site-specific repeated effects inflate the aleatory variability of the model (generally referred to as  $\sigma$ ). Therefore, in the GMPE development it is standard practice to introduce a structure in the residual distribution by isolating the event-specific component (referred to as inter-event or between-event residuals) from the record specific one (referred to as intra-event or within-event). Recognizing the existence of a dependent structure across observations, more complex decomposition of the residuals can be attempted (Al Atik et al., 2010) using mixed-effects regression (Pinheiro and Bates, 2000; Bates et al., 2015). Introducing different random effects in the regression model allows it to handle dependencies across observations (among the recordings of the same event at different stations) as well as for different related baselines, for example, to regional effects introduced by the ergodic assumption (Stafford, 2014). As the present study is focused on onsite EEW, we are particularly interested in controlling the site-to-site variability and in mitigating the effect of the ergodic assumption. Therefore, we develop onsite EEW models connecting  $P_d$  and  $IV^2$  to  $RSA(T)$ , using a mixed-effects regression to determine the coefficients and test two alternative grouping factors: one in which recordings are grouped by station so that the random effects assume one value per station (site-to-site variability), and another in which recordings are grouped by their EC8 site classification (class-to-class variability). The functional form of the models can be written as

$$\log_{10} RSA(T) = a^{Pd-S} + b^{Pd-S} * \log_{10}(Pd) + \delta S 2S^{Pd-S} + \epsilon^{Pd-S} \quad (3)$$

$$\log_{10} RSA(T) = a^{Pd-C} + b^{Pd-C} * \log_{10}(Pd) + \delta S 2S^{Pd-C} + \epsilon^{Pd-C} \quad (4)$$

## 2. Onsite Earthquake Early Warning: Predictive Models for Acceleration Response Spectra Considering Site Effects

$$\log_{10} RSA(T) = a^{Iv2-S} + b^{Iv2-S} * \log_{10}(Iv2) + \delta S2S^{Iv2-S} + \epsilon^{Iv2-S} \quad (5)$$

$$\log_{10} RSA(T) = a^{Iv2-C} + b^{Iv2-C} * \log_{10}(Iv2) + \delta S2S^{Iv2-C} + \epsilon^{Iv2-C} \quad (6)$$

where the apexes indicate whether the regression is performed for Pd or IV<sup>2</sup> and whether the grouping factors are the stations (S) or the EC8 classes (C). In Eqs. (3) to (6), the coefficients a and b are the fixed effects of the model,  $\delta S2S$  distribution is either the inter-station or inter-class random effects, and  $\epsilon$  is the intra-station or the intra-class residuals. In the following, we indicate with  $\sigma_{SS}$  the standard deviation of the  $\epsilon$  distribution (representing the aleatory variability of single-site ground motion) and with  $\phi_{S2S}$  the standard deviation of the  $\delta S2S$  distribution (site-to-site variability, Al Atik et al., 2010). Table 2-1 reports all these symbols used in this study along with their description. The models are derived for nine different periods, T (i.e., 0.1, 0.15, 0.2, 0.3, 0.5, 0.75, 1.0, 1.5, and 2.0 s) and Table 2-2 lists the obtained coefficients a and b for Eqs. 3–6.

Table 2-1: Acronyms and Symbols used in this work.

Acronym or Symbol	Description
EEWS	Earthquake Early Warning System
Pd	Peak of Displacement
IV <sup>2</sup>	Integral squared velocity
RSA	Response Spectra of Acceleration
$\delta S2S$	Onsite EEW site-to-site residuals
$\epsilon$	Station corrected residuals
$\gamma$	Residuals from median model, $\gamma = \epsilon + \delta S2S$
$\sigma_{SS}$	Aleatory variability of the ground motion under the partially non-ergodic single-site assumption
$\phi_{S2S}$	Standard deviation of the onsite EEW site-to-site residuals
$\sigma$	Aleatory variability of the ground motion under the ergodic assumption, $\sigma = \sqrt{\sigma_{SS}^2 + \phi_{S2S}^2}$
$RSA_{obs}$	Observed RSA
$RSA_{erg}$	RSA predicted without using site correction (ergodic)
$RSA_{rand}$	RSA predicted using site correction (random-effect procedure)
$RSA_{thres}$	EEW threshold
$RSA_{pred}$	RSA predicted, can be both with and without site-correction

## 2. Onsite Earthquake Early Warning: Predictive Models for Acceleration Response Spectra Considering Site Effects

Table 2-2: Coefficients of Eqs. (3, 4, 5, and 6) for all considered periods.

<b>T(s)</b>	$a^{Pd-S}$	$b^{Pd-S}$	$a^{Pd-C}$	$b^{Pd-C}$	$a^{lv2-S}$	$b^{lv2-S}$	$a^{lv2-C}$	$b^{lv2-C}$
<b>0.1</b>	0.004	0.897	0.045	0.850	-0.452	0.526	-0.475	0.481
<b>0.15</b>	-0.494	0.855	-0.413	0.829	-0.929	0.502	-0.915	0.471
<b>0.2</b>	-0.814	0.822	-0.710	0.803	-1.23	0.482	-1.19	0.457
<b>0.3</b>	-1.28	0.756	-1.14	0.746	-1.66	0.445	-1.58	0.427
<b>0.5</b>	-1.74	0.701	-1.59	0.692	-2.09	0.414	-1.99	0.398
<b>0.75</b>	-2.05	0.664	-1.90	0.659	-2.38	0.392	-2.28	0.380
<b>1.0</b>	-2.25	0.642	-2.09	0.637	-2.56	0.380	-2.45	0.368
<b>1.5</b>	-2.51	0.614	-2.34	0.611	-2.81	0.363	-2.69	0.354
<b>2.0</b>	-2.66	0.602	-2.49	0.599	-2.95	0.357	-2.83	0.348

## 2.4 Results

### 2.4.1 Model calibration

Figure 2-3 exemplifies the results of the regression between RSA at a period equal to 0.5 s and Pd when data (grey dots) are grouped by station (Eq. 3). The calibrated model considering only the fixed-effect coefficients ( $a^{Pd-S}$  and  $b^{Pd-S}$  in this example) is hereinafter referred to as median prediction, and we recall that it refers to the whole dataset of 1029 records at 100 stations. Figure 2-3 shows that the median model fits the data well but with large variability. The random effects  $\delta S2S^{Pd-S}$  act as station-dependent adjustments to the intercept of the median model and, as an example, Figure 2-3 shows the adjustments for the ACT (red line) and T1244 (blue line) stations. ACT, which is classified as EC8 Class C (i.e., shear wave velocity  $v_{s30}$  averaged in the uppermost 30 m in the range 180-360 m/s), presents RSA values distributed above the median predictions ( $\delta S2S^{Pd-S}$  is positive; orange dots in Figure 2-3), while station T1244 (EC8 Class B,  $v_{s30}$  in the range 360-800 m/s) shows RSA values distributed below the median model (negative  $\delta S2S^{Pd-S}$ ; cyan dots in Figure 2-3). The capability of the onsite EEW model with random effects to capture different baselines at the different stations has the beneficial result of decreasing the standard deviation  $\sigma_{SS}$  of the residuals  $\epsilon$  (Eq. 3). Indeed,  $\sigma_{SS}$  is reduced with respect the ergodic  $\sigma$ , as the site-to-site component is removed. Table 2-3 lists  $\sigma_{SS}$  and  $\sigma$  computed for the whole dataset at each RSA period. However, it is worth remembering that, along with these beneficial effects obtained by including site-specific adjustments to our models, the epistemic uncertainty affecting the random effects increases the overall epistemic uncertainty of the model.

2. Onsite Earthquake Early Warning: Predictive Models for Acceleration Response Spectra Considering Site Effects

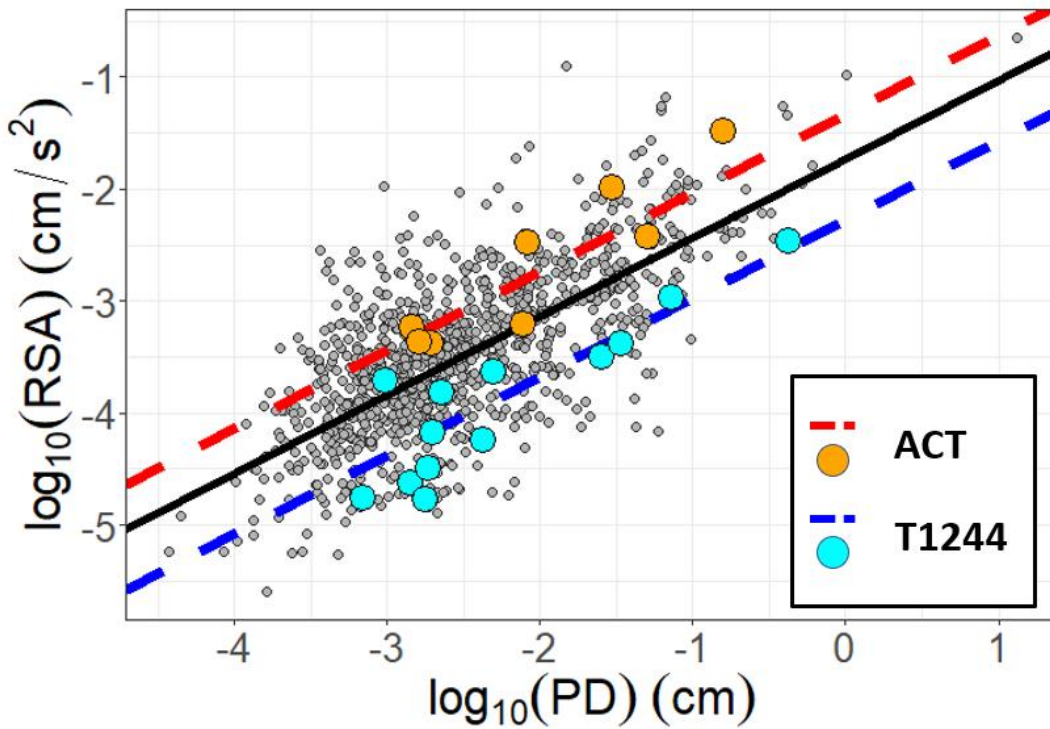


Figure 2-3: RSA (cm/s<sup>2</sup>) for the period of 0.5 s vs. the Pd (cm) used for the analysis (gray dots). Data from the ACT (orange dots) and T1244 (cyan dots) stations. The median model retrieved from all data (black line), and the mixed-effect model for ACT (red dashed line) and T1244 (blue dashed line).

Table 2-3:  $\sigma$  and  $\sigma_{SS}$  for Eqs. (3, 4, 5, and 6) for the considered periods

T(s)	$\sigma^{Pd-S}$	$\sigma_{SS}^{Pd-S}$	$\sigma^{Pd-C}$	$\sigma_{SS}^{Pd-C}$	$\sigma^{Iv2-S}$	$\sigma_{SS}^{Iv2-S}$	$\sigma^{Iv2-C}$	$\sigma_{SS}^{Iv2-C}$
0.1	0.60	0.42	0.60	0.58	0.57	0.39	0.56	0.53
0.15	0.55	0.40	0.56	0.53	0.51	0.36	0.51	0.49
0.2	0.53	0.38	0.54	0.51	0.49	0.35	0.49	0.47
0.3	0.52	0.37	0.54	0.50	0.48	0.34	0.49	0.45
0.5	0.52	0.37	0.54	0.50	0.48	0.35	0.50	0.46
0.75	0.51	0.37	0.53	0.49	0.47	0.34	0.49	0.45
1.0	0.51	0.37	0.53	0.49	0.47	0.34	0.49	0.45
1.5	0.51	0.37	0.53	0.49	0.48	0.35	0.50	0.45
2.0	0.52	0.37	0.54	0.49	0.48	0.35	0.50	0.46

## 2. Onsite Earthquake Early Warning: Predictive Models for Acceleration Response Spectra Considering Site Effects

To assess the effectiveness of the calibration procedure, we compute the residuals  $\gamma_{ei}$  (where  $i$  can indicate either a station  $s$  or a specific EC8 class  $c$ , and  $e$  is a specific event) between the observed RSA and the predictions considering the median model without the  $\delta S2S$  corrections ( $\gamma = \epsilon + \delta S2S$ ). The residuals are

normalized to the total aleatory variability  $\sigma = \sqrt{\sigma_{SS}^2 + \phi_{S2S}^2}$ .

The normalized residuals ( $\gamma_{ei}/\sigma$ ) help us to assess how much a subgroup of data (those recorded by a given station or at a specific EC8 class) differ from the median model.

Figure 2-4 presents  $\gamma_{ei}/\sigma$  (white circles) for three periods (0.15, 0.5, and 1.5 s) using the data grouped by station (Eq. 3). For each station, we computed the mean of the normalized residual ( $\langle \gamma_{ei}/\sigma \rangle$ , represented as white squares) and the normalized single-station variability (the standard deviation of  $\gamma_{ei}/\sigma$ ), which is colored per the EC8 station classification (vertical bars). We observe that approximately 20–25% of the stations (depending on the period, ranging from a number of 18 stations at 0.15 s, to 23 stations at 1.5 s) have a mean normalized residual exceeding 1 in absolute value. A t-test confirms that 20 and 17 stations at periods 0.15 and 1.5 s, respectively, have a mean normalized residual different from zero at the 95% confidence interval. An example of a station with particularly high  $\langle \gamma_{ei}/\sigma \rangle$  is NCR (Nocera village), where the large amplifications observed at frequencies between 5 Hz and 10 Hz (Luzi et al., 2005; Bindi et al., 2011) are controlled by a buried wedge of weathered rock (Rovelli et al., 2002). Other stations with large positive residuals are FOC (Colfiorito village) and SPM (Spello village). SPM is classified as a rock station (EC8 Class A, vs30 larger than 800 m/s) and further analyses are needed to identify a possible explanation for the observed amplifications, such as local geological conditions (Marzorati et al., 2011) or housing effects (Mucciarelli et al., 2017) since SPM is installed inside a power supply distribution substation. However, stations beginning with T12\*\* (T1221, T1214, and T1212) show negative normalized residuals, in some cases smaller than -2. These stations belong to a group of temporary stations installed by INGV staff (National Institute of Geophysics and Volcanology) soon after the 08/24/2016  $M_w$  6.0, Amatrice earthquake, on stiff soil (Class B) or rock (Class A) sites. To better clarify the relation between  $\langle \gamma_{ei}/\sigma \rangle$  and the site effects, we computed the horizontal-to-vertical spectral ratio (H/V) considering 12 s long windows over the S-waves, considering hundreds of small-to-moderate magnitude earthquakes (maximum magnitude  $M_w$  4.5; the number of earthquake recordings used for each station is reported within Figure 2-5) and applying the Konno and Ohmachi (1998) smoothing operator (using  $b = 20$ ) for a set of specific stations (NCR, FOC, T1212, and T1221).

## 2. Onsite Earthquake Early Warning: Predictive Models for Acceleration Response Spectra Considering Site Effects

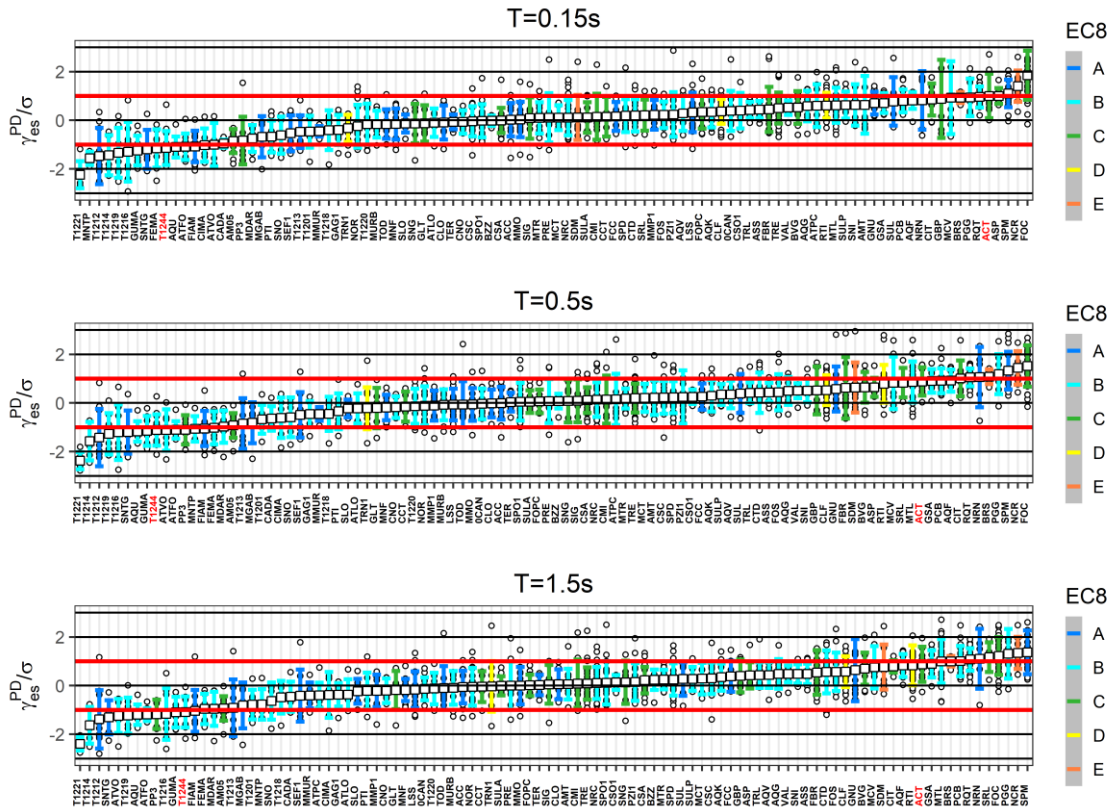


Figure 2-4: Normalized residuals for Pd (relation 3) for the periods  $T = 0.15$  s. a),  $T = 0.5$  s. b), and  $T = 1.5$  s. c). Normalized residuals for single recordings (white circles); the mean of the normalized residuals for each station (white squares); error bars proportional to the standard deviation of the normalized residuals (vertical bars colored by the EC8 classification of the station). The residuals are sorted in ascending order. Red horizontal lines indicate  $\pm 1$  standard deviation. We highlighted the ACT and T1244 stations in the labels for explanation purposes.

Figure 2-5a, and b show that the H/V for the NCR and FOC stations, which are characterized by large  $\langle \gamma_{ei}/\sigma \rangle$ , values, present strong amplification peaks (at 7–8 Hz and 20 Hz for NCR and around 5 Hz and 15–20 Hz for FOC). On the contrary, T1212 and T1221 stations (Figure 2-5c, and d) present flat H/V ratios, suggesting that strong site amplifications are not expected for these stations in agreement with the mixed-effect results (both stations are characterized by small  $\langle \gamma_{ei}/\sigma \rangle$  values).

With respect to the classic approach based on the ergodic assumption, our results indicate that significant site-specific deviations from the median model exist for a consistent number of stations among those considered. The mixed effects regression facilitates capturing site-specific repeated effects by introducing random effects on the station population. As an example of the improvement obtained by considering site-specific adjustments, we present Figure 2-6 which shows the normalized residuals considering (Figure 2-6a,  $\gamma_{ei}/\sigma$ ) or not considering (Figure 2-6b,  $\gamma_{es}/\sigma_{SS}$ ) the random effects. In Figure 2-6, considering the case of Eq. (3) for  $T$  equal to 0.3 s, the values of  $\sigma$  and  $\sigma_{SS}$  are equal to 0.52 and 0.37, respectively (see also Table 2-3). Considering the  $\delta S2S^{Pd-S}$  station terms, the predicted RSA are adjusted for site-specific baselines and the aleatory variability is reduced, resulting in an improved accuracy and precision of the Pd and  $IV^2$  predictions for site-specific onsite EEW applications. Possible impacts on alert protocols are discussed in Section 2.4.4 Implications of random effects for an onsite EEW decision alert system.

## 2. Onsite Earthquake Early Warning: Predictive Models for Acceleration Response Spectra Considering Site Effects

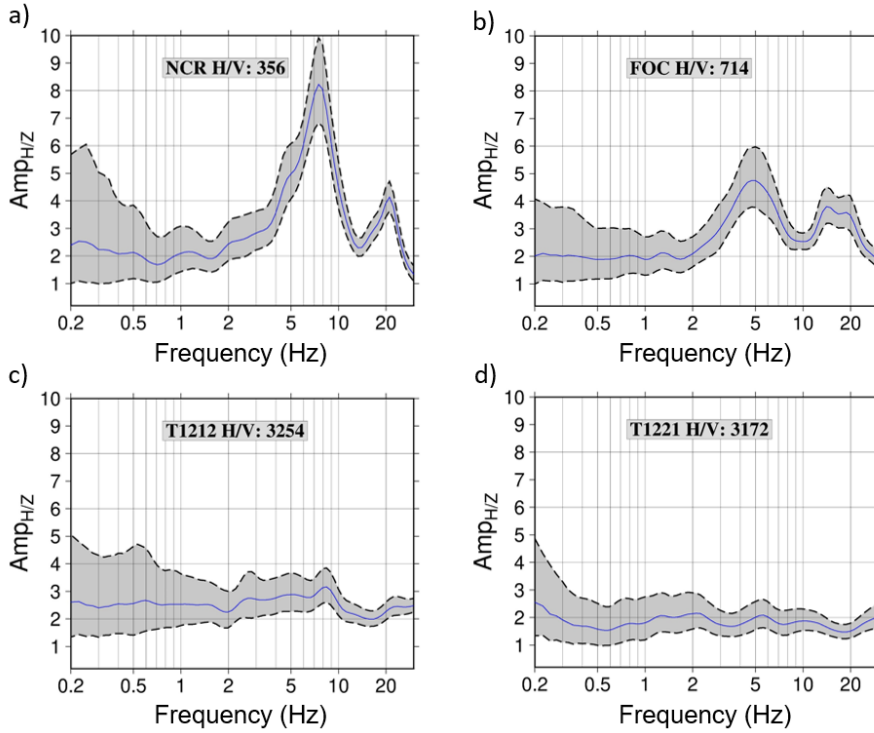


Figure 2-5: H/V ratio computed for the stations: NCR (a); FOC (b); T1212 (c); T1221 (d). The number of events considered is reported for each station within the plot.

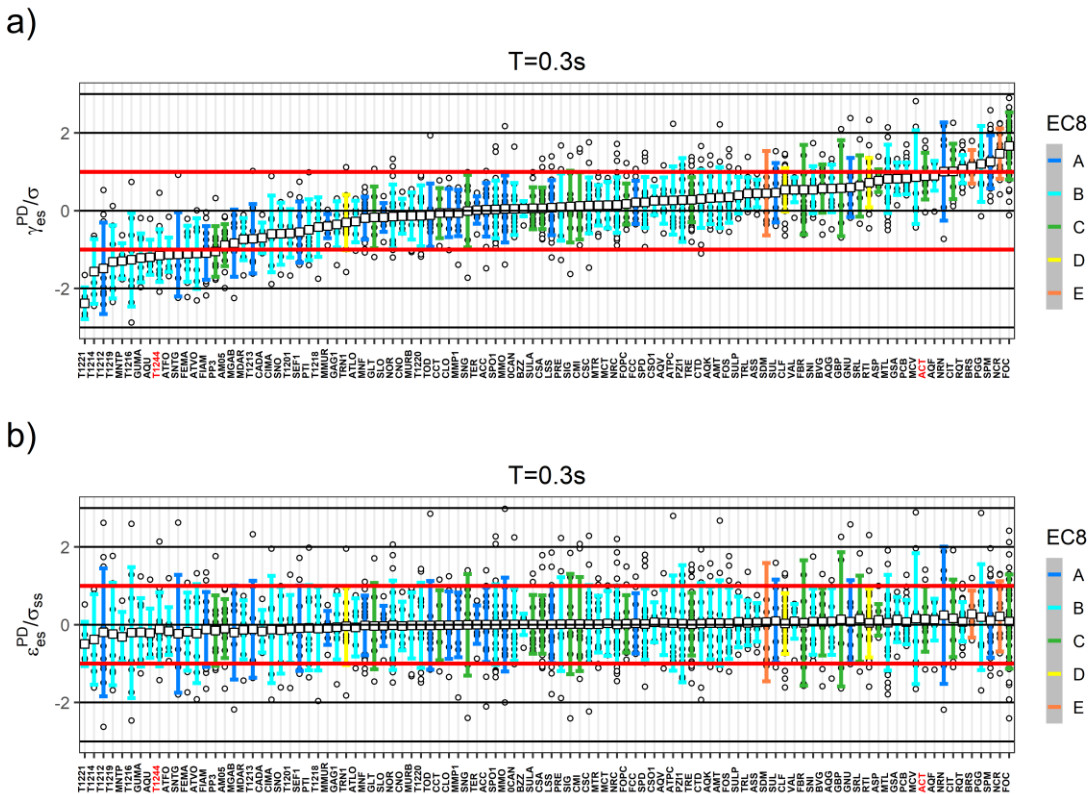


Figure 2-6: a) Normalized residuals for  $P_d$  (Eq. 3) for the period  $T$  equal to 0.3 s. b) Normalized residuals corrected by  $\delta S2S$  factor for  $P_d$  (Eq. 3) for the period  $T = 0.3$  s. In both the figures, normalized residuals for single recordings (white circles); the mean of the normalized residuals for each station (white squares); error bars proportional to the standard deviation of the normalized residuals (vertical bars colored by the EC8 classification of the station). The stations are sorted by ascending order of normalized residuals. Red horizontal lines indicate  $\pm 1$  standard deviation. We highlighted the ACT and T1244 stations in the labels for explanation purposes.

## 2. Onsite Earthquake Early Warning: Predictive Models for Acceleration Response Spectra Considering Site Effects

Searching for a simple and standardized site classification that could be suitable for EEW onsite applications, we tested the European EC8 classification as possible grouping factors for the random effects. EC8 classifies the sites mainly through the mean shear-wave velocity in the uppermost 30 m ( $V_{s30}$ ). In this regard, Class A refers to sites with a  $V_{s30}$  greater than 800 m/s (rock site); Class B ( $360 < V_{s30} < 800$  m/s) is a broad class including sites characterized mainly by very dense sand, gravel, and very stiff clay; and Class C ( $180 < V_{s30} < 360$  m/s) and Class D ( $V_{s30} < 180$  m/s) correspond to soft soil sites with amplifications expected to occur mainly at low frequencies. Class E corresponds to shallow ( $5 < h < 20$  m) class C or D sites overlying rock (Class A), with amplification occurring mainly at high frequencies (like at the NCR station). Finally, EC8 also includes special classes for sites with extreme low velocity and high susceptibility to liquefaction, which are not considered in this study. Figure 2-7 shows  $\gamma_{ei}/\sigma$  for three periods (0.15 s, 0.5 s, and 1.5 s, shown as white circles) grouping the data by EC8 (Eq. 4). As in Figure 2-4, in Figure 2-7 we represent the median value of  $\delta S2S^{Pd-C}$  for each soil class (white square) and the normalized soil class variability (vertical bars). The results show that the median  $\delta S2S^{Pd-C}$  for classes A and B are, for all periods, always negative, while  $\delta S2S^{Pd-C}$  for Class E is always positive. However, the median normalized residuals  $\langle \gamma_{ei}/\sigma \rangle$  do not differ appreciably among the different classes, and considering the uncertainties, are not significantly different from zero. These results indicate that for an onsite EEW application, where the goal is predicting the response spectra amplitudes using features extracted from early P-waves signals, the EC8 classification is not a suitable grouping factor to account for site effects, because the intra-class variability dominates that of the inter-class. This result confirms several previous studies about the identification of suitable proxies to define site classifications (Luzi et al., 2011; Kotha et al., 2018, among many others).

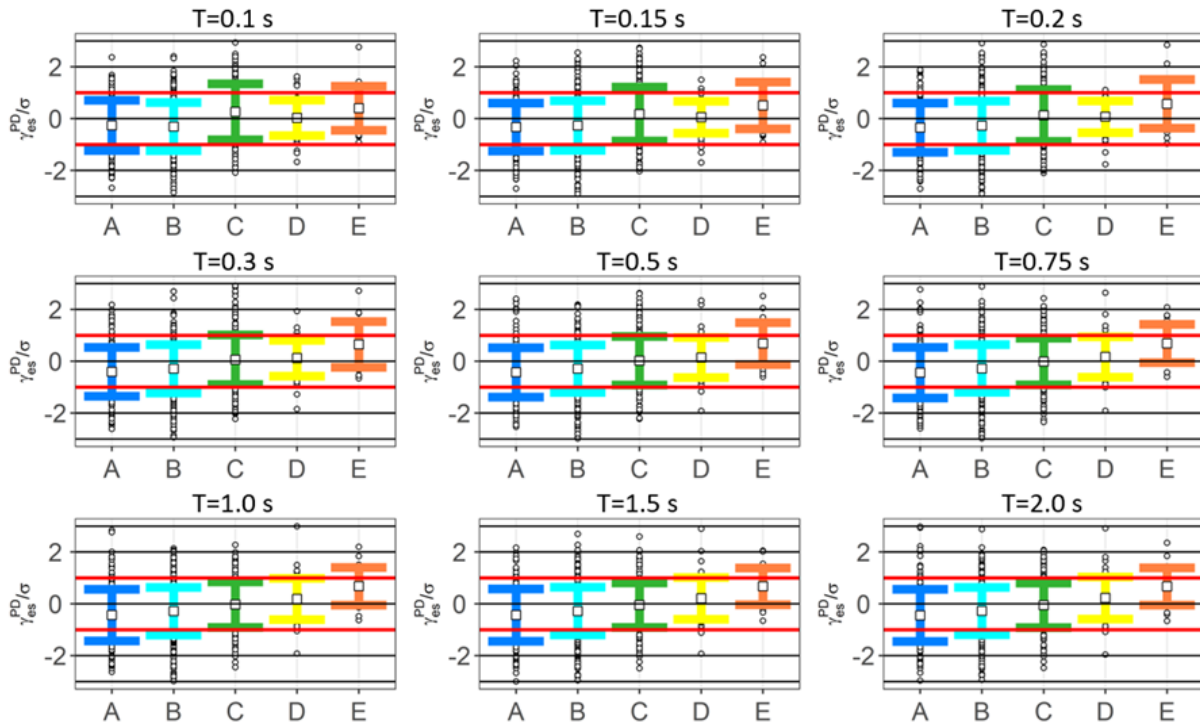


Figure 2-7: Normalized residuals for  $P_d$  considering the EC8 classes (relation 4) for nine periods. White circles are the normalized residuals for the data; white square dots are the mean of the normalized residuals for each class; the error bars are proportional to the standard deviation of the normalized residuals, and they are colored by the EC8 classification. Red horizontal lines indicate  $\pm 1$  standard deviation.

## 2. Onsite Earthquake Early Warning: Predictive Models for Acceleration Response Spectra Considering Site Effects

### 2.4.2 Model validation: Leave-one-out cross-validation

To validate the calibrated models (Eqs. 3–6), we perform a leave-one-out (L1Out) cross-validation (Stone, 1974). Briefly, the analysis consists of repeating the calibration procedure as many times as the number of data, every time leaving out one experimental data point from the calibration procedure; the excluded data point is in turn used to assess the predictive power of the model calibrated at each L1Out iteration. Hence, for all considered models (Eqs. 3–6) and all the periods, we perform as many regressions as the number of data points and we computed the residual between the excluded data points and the prediction made by the L1Out relations, with and without considering the  $\delta S2S$  corrections. Figure 2-8a, and b present, for each RSA period, the standard deviation of the residuals  $\sigma_{L10}$  for Pd and  $IV^2$  (relations 3 and 5). Red dots represent the residuals computed without considering the term  $\delta S2S$ , whereas the residuals corrected by considering the random effects are shown with green and blue dots. The large differences shown by  $\sigma_{L10}$  computed with and without random-effects indicate that both  $\delta S2S^{Pd-S}$  and  $\delta S2S^{IV^2-S}$  permit capturing the site-specific effects. This result confirms the significant impact local site conditions can have on the response spectrum variability. On the other hand, as shown in Figure 2-8c and d, the site correction terms for the EC8 grouping level ( $\delta S2S^{Pd-C}$  and  $\delta S2S^{IV^2-C}$  from Eq. 4 and Eq. 6) results in a very small improvement with respect to the ergodic model. These results highlight that, with respect to the station term, grouping stations according to their EC8 classification is not useful to capture site effects for the RSA in EEW predictive models. On the contrary, our results confirm that considering a site-specific adjustment accounting for local amplification effects allows reduction of the uncertainty related to EEW estimates. Comparing the variability  $\sigma_{L10}$  in Figure 2-8a and b, we observe a smaller variability when equation (5) is implemented. Therefore, RSA is better predicted using  $IV^2$  as P-wave feature. This is probably due to the nature of  $IV^2$  itself which, like RSA, is an integral quantity. Finally, we observed that the  $\sigma_{L10}$  has the same trend for all the models, exhibiting a maximum at the lowest analyzed period (0.1 s), it decreased until 0.3 s, and then it remained almost constant for the shortest periods. The origin of this trend is not clear, and it will be investigated in the future while also considering other datasets.

## 2. Onsite Earthquake Early Warning: Predictive Models for Acceleration Response Spectra Considering Site Effects

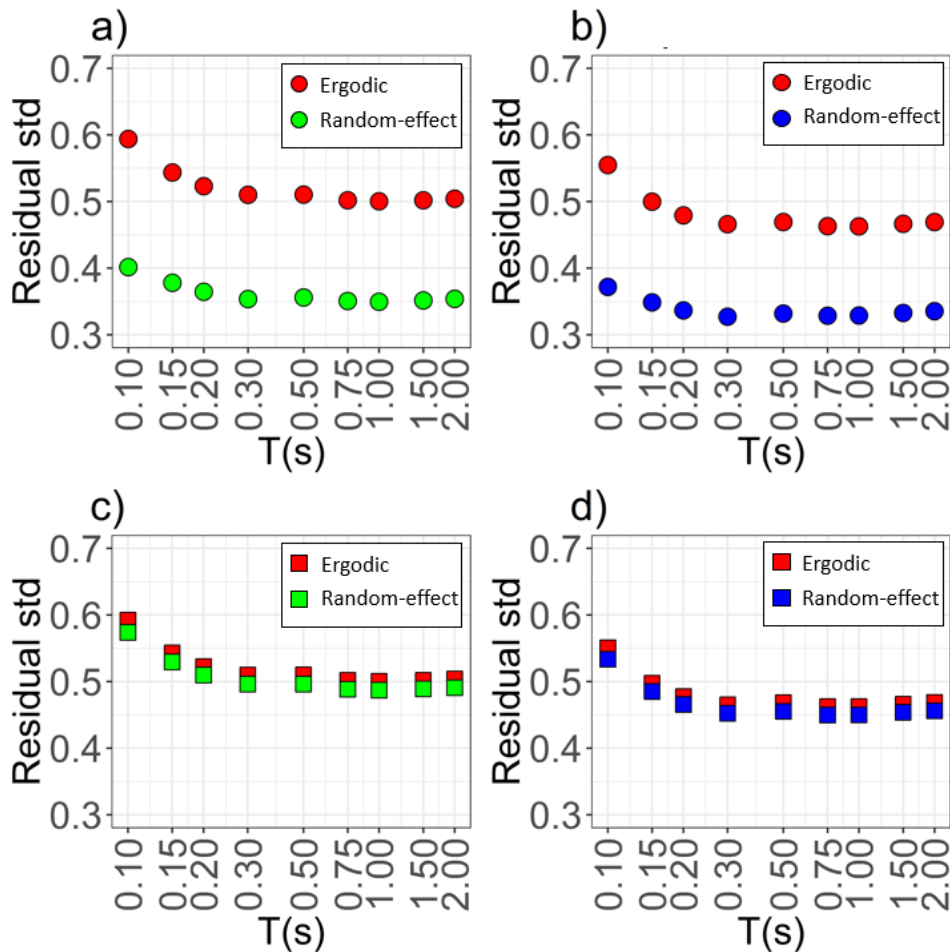


Figure 2-8: Standard deviation (std) of the residuals obtained from the L1Out validation procedure for different periods, comparing the residuals for the ergodic model, i.e. without considering the  $\delta S2S$  and the ones obtained correcting the data by the group  $\delta S2S$ . Figure a) refers to Eq. 3, Figure b) refers to Eq. 5, Figure c) refers to Eq. 4 and Figure d) refers to Eq. 6.

### 2.4.3 Analysis of random effect vs. period

Having analyzed nine different RSA periods ( $T$ ), we study the variability of  $\delta S2S^s$  as a function of  $T$  to investigate the reasons for the poor capability shown by the EC8 classification in describing site effects within our EEW context. For this purpose, we grouped the  $\delta S2S^{Pd-S}$  curves ( $\delta S2S^s$  as a function of the nine periods) by EC8 classes. Figure 2-9a, b, and c show the  $\delta S2S^{Pd-S}$  curves derived for each station grouped by EC8 classes, excluding class D and E sites due to the small number of stations belonging to these classes in our dataset. These results show that, irrespective of the EC8 class, there are no clear and common pattern between stations. This confirms further that the EC8 classification cannot provide useful information for EEW purposes. Despite the negative EC8 classification performance, we further investigate the  $\delta S2S^{Pd-S}$  values to check if they can still provide any other information. For this purpose, we normalize each curve by removing its mean and dividing it by the sum of its absolute values. The normalization results are shown in Figure 2-9d, e, and f. Interestingly, the normalized  $\delta S2S^{Pd-S}$  values present different trends within each EC8 class, but similar patterns can be recognized among different classes. Because we note that two different trends appear to cross at approximately 0.3 s in all classes (Figure 2-9d, e, and f), we assemble the  $\delta S2S^{Pd-S}$  normalized curves and classify them by a K-means analysis (Lloyd, 1982; Pedregosa et al., 2011).

## 2. Onsite Earthquake Early Warning: Predictive Models for Acceleration Response Spectra Considering Site Effects

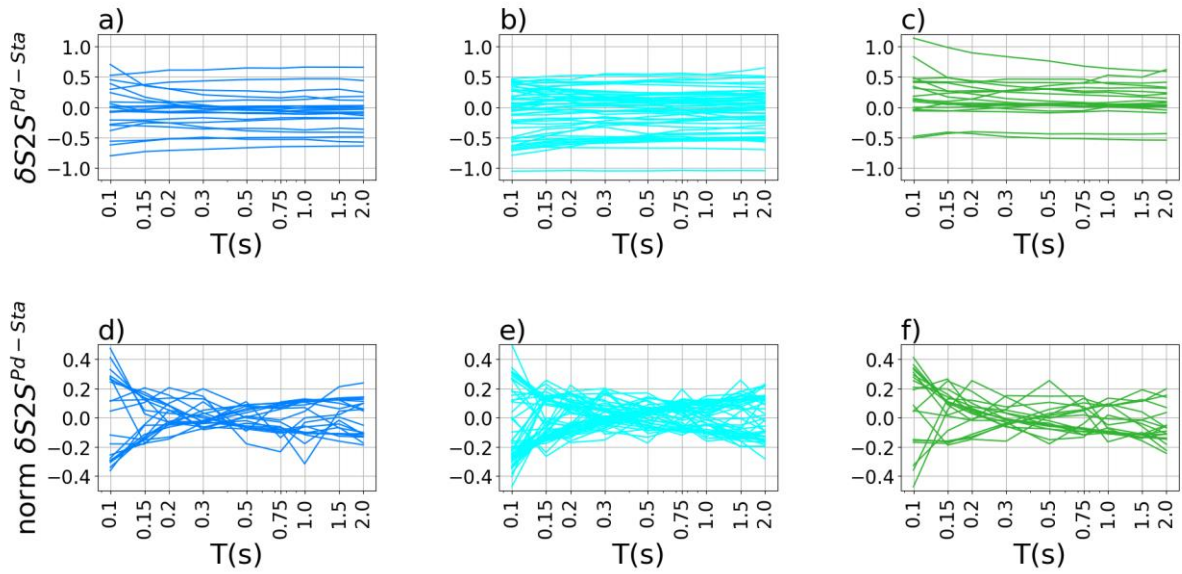


Figure 2-9:  $\delta S2S^{Pd-Sta}$  vs. period ( $T$ ). Each curve refers to a single station. a) Class A stations; b) Class B stations; c) Class C stations; d) 'Normalized' curves for Class A stations; e) 'Normalized' curves for Class B stations; f) 'Normalized' curves for Class C stations.

The K-means model is trained using data from 57 stations divided in sub-samples of 19 stations (the minimum class population size) for each class (A, B, and C), and with K equal to 3. Then, we apply the obtained model to the entire curve population. Figure 2-10 shows the  $\delta S2S_s^{Pd-Sta}$  normalized curves classified in the three new groups and colored by EC8 class. It is worth noting that each cluster presents a specific pattern ( $\delta S2S^{Pd-S}$  curve shape) formed by stations belonging to different EC8 classes. The first cluster (Figure 2-10a) presents a trend decreasing for a period; this suggests that at these stations the amplification of the RSA with respect to the median model decreases with the increase in period, which influences the higher frequencies. The second cluster (Figure 2-10b) shows the opposite behavior; these stations are prone to site effects at low frequencies. Finally, the third cluster (Figure 2-10c), which is the least populated, has a trend characterized by a broad central maximum; therefore, these stations amplify the ground motion in a wide intermediate frequency band. Looking at the cluster composition in terms of EC8 classes, as Class B stations are numerically dominant, the three clusters are mostly populated by Class B stations. Hence, there is not an objective relationship between clusters and classes. In conclusion, these results further confirm that the EC8 classification cannot discriminate the RSA site effect in the considered onsite EEW application.

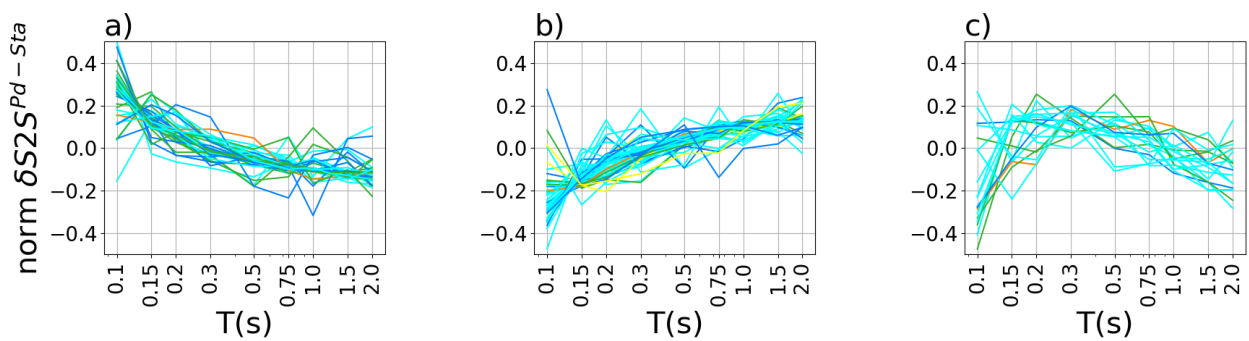


Figure 2-10: The three 'normalized' curves clusters obtained by the K-means clustering. Each curve is colored by station EC8 classification.

## 2. Onsite Earthquake Early Warning: Predictive Models for Acceleration Response Spectra Considering Site Effects

### 2.4.4 Implications of random effects for an onsite EEW decision alert system

We dedicate this final part of the work to show, by performing a retrospective analysis, the implications of including random effects in the Onsite EEW predictive models (Eqs. 3 and 5) with respect to the performance of a decision alert system. For this, we consider the ACT and T1244 stations (highlighted in Figure 2-1 and shown in Figure 2-2), which deviate from the median model (T1244 overestimates the predictions whereas ACT underestimates them). In the following, we discuss the case of Pd used as a proxy for RSA at the different periods through the predictive models of Eq. (3), whereas the results of the same analysis applied to IV<sup>2</sup> are presented in the supplemental material. There are twenty-one available recordings for the two considered stations, so that by considering each of the nine RSA periods as a single data point, we obtain a dataset composed by 189 observations (referred to as RSA<sub>obs</sub>), which are predicted either without considering the random effects  $\delta S_2 S^{Pd-S}$  (indicated in the following as RSA<sub>erg</sub>, whereas 'erg' stands for ergodic) or with random effects (referred to as RSA<sub>rand</sub>). The distribution of RSA<sub>obs</sub> is shown in Figure 2-11a, while Figure 2-11d shows the residuals between RSA<sub>obs</sub> and RSA<sub>erg</sub> (in blue) and between RSA<sub>obs</sub> and RSA<sub>rand</sub> (in red). As expected, the residuals of RSA<sub>rand</sub> are more closely distributed around zero than RSA<sub>erg</sub>.

To simulate a decision alert system, we set a threshold at the 80<sup>th</sup> percentile of our RSA<sub>obs</sub> distribution (RSA<sub>thres</sub> = 4.5\*10<sup>-3</sup> cm/s<sup>2</sup>, shown in Figure 2-11a as a black vertical bar). In this way, we know that whenever the RSA<sub>obs</sub> overcomes RSA<sub>thres</sub>, our hypothetical EEW system should release an alert (20% of the cases). Following Colombelli et al. (2015) and Minson et al. (2019), this approach allows us to assess the EEW system performance with respect to the following decision scheme: successful alarms (SA) require both observed and predicted (referred to as RSA<sub>pred</sub>, which can be either RSA<sub>rand</sub> or RSA<sub>erg</sub>) to be equal or larger than the selected threshold (RSA<sub>obs</sub> ≥ RSA<sub>thres</sub> and RSA<sub>pred</sub> ≥ RSA<sub>thres</sub>); idle, or not successful alarms (SNA) require both predicted and observed RSA to be below the threshold (RSA<sub>obs</sub> < RSA<sub>thres</sub> and RSA<sub>pred</sub> < RSA<sub>thres</sub>); missed alarms (MA) require RSA<sub>obs</sub> ≥ RSA<sub>thres</sub> but RSA<sub>pred</sub> < RSA<sub>thres</sub>; and finally, false alarms (FA) require RSA<sub>obs</sub> < RSA<sub>thres</sub> but RSA<sub>pred</sub> ≥ RSA<sub>thres</sub>. This notation for the EEW results was proposed by Colombelli et al. (2015), although in the literature we can find many similar definitions. Minson et al. (2019), for example, used "Alert" instead of "Alarm" and defined SA as "Correct alert" and SNA as "Correct no alert". Other works, such as Meier et al. (2017), used the classic logic classification where SA is "true positive", SNA is "true negative", MA is "false negative", and FA is "false positive". As previously discussed, our goal is to highlight a methodological issue (the role of site-effects in onsite EEW ground motion prediction) that does not depend on, or affect, the real-time application of an EEW system. Therefore, in the present analysis we refer to an ideal EEW system and we evaluate the performance of the calibrated EEW models in predicting ground motion when site effects are included or neglected. Furthermore, differently from (Meier, 2017), the lead-time is not discussed, while it will be considered in possible future real-time applications of the model.

2. Onsite Earthquake Early Warning: Predictive Models for Acceleration Response Spectra Considering Site Effects

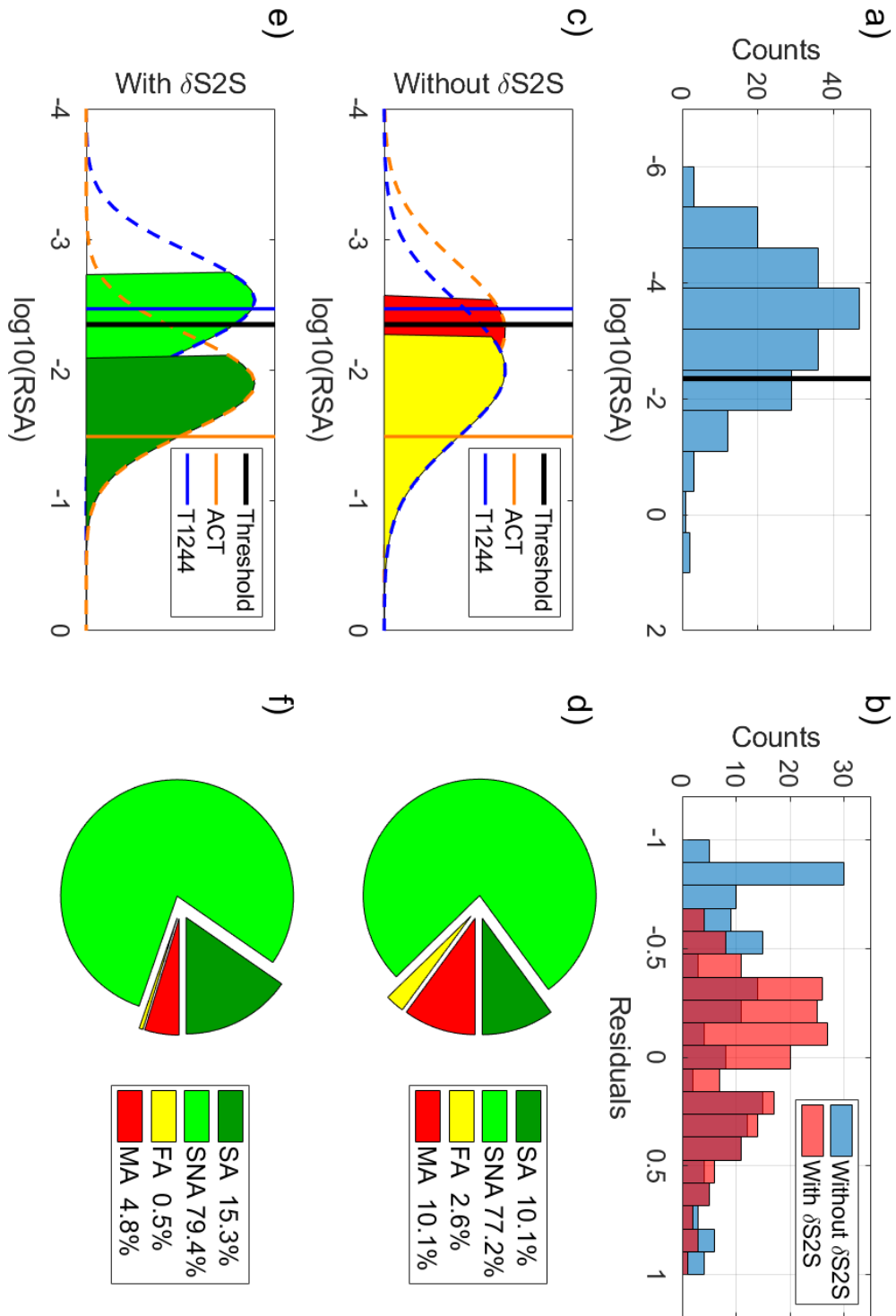


Figure 2-11: a) Distribution of observed RSA for all the periods for ACT and T1244 and for T equal to 0.5 s, and EEW RSA threshold (black vertical line). b) Observed and predicted RSA (from Pd with relation 3) for the 10/30/2016  $M_w$  6.5, Norcia earthquake at ACT and T1244 (orange and blue vertical line, respectively). EEW RSA threshold (black vertical line). Gaussian functions related to the predicted RSA for ACT and T1244 (orange and blue dashed line, respectively). The areas of the Gaussian functions are colored per an exceedance value of 0.70 according to the EEW performance, yellow for FA (station T1244), red for MA (station ACT). c) The same as (b) but including the random effects. The Gaussian functions are colored according to the EEW performance, light green for SNA (T1244) and dark green for SA (ACT). d) Histogram of the residuals distributions with (red) and without (blue) station corrections (random effects) for the dataset. e) EEW performance for the whole dataset without including the station corrections. f) The same as (e) but including the station corrections.

## 2. Onsite Earthquake Early Warning: Predictive Models for Acceleration Response Spectra Considering Site Effects

A further aspect that we investigate with our simulation is that, as discussed, a given level of uncertainty is always associated to EEW predictions through the predictive model itself. It is therefore reasonable to use a probabilistic approach when performing the comparison between the predicted ground motion and the threshold selected for the release of alerts (Minson et al., 2019). Therefore,  $RSA_{pred}$  should be considered along with the uncertainty of the predicted model ( $RSA_{pred}$  and the uncertainty allows us to set a probabilistic framework, whereas the alert is released only when the probability of exceedance of the considered threshold reaches a value selected by the EEW end users). Of course, selecting the probability of exceedance of an EEW system requires a cost-benefit analysis (Minson et al., 2019; Ruhl et al., 2019), but this is beyond the scope of this work, because we do not consider any specific EEW application and we mean to discuss a general principle. Hence, for simplicity, we consider an exceedance probability of 0.7 (70 percent) for the release of an alert. It is important to note that exceedance limits greater than 0.5 will favor the MAs with the respect to FAs.

Figure 2-11b shows an example of the decision module just outlined with respect to the recordings of the 10/30/2016  $M_w$  6.5 (Norcia earthquake, Figure 2-1) for the ACT (hypocentral distance  $R=27.2$  km) and T1244 ( $R=20.1$  km) stations at a period of 0.5 s (within the plot, the threshold is a black vertical line; the observed RSA values are vertical lines colored per station code; the predicted ergodic RSA values are two Gaussian functions with dashed lines colored according to the station code, and areas colored per the EEW performance using, the red for MA and yellow for FA). Looking at station T1244 in Figure 2-11b,  $RSA_{obs}$  (blue vertical line) is lower than  $RSA_{thres}$  (black vertical line); thus, the EEW system should not issue an alert. Concerning the predicted  $RSA_{erg}$ , which is represented as a Gaussian function (blue dashed line) with mean equal to  $RSA_{erg}$  and sigma equal to  $\sigma^{Pd-S}$  (see Table 2-3 for  $T = 0.5$  s), we highlighted the area corresponding to the selected exceedance probability (0.70). Because the  $\delta S2S^{Pd-S}$  of T1244 is negative (as shown in Figure 2-3), the prediction of the median model is over-estimated, leading the EEW prediction to be larger than the threshold over the exceedance limit which, in turn, leads the EEW system to fail (FA case). On the contrary, when the RSA prediction includes the random-effect term (Figure 2-11c), the variability to be considered is  $\sigma_{SS}^{Pd-S}$ , and the previous FA becomes a correct SNA (light green area).

If we consider the ACT station, we observe the opposite behavior in terms of EEW performance. In this case, the  $RSA_{obs}$  (orange vertical line) is larger than  $RSA_{thres}$ , indicating that this is a critical event for which an alert to users is necessary. However, Figure 2-11b shows that, if the median model is used, the  $\delta S2S^{Pd-S}$  is positive for this station, and the predicted data (orange dashed Gaussian function) are under-estimated, which leads the EEW system to fail with an MA. By contrast, Figure 2-11c shows that, as for the previous station, it is beneficial to include the random effects. By adding the mixed-effect term, the new prediction overcomes the  $RSA_{thres}$  and the EEW system provides a correct alert (SA). These two examples show that the mixed-effect terms improve the EEW results in two ways: they decrease the residuals between real and predicted data, and they decrease the prediction uncertainty.

Finally, Figure 2-11e and f show the total performance of the EEW system without and with the mixed-effect terms, respectively (considering the whole dataset). Already at a first glance, the performance improvement of the system is evident. Interestingly, the FA alarms drops from 2.6% to 0.53%, while the MAs decrease from the 10.1% to 4.8% while, clearly, both the SAs and SNAs increase from 10.1% and 77.2% to 15.1% and 79.4%.

## 2. Onsite Earthquake Early Warning: Predictive Models for Acceleration Response Spectra Considering Site Effects

### 2.5 Conclusion

In this study, we developed partially non-ergodic, site-specific onsite early warning models for spectral ordinates (RSA) at different periods ( $T$ ). We used waveforms belonging to the 2016–2017 Central Italy sequence, which provided us with many high-quality recordings per station for magnitudes ranging between  $M_w$  3.8 and  $M_w$  6.5. This dataset is representative for onsite EEW applications in regions where the seismic hazard for residential buildings is dominated by close-distance earthquakes of small-to-moderate magnitudes.

We derived four onsite EEW prediction relationships for RSA at nine periods, considering the peak displacement and the velocity integral squared over an early P-wave window, and introducing station- or EC8 class-specific adjustments through mixed-effects regression. The analysis of the station-specific random effects confirms that the onsite EEW benefits from the introduction of a partially non-ergodic approach. Indeed, the random effects  $\delta S2S^s$  permit capturing the period-dependent site amplifications and reducing the aleatory variability. On the other hand, considering the EC8 classification has proven to be ineffective for describing the site effects for the RSA in EEW applications due to the large within-group variability. Even considering the trend of the random effects ( $\delta S2S^s$ ) as a function of the period, our analysis confirmed that EC8 classification is unrelated to the site effects on RSA. This was also confirmed by a cluster analysis performed on the period-dependent  $\delta S2S^s$ , which provided three groups totally unrelated to the EC8 class of the stations within the groups. In conclusion, the EC8 classification cannot be exploited in EEW applications to discriminate site effects in RSA predictions. With regard to the two considered P-wave features for developing onsite EEW models, the results of the cross-validation analysis have shown that the RSA predictions associated to  $IV^2$  are more precise than those derived from  $P_d$ .

One of the main results of our study is that considering both  $P_d$  and  $IV^2$ , the predictive onsite EEW models that include the station random effects provide more robust predictions of the RSA amplitudes with respect to the customary ergodic approaches. This latter aspect has also been shown through a probabilistic alert decision module applied to the data of two stations. Indeed, the performance of onsite EEW applications where the predictive models include site-effects highlights how they can provide more precise alerts. The approach presented in this study would permit, therefore, obtaining real-time ground motion predictions tailored to given target conditions (less affected by site-effects) and, hence, it would lead to more efficient onsite EEW. In conclusion, given the great importance of the uncertainty associated to the ground motion level predicted at a target site in EEW applications, we believe that future onsite EEW applications should consider strategies to reduce the role of site-effects.

### 3. Earthquake Early Warning System for Structural Drift Prediction using Machine Learning and Linear Regressors

Antonio Giovanni Iaccarino<sup>1</sup>, Philippe Gueguen<sup>2</sup>, Matteo Picozzi<sup>1</sup>, and Subash Ghimire<sup>2</sup>

<sup>1</sup> Università degli studi di Napoli, Federico II, Dipartimento di Fisica “Ettore Pancini”, Napoli, Italia

<sup>2</sup> Université Grenoble Alpes, Université Savoie Mont Blanc, CNRS, IRD, IFSTTAR, ISTerre, Grenoble, France

Submitted in *Frontiers in Earth Science* (Iaccarino et al., 2021)

doi: 10.3389/FEART.2021.666444

### 3. Earthquake Early Warning System for Structural Drift Prediction using Machine Learning and Linear Regressors

#### 3.1 Introduction

Seismic risk is one of the main concerns for public authorities in seismic prone regions. Earthquake Early Warning Systems (EEWSs) are complex infrastructures that can mitigate the seismic risk of citizens and losses by the rapid analysis of seismic waves (Gasparini et al., 2011). Typically, EEWS analyzes seismic data in real-time for automatically detects and predict the earthquake size using the first seconds of P-wave signals. Generally, by these pieces of information, EEWSs attempt predicting the ground motion (e.g., Peak Ground Acceleration, PGA) at specified targets. Hence, EEWSs disseminate alerts to targets where the shaking intensity is expected to overcome a damage threshold.

There are two main families of EEWS: onsite and regional systems (Satriano, Wu, et al., 2011). The onsite approaches use a single station, or a small seismic network, installed near the target. On the other hand, in regional systems, a seismic network is placed near the seismogenic zone, which normally is placed sufficiently far from the target area to protect. Furthermore, onsite systems use P-waves information to directly predict ground motion through empirical scaling laws, while regional ones exploit primarily P-waves, but also S-waves information, from stations close to the epicenter for estimating the source location and magnitude, which in turn are feeding GMPEs (Ground Motion Prediction Equation) for predicting the ground motion at targets.

A fundamental EEWS parameter is the time available to mitigate the seismic risk at a target before damaging ground motion related to S-waves or surface waves reach it (hereinafter called 'lead-time'). Depending on the hypocentral distance between seismic source and target, the lead-time of the EEWS approaches is different: at higher distances, the lead-time is greater for regional systems; at shorter distances, onsite EEWSs are faster and can provide useful alerts when the regional systems fail (Satriano, Wu, et al., 2011).

In the last two decades, several works have proposed the use of P-wave features in onsite EEW framework. Wu and Kanamori (2005) proposed the inverse of the predominant period,  $\tau_c$ , measured on the first 3s of P-wave waveforms to predict the magnitude. The same authors have also proposed the Peak of Displacement,  $P_d$ , on 3s window to predict the Peak Ground Velocity, PGV (Wu and Kanamori, 2008). Brondi et al. (2015) used the  $P_d$  and the Integral of squared Velocity,  $IV^2$  to predict the PGV and the Housner Intensity,  $I_H$ . Spallarossa et al. (2019) and Iaccarino et al. (2020) explored the use of  $P_d$  and the  $IV^2$  and for predicting PGV and the Response Spectra of Acceleration, RSA, amplitudes at nine periods, respectively, using a mixed-effect regression approach aiming to account for site-effects.

Besides the ground motion in free field, recently, efforts to predict the structural response in EEWS applications have also been proposed (i.e., applications where the Structural Health Monitoring, SHM, meets the EEWS goal to disseminate real-time alerts). The outputs of these methods can, for instance, trigger automatic isolation systems (Chan et al., 2019; Lin et al., 2020) based on damage level predictions through Engineering Demand Parameters (EDP). For example, Picozzi (2012) proposed to combine P-wave features with the structural building response retrieved by interferometry and a multi-sensors system (Fleming et al., 2009) to predict both the earthquake parameters and the structural response. Kubo et al. (2011) proposed a built-in EEWS for buildings that is able to automatically stop the elevator, start an acoustic alert at each floor, and predict displacement intensity and story drift angle at each floor. In perspective, the use of new advanced technologies, such as Internet of Things and 5G, will significantly facilitate for the easy and huge implementation of such systems (D'Errico et al., 2019).

This work aims to explore the use of P-wave parameters (i.e.,  $P_d$ ,  $IV^2$  and the integral of squared displacement,  $ID^2$ ) to predict the structural response in onsite EEWS applications. In particular, following Astorga et al. (2020), we considered the drift ratio (Dr) as a robust and reliable parameter to link in the

### 3. Earthquake Early Warning System for Structural Drift Prediction using Machine Learning and Linear Regressors

building response. The parameter  $Dr$  is computed as the relative displacement between two sensors in the building (one placed at the top floor and the other at the bottom floor of the building) divided by the height difference between the sensors.

To this purpose, we investigated the performance of different algorithms to develop robust empirical model between our EEWS parameters and  $Dr$ . Specifically, we explored both Least Square Regression (LSR) and Machine Learning (ML) techniques. Since Mignan and Broccardo (2019) have demonstrated that complex ML models are often overused, one of our goal is to verify whether MLs, considering their complexity and the difficulties in a suitable training, provide advantages or not with respect to simpler linear models in EEW applications.

We investigated four different machine learning regressors: Random Forest (RF, Breiman, 2001), Gradient Boosting (GB, Friedman, 2001), Support Vector Machine (SVM, Cortes and Vapnik, 1995) and K-Nearest Neighbors (KNN, Altman, 1992). These MLs are used to parameterize models aiming to predicting  $\log_{10} Dr$  from the three P-wave proxies and three time-windows (i.e., 1, 2, and 3 seconds). For each regressor, we tune two hyper-parameters by comparing the results of K-fold cross-validation (with  $K=5$ ) using the training set (Stone, 1974). Then, the best hyper-parameters set is used to train the ML algorithms with the entire training set (i.e., 80% of the data), and finally, we test their performance with a testing set (i.e., 20% of the data). This procedure allows us to assess in a robust way the regression performance. In parallel, we calibrated models also using linear least square regressors (LSR). To this aim, we used two strategies: we calibrated LSR models for single P-wave features (i.e., three P-wave proxies times three time-window lengths); we used all the features together for calibrating LSR models, mimicking what is done for ML. Therefore, we compare the ML performance with the LSR models.

The calibration and performance analysis are carried out by progressive steps, where the complexity of the dataset is increased at each step. In the first analysis, we focused on the Shiodome Annex (ANX) building, a Japanese Steel-Reinforce-Concrete (SRC) building. With its 20 years-long history of earthquakes recording, ANX represents the perfect starting case study to understand the capabilities of the methods.

In the second step, we considered all the Japanese SRC buildings. The rationale in this choice is that, even if they are of the same typology of ANX, we expect that the combination of the buildings response with different site conditions can contribute to inflate the drift variability.

Finally, in the third step we used the complete Japanese dataset, and we performed a residuals analysis de-aggregating them for building and earthquake characteristics. The aim of this last analysis is to explore the possibility of retrieving correction factors that in future EEW applications can be used for improving the drift predictions.

Finally, we verified the validity of the ergodic assumption for the EEWS calibrated models, a typical problem in seismology when models calibrated for a region are applied to data in other areas. To this aim, we applied the models calibrated using the Japanese dataset to the waveforms recorded in U.S. buildings.

### 3. Earthquake Early Warning System for Structural Drift Prediction using Machine Learning and Linear Regressors

#### 3.2 Datasets and methods

##### 3.2.1 Datasets

We consider 3-components waveforms recorded at Japanese and U.S. buildings (Astorga et al., 2020). The considered buildings belong to three different types of construction (Table 3-1): steel (ST), reinforced concrete (RC) and steel-reinforced concrete (SRC, only Japanese buildings). All buildings have one sensor at the ground floor and one at the top floor. We measure P-waves EEW parameters ( $P_d$ ,  $IV^2$ ,  $ID^2$ ; hereinafter we refer to them in general way as XP parameters) for different signal lengths (i.e., 1, 2 and 3 seconds) from the station at the ground level, while  $Dr$  is measured using both sensors.

The Japanese dataset (Figure 3-1a) is made up by 5,942 waveforms collected from 2,930 earthquake recorded at 34 buildings. The magnitude of the events, from the Japan Meteorological Agency (JMA), ranges from  $M_{JMA}$  2.6 to  $M_{JMA}$  9, and the epicentral distances vary between 2.2 km and 2514 km.

The US dataset (Figure 3-1b) is formed by 240 waveforms from 90 events recorded at 69 buildings. The magnitude of these events ranges from  $M_w$  3.5 to  $M_w$  7.3, while the epicentral distance ranges from 2.7 km to 391 km.

Table 3-1 presents the buildings classification according to construction material and height. The largest set of data is available for ANX (Figure 3-1a), an SRC building in Japan that includes 1,616 waveforms recordings. Since the height is considered important in determining the buildings response, we used the number of floors to divide the dataset into two categories: 1) low-rise buildings when the number of floors is less than eight; 2) high-rise buildings for the others. This classification is similar to the one done in Astorga et al., 2020, but, here, low-rise and mid-rise categories are merged in the low-rise category.

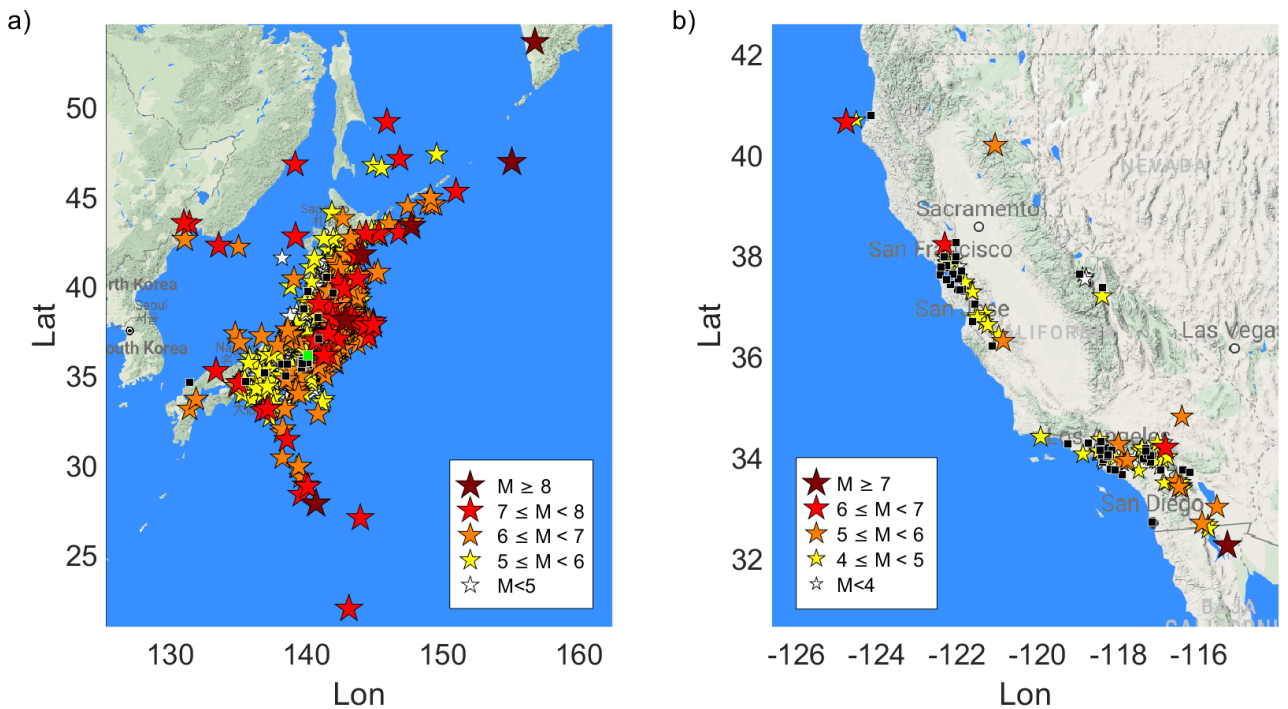


Figure 3-1: Map of the dataset used in the study. The stars indicate the events, the color and the size refer to the magnitude following the legends in the figure. The black squares indicate the buildings, the green one in figure a) is the ANX building.

### 3. Earthquake Early Warning System for Structural Drift Prediction using Machine Learning and Linear Regressors

Table 3-1: Dataset summary

	Japanese dataset		US dataset	
	Low-rise	High-rise	Low-rise	High-rise
RC	10	3	13	9
SRC	5	7	0	0
ST	1	8	28	19

#### 3.2.2 P-wave features

Waveforms are filtered using a narrow bandpass Butterworth filter between the frequencies 0.5 Hz and 2 Hz. This choice was made following Astorga et al. (2019) and is motivated by the aim of selecting signals that are strongly related to the structural response. Indeed, for the building as those considered in this study the co-seismic fundamental frequency is usually within this range (Astorga et al., 2020).

Since our objective is to calibrate models for onsite EEW application, we considered as proxy of drift parameters estimated from P-wave signal windows of limited lengths (i.e., 1, 2 and 3 seconds after the P-waves first arrival). The rationale behind this choice is that the three time-windows can allow to capture the temporal evolution of the drift, and also to assess the consistence/robustness of the estimates in time. Furthermore, selecting a fixed time window length in EEW systems is not a trivial task. Indeed, two contrasting effects play a role in taking this decision. From one hand, the signal windows should be as shorter as possible to increase the lead-time. On the other hand, since the rupture duration increases with magnitude, selecting too short time-windows lead to the saturation of the prediction, which results in wrong prediction for large earthquakes (i.e., in analogy with the typical magnitude saturation problem in seismology). In this study, using time windows with maximum length equal to 3 seconds, we expect our P-wave proxies to saturate around magnitude  $M_w$  7 (e.g., Yamada and Mori, 2009).

To assess the structural response, we consider the dimensionless structural drift,  $Dr$ , defined as (Astorga et al., 2020)

$$Dr = (PTD - PGD)/h \quad (1)$$

where  $PTD$  is the Peak of Displacement in the top of the building,  $PGD$  is the Peak of Displacement at the ground level of the building and  $h$  is the distance between the two sensors.

Concerning the P-waves features, we rely on the peak of displacement ( $Pd$ ), the integral of the squared velocity ( $IV^2$ ) and the integral of the squared displacement ( $ID^2$ ).

These features are computed on the vertical component following Iaccarino et al. (2020):

$$ID^2 = \int_{t_p}^{t_p+\tau} d^2(t) dt \quad (2)$$

$$IV^2 = \int_{t_p}^{t_p+\tau} v^2(t) dt \quad (3)$$

### 3. Earthquake Early Warning System for Structural Drift Prediction using Machine Learning and Linear Regressors

$$Pd = \max_{t_p \leq t \leq t_p + \tau} |d(t)| \quad (4)$$

where  $t_p$  is the first arrival time,  $\tau$  is the window length,  $d(t)$  is the displacement, and  $v(t)$  is the velocity.  $Pd$  is measured in cm,  $IV^2$  in  $\text{cm}^2/\text{s}$  and  $ID^2$  in  $\text{cm}^2 \cdot \text{s}$ . Since we measure these three XPs on three different windows, we have a total of nine different features:  $ID^2_{1s}$ ,  $ID^2_{2s}$ ,  $ID^2_{3s}$ ,  $IV^2_{1s}$ ,  $IV^2_{2s}$ ,  $IV^2_{3s}$ ,  $Pd_{1s}$ ,  $Pd_{2s}$ ,  $Pd_{3s}$ .

#### 3.2.3 Case studies

The availability of two rich datasets, relevant to two countries with different building typology and tectonic contexts, motivated us to explore the effect of the dataset complexity in the robustness of EEW model predictions. It is quite common in seismology, and especially in EEW applications, to use an ergodic approach in the use of EEW models. In other words, models calibrated combining datasets from different regions are exported to further areas assuming that regional effects do not play role in the model uncertainty (Stafford, 2014). However, results of recent EEW studies (e.g., among others Spallarossa et al., 2019; Iaccarino et al., 2020) have shown the opposite; that is to say, regional characteristics can play an important role in the robustness and accuracy of the EEW predictions, leading to increase the epistemic uncertainty (Al Atik et al., 2010). For this reason, we proceeded setting 4 different case studies using datasets of increasing order of heterogeneity. We started calibrating EEW models from a specific building (i.e., ANX in Japan); then, we moved forwards including more buildings from the same typology and region (i.e., SRC from Japan); and then, the same region but with different construction typology. Finally, we applied the models calibrated with Japanese data to those recorded at U.S. buildings. Our strategy of assessing the performance of LSR and ML models in progressively harder conditions (i.e., varying dataset size and composition) aims to unveil eventual drawbacks and limitations in their use.

To set a robust assessment of the models calibrated by different approaches (i.e., ML and linearized algorithms) and datasets (i.e., #1 ANX, #2 SRC-JAPAN, #3 all JAPAN buildings, #4 U.S. buildings), we define a training set (80% of the data) and a testing set (20% of the data) for each of the case studies. In all cases, the data for training and testing are selected by randomly splitting the dataset. The training set is used to tune the model parameters. Then, the trained model is used to predict the drift of the testing set. This will provide a trustworthy way to compare LSR and ML models. This procedure will avoid any bias in the evaluation of the models.

Case 1. The ANX building is considered for a building specific analysis (i.e., the same site conditions and building features characterize all the data). Therefore, the variability of data in terms of amplitude and duration length is, in this case, due to only the within-event and aleatory variability (Al Atik et al., 2010).

Case 2. In the second step of our analysis, we considered the dataset formed by all the data from SRC buildings in Japan. This second dataset is made up by 3,086 waveforms from 2,034 events and 12 buildings (of course including also ANX). This analysis, thus, allows us to study the variability related to different site conditions and building responses.

Case 3. We considered the complete Japanese dataset. With respect to the previous one, this dataset also includes the complexity due to differences in the seismic response between different types of construction.

Case 4. We studied the implications of exporting the retrieved model for Japan to another region. To do this, we apply the models trained on the Japanese dataset to the U.S. dataset. Clearly, this application is expected to be the more difficult since different aspects can play a role in degrading the model prediction capability. First of all, there are well-known tectonic and geological differences between

### 3. Earthquake Early Warning System for Structural Drift Prediction using Machine Learning and Linear Regressors

Japan and California. The main difference is that the former is a subduction zone with a prevalence of thrust earthquakes, while, in the latter, most of the earthquakes are associated to strike-slip faults. Another important aspect to account for is that differences may exist within the building type of construction, due to different building design codes between Japan and USA.

#### 3.2.4 Linear least square regression

The selected nine  $XP_w$  (see subsection 3.2.2) are strongly covariant, since they are relevant to the same P-wave signals observed in different domains (i.e., displacement, and velocity) and time (i.e., 1, 2 and 3 seconds). While ML techniques can address this issue, the LSR approaches are prone to problems in cases where the dependent variables are correlated each other. For this reason, we applied the LSR in two different ways.

In the first approach, we used the features separately. This leads us to have nine different linear models that, for the sake of simplicity, have the same functional form, as:

$$\log_{10} Dr = a + b * \log_{10} XP_w \quad (7)$$

where  $XP_w$  can be any of the P-wave parameters (Eqs. 2, 3 and 4) at a specific window-length  $w$  (i.e., 1, 2 or 3 seconds). We will refer to these models as “LSR  $XP_w$ ”.

For all these techniques, we calibrated ML models by adopting an approach that mimics increase of information with time typical of EEW applications (i.e., the temporal evolution of time-windows in 1s, 2s, and 3s). In particular, for the first time-window (1s), we use only the 3 P-wave parameters available at that time. For the second time-window (2s), we consider the information available at this moment (i.e., the features at 1s and 2s, for a total of 6 features). Finally, for the 3s window, we use all 9 features.

In the second approach we mimic the increasing of information with time typical of EEW applications (i.e., the temporal evolution of time-windows in 1s, 2s, and 3s). In particular, for the first time-window (1s), we use only the 3 P-wave parameters available at that time. For the second time-window (2s), we consider the information available at this moment (i.e., the features at 1s and 2s, for a total of 6 features). Finally, for the 3s window, we use all 9 features. We will refer to three combined models as “LSR $_w$ ”.

In total, we will compare 12 linear models.

#### 3.2.5 Machine Learning regressors

As previously said, we use four different ML techniques: Random Forest (RF, Breiman, 2001), Gradient Boosting (GB, Friedman, 2001), Support Vector Machine (SVM, Cortes and Vapnik, 1995) and K-Nearest Neighbors (KNN, Altman, 1992). In this section, we shortly present them focusing on hyper-parameters tuned by a K-fold cross validation. Of course, we refer to the referenced works for their deeper understanding.

##### *RF regressor*

RF regressor (Breiman, 2001) is an ensemble of a specified number of decision tree regressors ( $N_{tr}$ ). A decision tree regressor works as a flow-chart in which, for each node, a feature is selected randomly to subdivide the data in two further nodes through a threshold. This latter is chosen to minimize the node impurity, as follows:

### 3. Earthquake Early Warning System for Structural Drift Prediction using Machine Learning and Linear Regressors

$$I = \frac{1}{N} \sum_{i=1}^N (y_i - \hat{y})^2 \quad (5)$$

where  $N$  is the number of the training data in the node,  $y_i$  is the real value of the target for the  $i$ -th datum and  $\hat{y}$  is the predicted value of the end node in which the  $i$ -th point is assigned. The predicted value of the end node is simply the mean value of the data in the end node itself. The depth of the trees is controlled by a tolerance factor that stops the subdivision procedure if the gain in impurity is not enough, or by reaching a maximum depth value  $M_{\text{dep}}$ . The final regression is given by the average prediction of all the trees. We select  $N_{\text{tr}}$  and  $M_{\text{dep}}$  as the hyper-parameters to tune.

#### *GB regressor*

In a similar way to RF, the GB regressor is an ensemble of  $N_{\text{tr}}$  decision tree regressors (Friedman, 2001). The main difference between the two is that in GB the steepest descent technique is applied to minimize a least square loss function. In this algorithm, each decision tree plays the role of a new iteration, while the procedure is controlled by the hyper-parameter learning rate ( $L_r$ ). From preliminary studies, we decide to fix  $N_{\text{tr}}=300$  and we tune  $M_{\text{dep}}$  and  $L_r$ .

#### *SVM regressor*

The SVM regressor searches the best hyperplane to predict the target value also minimizing the number of predictions that lies outside an  $\epsilon$ -margin from the hyperplane (Cortes and Vapnik, 1995). The result is achieved solving the problem:

$$\min_{\omega, b, \xi} \left[ \frac{1}{2} \omega^T \omega + C \sum_i (\xi_i + \xi_i^*) \right] \quad (6)$$

where  $\omega \in \mathbb{R}^p$  and  $b \in \mathbb{R}$  are the linear regression parameters for  $p$  features,  $C$  is a penalty factor, and  $\xi_i, \xi_i^*$  are positive slack variables representing the distance from the lower or the upper margins. It is worth to note that the slack variables ( $\xi_i$  and  $\xi_i^*$ ) are both non-zero only if the datum lies inside the margins. Furthermore, to include any nonlinear trends, we used a gaussian kernel with  $\sigma_{\text{SVM}}$  as variance. In summary, the main hyper-parameters for this technique are  $\epsilon, C$  and  $\sigma_{\text{SVM}}$ . Looking at preliminary testing results, we fixed  $\epsilon=0.1$  and we tuned  $C$  and  $\sigma_{\text{SVM}}$ .

#### *KNN regressor*

Finally, the KNN regressor predicts the target of a certain datum as the weighted average of the  $K_N$  nearest data target, where the weights are the opposite of the distance (Altman, 1992). This technique is a lazy learner because the training step consists only in the memorization of a training set. We use the Minkowski distance of order  $P$  (van de Geer, 1995). We use  $K_N$  and  $P$  as hyper-parameters to tune.

For all these techniques, we calibrated ML models by adopting an approach similar to the one adopted for combined LSR models. That is to say, we will use all the available features at each second (i.e., 3 features at 1s, 6 at 2s and, finally, 9 features at 3s) to calibrate the ML models. In this way, we have three configurations for each ML regressor with a total of 12 ML models. Hereinafter, we will refer to these models as  $ML_w$ , where  $ML$  can be RF, GB, SVM or KNN, and  $w$  is the time window used.

#### *Validation process*

For all ML methods, we apply the logarithm base 10 to all the features and then we standardize them to have a unit variance. For each ML algorithm, we apply a  $K$ -fold cross-validation (Stone, 1974) on the training set with  $K=5$  for each set of hyper-parameters. We use the coefficient of determination  $R^2$  as comparative score, so as to find the optimal configuration for each model. This effort is done to avoid two critical issues that are well-known with ML techniques: underfitting and overfitting (Dietterich, 1995; Hawkins, 2004; Raschka and Mirjalili, 2017). A model is underfitted when it is too simple and is not able to retrieve good predictions even on the training set (e.g., this can happen also when LSR is performed on strongly non-

### 3. Earthquake Early Warning System for Structural Drift Prediction using Machine Learning and Linear Regressors

linear databases). On the other hand, a model is overfitted when it performs very well on the training set but presents a lack of accuracy on the testing set. This problem arises when a model is so complex that it results too linked with the training data variability.

#### 3.3 ANX and SRC analysis

In this section, we analyze the EEW models calibrated considering the ANX and SRC buildings subsets.

##### 3.3.1 Least Square Regression models

As said above, we develop 12 linear models (i.e., derived combining three P-wave proxies and three different windows, and the combined LSR models) for the two datasets. As example, we show in Figure 3-2 the results of the regression performed for  $Pd$  considering the three windows on the ANX. Figure 3-2 shows that both the training set (grey circles) and testing set (green triangles) have the same variability around the fit. We report the results of all the linear regressions, for ANX in Table 3-2, and for SRC in Table 3-3, whereas the first two columns report the regression parameters as in Eq. 7. Moreover, the third column,  $\sigma_{\text{train}}$ , contains the standard deviation of the residuals for the training set, while the fourth column,  $\sigma_{\text{test}}$ , contains the same but for the testing set. Finally, in the last two columns, we report the  $R^2$  value for training and testing sets.

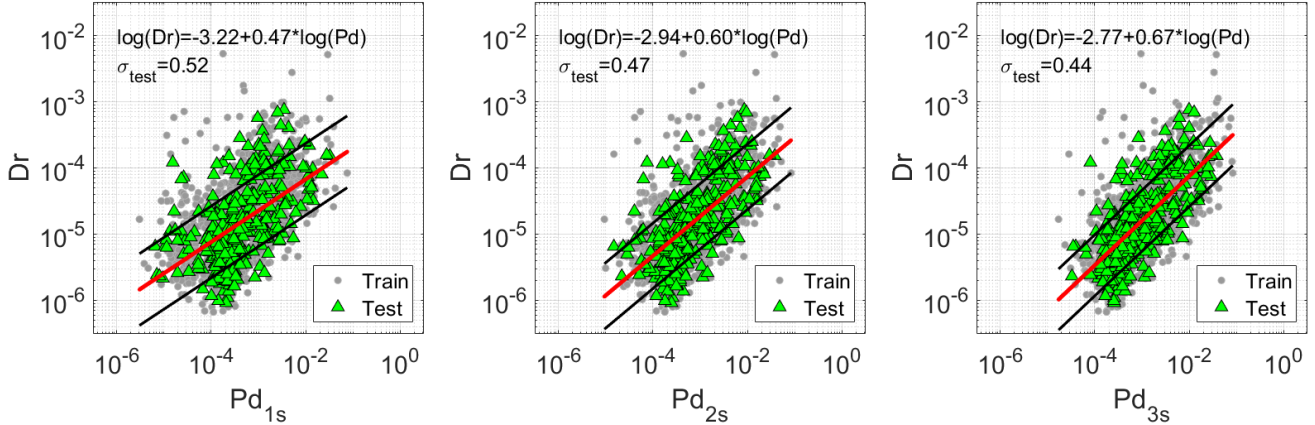


Figure 3-2:  $Dr$  versus  $Pd$  (cm) of the ANX dataset for three different windows. Gray dots refer to train set data. Green dots refer to test set data. The red lines are the least square regression performed for the train set. The black lines, instead, represent the  $\pm\sigma_{\text{train}}$  confidence level. The equation of this line is written in the upper part of each figure with its own test residual variability,  $\sigma_{\text{test}}$ .

Looking at the results shown in Table 3-2 (i.e., ANX), the models perform slightly better on the testing set both in terms of  $\sigma$  and  $R^2$ . This difference is probably due to the different amount of data within the two sets. It is worth to note that the prediction improves with the increasing of the window length for all the models, i.e., looking at  $Pd$ ,  $\sigma_{\text{test}}$  is 0.52 at 1s, 0.47 at 2s and 0.44 at 3s. In the end, comparing XPs, we note that  $IV^2$  and  $Pd$  have similar performances, while  $ID^2$  is the worst. The combined models perform always better than the single-feature models looking window-by-window.  $LSR_{3s}$  provides the best performances with  $\sigma_{\text{test}}=0.39$  and  $R^2_{\text{test}}=0.60$  (these values are bolded in Table 3-2).

### 3. Earthquake Early Warning System for Structural Drift Prediction using Machine Learning and Linear Regressors

From Table 3-3, we can note that the performance of the LSR models for the Japanese SRC buildings is always slightly worse than that for ANX. This result is probably due to the increase in the between-buildings variability of the observations, that can also be affected by different site conditions (we will focus on this important aspect in the following section). An improvement of predictions with the time window lengths is again observed. In this case, the combined models improve the predictions only for 2s, and 3s windows. Finally, we obtain again the best results for LSR<sub>3s</sub> with  $\sigma_{\text{test}}=0.46$  and  $R^2_{\text{test}}=0.51$  (bolded in Table 3-3).

We show, in Figure 3-3, the predicted Dr versus the real Dr using the LSR model calibrated using the combined model LSR<sub>w</sub> for the three windows on the ANX (Figure 3-3a-c) and SRC (Figure 3-3d-f) testing datasets as red triangles. We also plot the standard deviation references as red dashed lines. From these results, we can see the improving of the performances due to the increasing of the window length.

Table 3-2: Least square regression results, ANX dataset

$XP_w$	<b>a</b>	<b>b</b>	$\sigma_{\text{train}}$	$\sigma_{\text{test}}$	$R^2_{\text{train}}$	$R^2_{\text{test}}$
$ID^2_{1s}$	-3.41	0.21	0.56	0.54	0.22	0.25
$ID^2_{2s}$	-3.13	0.27	0.51	0.49	0.35	0.39
$ID^2_{3s}$	-3.01	0.31	0.48	0.46	0.43	0.46
$IV^2_{1s}$	-3.56	0.22	0.54	0.52	0.27	0.31
$IV^2_{2s}$	-3.42	0.27	0.49	0.47	0.40	0.43
$IV^2_{3s}$	-3.34	0.30	0.46	0.44	0.46	0.49
$Pd_{1s}$	-3.22	0.47	0.54	0.52	0.26	0.29
$Pd_{2s}$	-2.94	0.60	0.49	0.47	0.39	0.43
$Pd_{3s}$	-2.77	0.67	0.46	0.44	0.47	0.50
$LSR_{1s}$			0.53	0.51	0.30	0.34
$LSR_{2s}$			0.44	0.43	0.51	0.53
$LSR_{3s}$			0.41	<b>0.39</b>	0.57	<b>0.60</b>

### 3. Earthquake Early Warning System for Structural Drift Prediction using Machine Learning and Linear Regressors

Table 3-3: Least square regression results, SRC dataset

$XP_w$	<b>a</b>	<b>b</b>	$\sigma_{train}$	$\sigma_{test}$	$R^2_{train}$	$R^2_{test}$
$ID^2_{1s}$	-3.25	0.22	0.53	0.54	0.32	0.33
$ID^2_{2s}$	-3.17	0.26	0.50	0.51	0.41	0.40
$ID^2_{3s}$	-3.14	0.28	0.47	0.48	0.47	0.46
$IV^2_{1s}$	-3.49	0.22	0.53	0.54	0.34	0.33
$IV^2_{2s}$	-3.47	0.25	0.49	0.51	0.42	0.41
$IV^2_{3s}$	-3.47	0.27	0.47	0.48	0.47	0.47
$Pd_{1s}$	-3.18	0.47	0.52	0.54	0.35	0.33
$Pd_{2s}$	-3.08	0.54	0.49	0.51	0.43	0.39
$Pd_{3s}$	-3.03	0.58	0.46	0.49	0.49	0.45
$LSR_{1s}$			0.52	0.54	0.36	0.33
$LSR_{2s}$			0.46	0.49	0.49	0.45
$LSR_{3s}$			0.44	<b>0.46</b>	0.54	<b>0.51</b>

#### 3.3.2 Machine Learning Regression

Table 3-4 and Table 3-5 report the results for 12 ML regression models (see section 3.2.5) for the ANX and SRC datasets, respectively. In these tables, each row refers to a different  $ML_w$ . The parameters  $\sigma_{train}$  and  $R^2_{train}$  are the mean of the same parameters obtained by the K-fold cross-validation on the training set. After the training, we apply the calibrated models to the testing dataset.

Looking at Table 3-4,  $\sigma_{test}$  and  $R^2_{test}$  are in general equal or slightly better than the values for the training set. A similar result has been observed also in the least square regression analysis (Table 3-2). Since our predictions do not worsen on the testing set, we are confident that we are avoiding overfitting. Furthermore, applying ML analyses, the prediction performance is improved by using the longest time window available. Lastly,  $SVM_{3s}$  is the best ML among the tested ones, with  $\sigma_{test}=0.37$  and  $R^2_{test}=0.64$  (bolded in Table 3-4).

As for the least square regression analysis results, also in this case we observe that drift prediction worsens increasing the building numbers (i.e., going from ANX to SRC buildings). This result shows us that despite buildings are of the same construction typology, the varying site conditions can play a significant role in increasing the drift estimates variability. As for the ANX analysis, the SVM technique provides the best Dr predictions; in particular,  $SVM_{3s}$  provides the best model with  $\sigma_{test}=0.42$  and  $R^2_{test}=0.58$ .

Figure 3-3 shows the comparison between the best LSR model (i.e., combined LSR for both datasets, red triangles) and the best ML technique (i.e., SVM for both datasets, blue squares). As expected, we observe for both datasets that the model prediction improves with the time window length (i.e., predictions and observations get closer to the 1:1 reference line; black line), especially for higher Dr values.

### 3. Earthquake Early Warning System for Structural Drift Prediction using Machine Learning and Linear Regressors

Our results highlight also that the SVM technique provides slightly better predictions than LSR models for both ANX and SRC datasets. Indeed, the variability of prediction for SVM is smaller than that from the linear regression models. This effect is even more evident looking at low and high  $Dr$  values (Figure 3-3), for which the linear regression models lead to higher variability in the prediction (i.e., especially for SRC buildings, panels d-f).

Such underestimation increases with drift amplitude, which is clearly function also of the events magnitude. For this reason, we hypothesize that the drift underestimation is due to two main effects: 1, for larger magnitude earthquakes (i.e.,  $M_w > 7.5$ ) the moment rate function is longer than 3 seconds, leading the maximum time-window (3s) to saturate, which in turns makes it difficult to predict  $Dr$ ; 2, differently from most of the datasets, the waveforms of large magnitude events are recorded at very large hypocentral distances and can be dominated by high amplitude surface waves. The dominance of surface waves in such signals can pose a problem to our analyses, because our dataset is mostly dominated by moderate to large magnitude events (the 90% of the Japanese data is between  $M_w$  3.6 and 7.0) and the larger ground motion is related to the S-waves. Therefore, models calibrated for estimating the drift associated to S-waves are not efficient in predicting  $Dr$  associated to very large magnitude earthquakes at large hypocentral distances generating high amplitude surface waves.

The analysis on the ANX and SRC datasets suggest us that it is possible to predict in real-time  $Dr$  using P-wave parameters. The best predictions are obtained using the 3s-time-windows and using ML models (i.e., the model  $SVM_{3s}$ ).

### 3. Earthquake Early Warning System for Structural Drift Prediction using Machine Learning and Linear Regressors

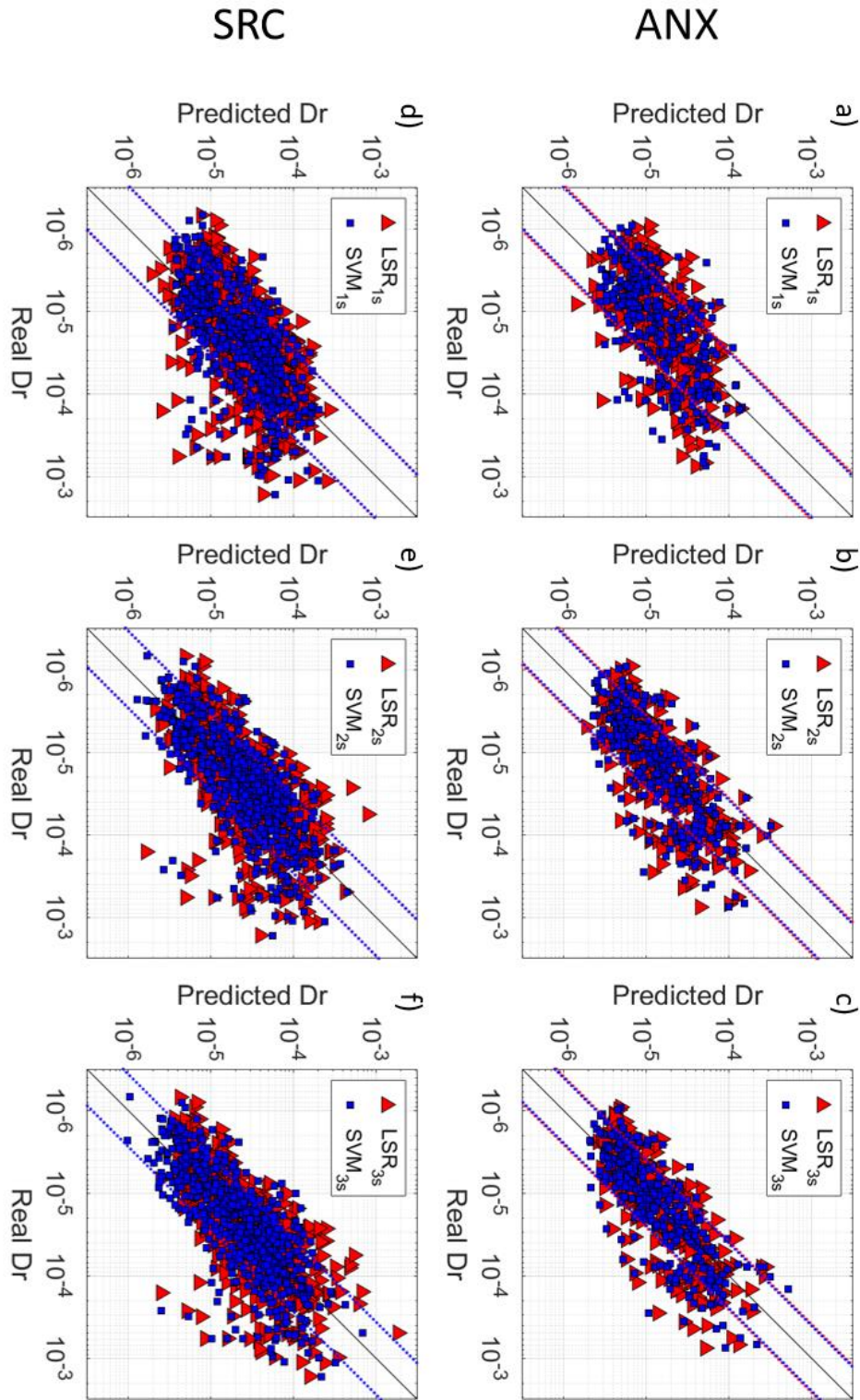


Figure 3-3: Predicted Dr versus Real Dr for three different windows for ANX dataset (a-c) and for SRC dataset (d-f). Red triangles refer to the prediction made least square regression using combined LSR for both datasets measured at the reference window. Blue squares refer to the predictions of the SVM regressor at the reference window. The black line Real Dr=Predicted Dr reference line. The dotted lines represent  $\pm\sigma_{train}$  confidence level for LSR (red) and ML (blue) models.

### 3. Earthquake Early Warning System for Structural Drift Prediction using Machine Learning and Linear Regressors

Table 3-4: ML regression results, ANX dataset

ML <sub>w</sub>	$\sigma_{\text{train}}$	$\sigma_{\text{test}}$	$R^2_{\text{train}}$	$R^2_{\text{test}}$
RF <sub>1s</sub>	0.49	0.49	0.38	0.38
RF <sub>2s</sub>	0.44	0.42	0.51	0.53
RF <sub>3s</sub>	0.42	0.39	0.55	0.60
GB <sub>1s</sub>	0.50	0.49	0.36	0.38
GB <sub>2s</sub>	0.44	0.42	0.50	0.53
GB <sub>3s</sub>	0.43	0.39	0.53	0.59
SVM <sub>1s</sub>	0.49	0.47	0.39	0.43
SVM <sub>2s</sub>	0.42	0.40	0.54	0.57
SVM <sub>3s</sub>	0.40	<b>0.37</b>	0.58	<b>0.64</b>
KNN <sub>1s</sub>	0.49	0.50	0.37	0.35
KNN <sub>2s</sub>	0.44	0.42	0.51	0.54
KNN <sub>3s</sub>	0.42	0.39	0.56	0.59

Table 3-5: ML regression results, SRC dataset

ML <sub>w</sub>	$\sigma_{\text{train}}$	$\sigma_{\text{test}}$	$R^2_{\text{train}}$	$R^2_{\text{test}}$
RF <sub>1s</sub>	0.50	0.51	0.41	0.40
RF <sub>2s</sub>	0.46	0.46	0.50	0.51
RF <sub>3s</sub>	0.44	0.43	0.54	0.57
GB <sub>1s</sub>	0.50	0.51	0.40	0.40
GB <sub>2s</sub>	0.46	0.46	0.50	0.51
GB <sub>3s</sub>	0.44	0.44	0.54	0.55
SVM <sub>1s</sub>	0.49	0.50	0.42	0.41
SVM <sub>2s</sub>	0.45	0.45	0.52	0.53
SVM <sub>3s</sub>	0.42	<b>0.42</b>	0.57	<b>0.58</b>
KNN <sub>1s</sub>	0.50	0.51	0.39	0.39
KNN <sub>2s</sub>	0.46	0.47	0.49	0.49
KNN <sub>3s</sub>	0.43	0.44	0.55	0.55

### 3. Earthquake Early Warning System for Structural Drift Prediction using Machine Learning and Linear Regressors

#### 3.4 Japanese dataset analysis

In this section, we discuss the development and testing of prediction models considering the entire Japanese dataset.

##### 3.4.1 Least Square Regression Laws

Table 3-6 reports the results for LSR models calibrated on the Japanese dataset. In this case, we observe that the performances on training and testing set are very similar. Again, we notice an overall worsening of both the scores with respect to the ANX (Table 3-2) and SRC buildings (Table 3-3). Clearly, this outcome was expected, given that the Japanese dataset includes more variability than the other two datasets.

In this case, all the P-wave proxies (XPs) show basically the same results in terms of  $\sigma_{\text{test}}$  and  $R^2_{\text{test}}$  for the same windows. On the other hand, combined LSR models perform slightly better at 2s and 3s. We have the best results for LSR<sub>3s</sub>, as in the other cases,  $\sigma_{\text{test}}=0.48$  and  $R^2_{\text{test}}=0.41$ . Despite such low fitting score can generate skepticism about these LSR models utility, in the following section 3.4.3, we will show that by a residual analysis we can identify some of the component generating the large variability of predictions.

Table 3-6: Least square regression results, Japanese dataset

$XP_w$	<b>a</b>	<b>b</b>	$\sigma_{\text{train}}$	$\sigma_{\text{test}}$	$R^2_{\text{train}}$	$R^2_{\text{test}}$
$ID^2_{1s}$	-3,52	0,18	0,54	0,54	0,23	0,24
$ID^2_{2s}$	-3,46	0,21	0,52	0,52	0,29	0,30
$ID^2_{3s}$	-3,41	0,23	0,50	0,50	0,33	0,34
$IV^2_{1s}$	-3,75	0,17	0,54	0,54	0,22	0,24
$IV^2_{2s}$	-3,72	0,20	0,52	0,52	0,28	0,29
$IV^2_{3s}$	-3,71	0,22	0,51	0,50	0,32	0,34
$Pd_{1s}$	-3,48	0,37	0,54	0,54	0,23	0,24
$Pd_{2s}$	-3,38	0,43	0,52	0,52	0,30	0,29
$Pd_{3s}$	-3,32	0,48	0,50	0,50	0,35	0,34
$LSR_{1s}$			0,54	0,54	0,23	0,25
$LSR_{2s}$			0,50	0,50	0,35	0,34
$LSR_{3s}$			0,47	<b>0,48</b>	0,41	<b>0,41</b>

### 3. Earthquake Early Warning System for Structural Drift Prediction using Machine Learning and Linear Regressors

#### 3.4.2 Machine Learning Regression

Table 3-7 is the analogue of Table 3-4 and Table 3-5 for the Japanese dataset. As for the previous cases, MLs perform better than LSR for the same time window. In this case also, the best model is SVM<sub>3s</sub>, with  $\sigma_{\text{test}}=0.45$  and  $R^2_{\text{test}}=0.47$ . In Figure 3-4, we compare the predictions of LSR<sub>3s</sub> for one of the best LSR models (Table 3-6) with that of SVM<sub>3s</sub>. This comparison clearly shows us that the cloud of SVM<sub>3s</sub> estimates is thinner than that for LSR. Despite that, both models seem to saturate above Dr equal to  $4 \cdot 10^{-4}$ .

The performances of the calibrated models seem to be worse than those proposed by onsite EEW studies (among others, (Olivieri et al., 2008; Wu and Kanamori, 2008; Zollo et al., 2010; Brondi et al., 2015; Caruso et al., 2017)). A direct comparison among different approaches is however unfair. Indeed, despite the appearance, we must consider that generally onsite EEW studies focus on the prediction of ground motion parameters (e.g., peak ground acceleration, PGA) using data collected in free-field. On the contrary, in this study, we predict an engineering demand parameter (Dr) using data from in-building sensors. Our approach is certainly challenging because building responses inflate the variability of our predictions. Furthermore, we must also consider that recent studies (Astorga et al., 2020; Ghimire et al., 2021) explored the prediction of drift from PGA measures using the same dataset considered here and found a prediction variability similar to that of our models. Moreover, other studies, such as Tubaldi et al., 2021, pointed out that event-to-event variability contributes significantly to the uncertainties in the damage prediction, even for single structure models.

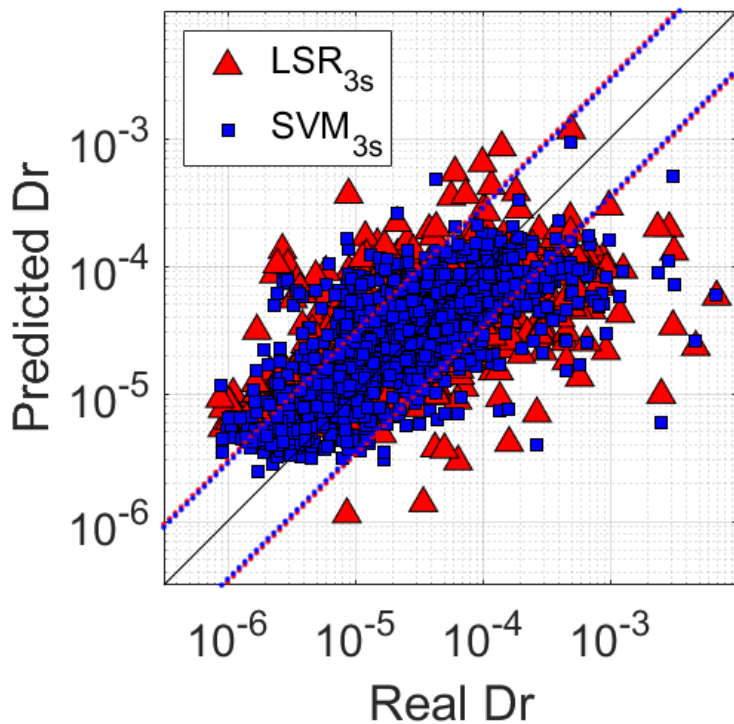


Figure 3-4: Predicted Dr versus Real Dr of the test set for the Japanese dataset for 3s windows. Red triangles refer to the predictions with LSR<sub>3s</sub>. Blue squares refer to the predictions of the SVM<sub>3s</sub> model. The black line Real Dr=Predicted Dr reference line. The dotted lines represent  $\pm\sigma_{\text{train}}$  confidence level for LSR (red) and ML (blue) models.

### 3. Earthquake Early Warning System for Structural Drift Prediction using Machine Learning and Linear Regressors

Table 3-7: ML regression results, Japanese dataset

ML <sub>w</sub>	$\sigma_{\text{train}}$	$\sigma_{\text{test}}$	$R^2_{\text{train}}$	$R^2_{\text{test}}$
RF <sub>1s</sub>	0,52	0,52	0,28	0,29
RF <sub>2s</sub>	0,48	0,48	0,39	0,39
RF <sub>3s</sub>	0,46	0,46	0,43	0,46
GB <sub>1s</sub>	0,52	0,52	0,28	0,29
GB <sub>2s</sub>	0,49	0,49	0,38	0,38
GB <sub>3s</sub>	0,47	0,46	0,43	0,44
SVM <sub>1s</sub>	0,52	0,52	0,27	0,31
SVM <sub>2s</sub>	0,49	0,48	0,38	0,40
SVM <sub>3s</sub>	0,46	<b>0,45</b>	0,43	<b>0,47</b>
KNN <sub>1s</sub>	0,53	0,53	0,26	0,28
KNN <sub>2s</sub>	0,48	0,48	0,38	0,40
KNN <sub>3s</sub>	0,46	0,45	0,43	0,46

#### 3.4.3 Residual analysis

As we saw in Table 3-6 and Table 3-7, the fitting scores for all the methods are generally rather low. This can be due to numerous factors. One reason can be the lack of information of the EEW input features that, as said, are extracted from P waves, while the final building drift is related to S and surface waves. Anyway, this effect is unavoidable in onsite EEW and also difficult to quantify. Instead, we can try to assess which other factors influence the variability of our methods. So, to better understand the strengths and weaknesses of the calibrated models, we performed a residual analysis (Al Atik et al., 2010). To this purpose, we disaggregate the residuals (predicted minus real Dr values) by site and event characteristics. In Figure 3-5, we compare the testing set residuals for the LSR model considering Pd<sub>3s</sub> (red error-bars) and the equivalent for SVM<sub>3s</sub> (blue error-bars). For each group, we show the mean and the standard deviation of residuals. In all sub-plots of Figure 3-5, we also show the  $\pm\sigma_{\text{train}}$  references for both methods (i.e., 0.50 for Pd<sub>3s</sub> represented as red lines, and 0.46 for SVM<sub>3s</sub> represented as blue lines).

Figure 3-5a presents the residuals grouped by buildings, which are ordered by the mean of the residuals for the two methods. We colored the labels of the buildings by type of construction (pink for RC, light green for SRC, blue for ST) and the edge of the label by the height (brown for low-rise, green for high-rise). At first glance, we observe that the two methods show similar performance in terms of mean of the residuals for all the buildings. Looking at residual variability, however, we observe that in most of the cases ML performs better than LSR, especially for two buildings “YKH1” and “SKS”.

A more detailed examination to residuals variation for different buildings suggests conclusions similar to those of Al Atik et al. (2010) for ground motion prediction equations (GMPEs). These authors, indeed, explored the epistemic uncertainty by splitting it into source, path, and site contributions. If we

### 3. Earthquake Early Warning System for Structural Drift Prediction using Machine Learning and Linear Regressors

consider one or many of these factors in our model, we are relaxing the ergodic assumption which states that the variability of the dataset is completely aleatory. The variability of the residuals in Figure 3-5a is the result of the site-effect, which in our particular case is a term used to describe the response of the soil-structure system that can lead to a very complex behaviour. Nevertheless, the full investigation and explanation of the causes of these site conditions is beyond the aim of this paper. In our opinion, the significant variation in residuals shown in Figure 3-5a is not surprising, being in agreement with other studies (Spallarossa et al., 2019; Iaccarino et al., 2020); which have recently discussed how to reduce the prediction variability considering site-effect terms in EEW model using the mixed-effect regression approach (Pinheiro and Bates, 2000).

As second step, we analyze the residuals grouping them for building characteristics and height (see Table 3-1 and Figure 3-5b). Our results show that the mean of residuals for all building groups are close to zero, except for low-rise ST buildings. This latter class, however, includes only the building KWS, that also in the previous analysis showed a peculiar response (Figure 3-5a). Being the average of residuals consistent with zero, the predictions seem independent from the type of construction and the height of the buildings.

In Figure 3-5c and d, we show the residuals versus the event parameters magnitude and distance. It is worth noting that these are not 'sufficiency analysis' as intended by Luco (2002). Indeed, in the sufficiency analysis a cinematic parameter is defined as sufficient for predicting an engineering demand parameter (e.g., Dr) if the predictions are independent from magnitude and distance. To confirm this property, a probabilistic analysis would be needed, but that is beyond the aim of this study.

Figure 3-5c shows the error bars, the residual mean and standard deviation in bins of 1 unit centered on the magnitude value. From these results, we can clearly see that the magnitude has a great effect on the prediction. In particular, we see that the predictions are good between magnitude 4 and 7, while we overestimate Dr at lower magnitudes and underestimate Dr at higher magnitudes. The overestimation at magnitudes lower than 3.5 is probably due to the fact that the predominant frequencies of such events are too high to stimulate an effective response of the building (i.e., we consider a frequencies range between 0.5 Hz and 2 Hz). On the other hand, as previously discussed, the underestimation for magnitude greater than 7.5 is likely due to: i) the window length of 3s, which is too small compared to the rupture duration and lead to saturation problems of the prediction; ii) the measured Dr can be affected by the presence of surface waves associated to large magnitude events. Measures of Dr from signals dominated by surface waves, indeed, might add non-linear terms to the equation between our XP and Dr itself. The underestimation at high magnitudes can be also caused by the lower number of recordings in the dataset with respect to those for the smaller magnitudes, i.e. a typical problem for all the EEWS (Hoshiba et al., 2011; Chung et al., 2020). Moreover, another possible bias that big events can introduce are the non-linear responses of site and buildings, especially during long sequence of earthquakes (Guéguen et al., 2016; Astorga et al., 2018). The saturation of Dr predictions for earthquakes with  $M > 7.5$  is certainly a big issue for the application of the calibrated models in operational EEW systems in areas where very large earthquakes are expected, and further studies are necessary to deal with it. Nevertheless, our results indicate that the calibrated models can be useful in countries characterized by moderate to large seismic hazard (e.g., Italy, Greece, Turkey; where the seismic risk is high due to high vulnerability and exposure). A more in-depth analysis of the performances for EEW systems using the models calibrated is beyond the aim of this study, because it would require target dependent economic cost-benefit analyses (Strauss and Allen, 2016; Minson et al., 2019).

Interestingly, SVM<sub>3s</sub> seems providing better results than LSR for both for lowest and highest magnitude events. In our opinion, this result suggests a higher performance of non-linear models.

Finally, Figure 3-5d shows the residuals grouped by the distance, using 6 bins evenly spaced in logarithmic scale from  $10^{0.5}$  to  $10^3$  km. The mean of residuals and the associated standard deviation are

### 3. Earthquake Early Warning System for Structural Drift Prediction using Machine Learning and Linear Regressors

plotted at the center of each corresponding bin. We observe that all the residuals are close to zero. Nevertheless, we observe a small overestimation of the prediction at distances lower than 20 km. This effect is partially connected to the overestimation seen for low magnitudes (Figure 3-5c), because in this range of distances the magnitude is limited between 2.6 and 5.2. In this case too, the machine learning seems able to learn how to solve the bias.

The results of the residual analysis suggest: i) SVM<sub>3s</sub> is confirmed as the best model; ii) decomposing the residuals with respect to buildings, construction type, magnitude, and distance, we found a broad variation of the mean residuals with the buildings typology. This result suggests that site-correction terms should be included in future EEW application to buildings. iii) The residuals are correlated to the magnitude, while they seem be much less dependent from the distance.

### 3. Earthquake Early Warning System for Structural Drift Prediction using Machine Learning and Linear Regressors

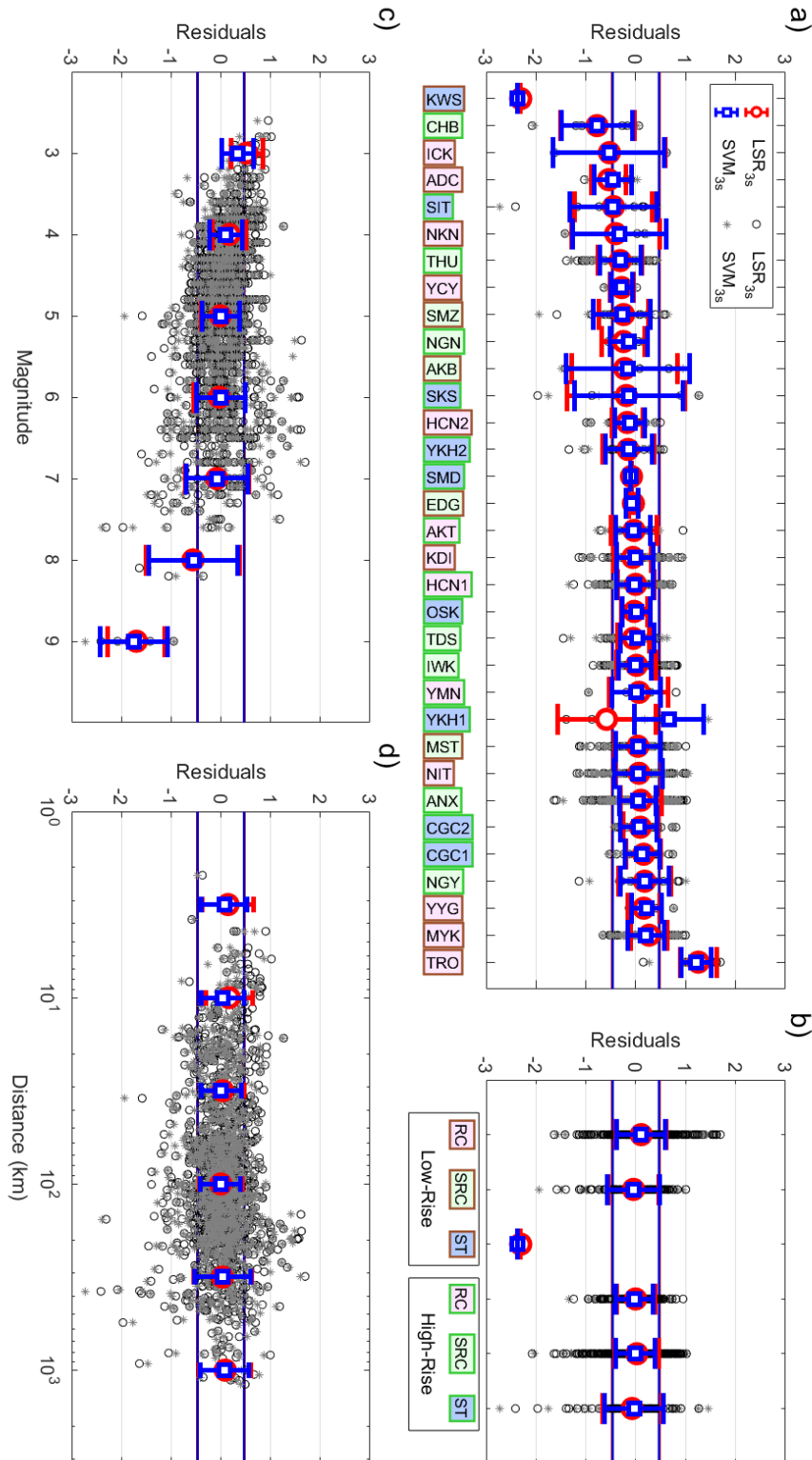


Figure 3-5: Decomposition of the residuals of  $D_r$  prediction for Japanese test set. The residuals are computed as real  $D_r$  - predicted  $D_r$ , so positive values mean overestimation, and negative residuals mean underestimation. In each panel we show the residuals for two different models: LSR  $Pd_{3s}$  with circles representing the single prediction and red errorbars representing the mean prediction of the group; SVM  $_{3s}$  with stars for the single prediction and blue errorbars for the group mean. Red and blue lines represent the  $\pm\sigma_{train}$  for LSR  $Pd_{3s}$  and SVM  $_{3s}$ , respectively. The labels in panels a) and b) are colored by construction type and height: pink for RC; light green for SRC; blue for ST; brown edges for low-rise; green edges for high-rise. In panel a) we decompose the residuals by buildings. In b) we group them by building type of construction and height. In panel c) we use the magnitude to decompose residuals, the groups are evenly spaced and the errorbars are placed in the center of the bin. In panel d) the residuals are grouped by distance in km, the groups are evenly spaced and the errorbars are placed in the center of the bin.

### 3. Earthquake Early Warning System for Structural Drift Prediction using Machine Learning and Linear Regressors

#### 3.5 US dataset application

In the last part of this work, we apply the models calibrated using the Japanese dataset to the U.S. dataset. Our aim is to verify if the usual ergodic assumption often used in EEW application is valid or not, and eventually to look for strategies that could allow to successfully export the models from one region to another.

##### 3.5.1 Least Square Regression Laws

Table 3-8 reports the results for the linear regression performed on the complete dataset. The most noticeable aspect here is the  $R^2_{\text{test}}$  column that presents all negative value. This is due to a quite important bias in the prediction of  $Dr$  for U.S. building. In Figure 3-6, we show the mean residual for U.S. dataset, which are plotted as orange error bars with the length equal to  $\sigma_{\text{test}}/\sigma_{\text{train}}$ . Since the residuals are computed as differences between predicted and observed  $Dr$ , the linear regression of the Japanese dataset underestimates the  $Dr$  of the U.S. buildings of about  $1\sigma$ . We find a similar bias also for ML techniques. These observations confirm that exporting EEW models among different regions, independently from the algorithm used for their calibration, is not a straightforward operation.

In the next section, we analyze the causes of this bias, and we propose a solution.

Table 3-8: Least square regression results, complete dataset

$XP_w$	<b>a</b>	<b>b</b>	$\sigma_{\text{train}}$	$\sigma_{\text{test}}$	$R^2_{\text{train}}$	$R^2_{\text{test}}$
$ID^2_{1s}$	-3,52	0,18	0,54	0,48	0,23	-0,45
$ID^2_{2s}$	-3,46	0,21	0,52	0,46	0,29	-0,37
$ID^2_{3s}$	-3,42	0,23	0,50	0,46	0,34	-0,25
$IV^2_{1s}$	-3,75	0,17	0,54	0,47	0,23	-0,48
$IV^2_{2s}$	-3,73	0,20	0,52	0,45	0,28	-0,39
$IV^2_{3s}$	-3,72	0,22	0,51	0,46	0,33	-0,25
$Pd_{1s}$	-3,49	0,37	0,54	0,48	0,24	-0,44
$Pd_{2s}$	-3,39	0,43	0,52	0,46	0,30	-0,36
$Pd_{3s}$	-3,33	0,47	0,50	0,46	0,35	-0,25
$LSR_{1s}$			0,54	0,47	0,24	-0,44
$LSR_{2s}$			0,50	0,46	0,35	-0,35
$LSR_{3s}$			0,48	0,54	0,41	-0,32

### 3. Earthquake Early Warning System for Structural Drift Prediction using Machine Learning and Linear Regressors

#### 3.5.2 Bias analysis

We present here the results of the residual analysis carried out on the U.S. buildings predictions. Figure 3-6 shows the results as orange error-bars for LSR with  $IV^2_{2s}$ . We selected this particular model because, as we will show also later, after the application of a correction term it becomes the best predictive model for drift on U.S. buildings.

To correctly evaluate the effectiveness of the method, we divided the U.S. dataset in two subsets (60% and 40%): whereas the first subset is used to compute the correction terms and the second one is used to test the models. The residuals for the corrected model are plotted as green error-bars for the U.S. train set and as light blue for the U.S. test set. We report as reference level the  $\pm\sigma_{\text{train}}$  as black lines (see also Table 3-8).

First, we consider only the uncorrected residuals (i.e., orange error-bars). In Figure 3-6a, we plot only the results for U.S. buildings with at least 3 records, grouping the remaining ones as 'Others'. The buildings are ordered for increasing mean value of residuals. We observe a general smaller variability of the residuals with the buildings than for Japanese buildings (Figure 3-5a), but at the same time we notice that the majority of the buildings have predictions underestimated and non-zero residuals. These results indicate that there is a bias in the global trend of predictions with respect to the buildings.

Looking at Figure 3-6b, we can note that, while a small bias is still present for high-rise buildings, the majority of the bias is due to low-rise buildings. However, this difference between building classes is not significant since all the bars are consistent with each other.

In Figure 3-6c, as for Figure 3-5c, we notice a strong correlation between residuals and magnitude. We can see, indeed, that the predictions worsen with the increasing of the magnitude.

Finally, in Figure 3-6d, the residuals for U.S. dataset seem to be not significantly affected by the distance. Indeed, the residuals remain equally underestimated but in the second range that goes from about 6 km to 18 km. The anomaly in this range of distances is probably connected to data distribution. In fact, here we find events with magnitude between 3.5-4.5 and we can relate this result with what we observe for low magnitude in Figure 3-6c.

### 3. Earthquake Early Warning System for Structural Drift Prediction using Machine Learning and Linear Regressors

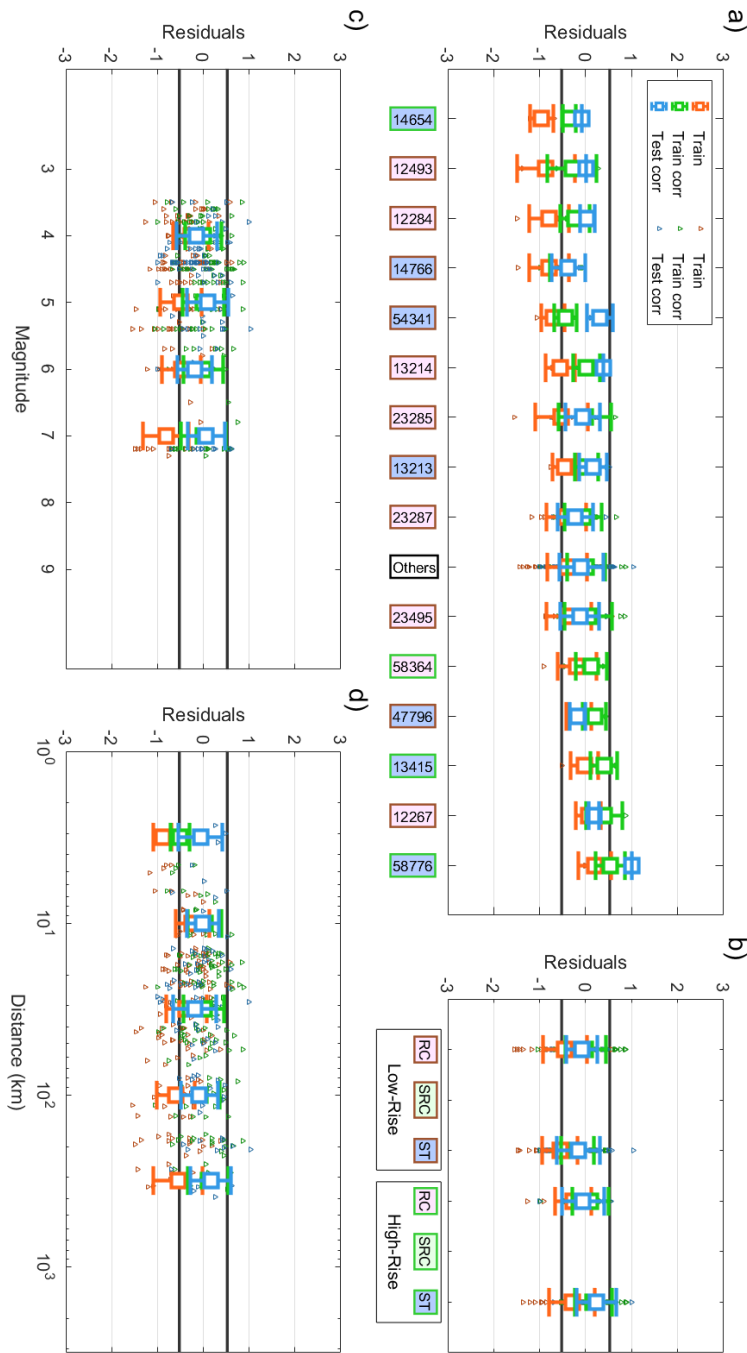


Figure 3-6: Decomposition of the residuals of  $D_r$  prediction for US dataset using Japanese model. The residuals are computed as real  $D_r$  - predicted  $D_r$ , so positive values mean overestimation, and negative residuals mean underestimation. In each panel we show the residuals for LSR  $IV^2_{2s}$  model in three cases: for the training set without corrections, with orange triangles representing the single prediction and orange errorbars representing the mean prediction of the group; for the training set and with magnitude dependent correction with green triangles for the single prediction and green errorbars for the group mean; for the testing set with magnitude dependent correction with light blue triangles for the single prediction and light blue errorbars for the group mean. Black lines represent the  $\pm\sigma_{train}$  for LSR  $IV^2_{2s}$ . The labels in panels a) and b) are colored by construction type and height: pink for RC; light green for SRC; blue for ST; brown edges for low-rise; green edges for high-rise. The "Others" label is white. In panel a) we decompose the residuals by buildings. In b) we group them by building type of construction and height. In panel c) we use the magnitude to decompose residuals, the groups are evenly spaced and the errorbars are placed in the center of the bin. In panel d) the residuals are grouped by distance in km, the groups are evenly spaced and the errorbars are placed in the center of the bin.

### 3. Earthquake Early Warning System for Structural Drift Prediction using Machine Learning and Linear Regressors

#### 3.5.3 Bias correction

In this section, we propose a methodology to account for the bias observed from the residual analysis applied to U.S. buildings drift predictions. To this aim, we borrowed the strategy adopted in seismic hazard studies where the decomposition of the variability in the ground motion predictions can be used to improve the estimates (Al Atik et al., 2010).

We consider, as correction terms, the residuals for magnitude classes,  $\Delta Dr_M$ , computed for the U.S. training set (Figure 3-5c, orange error-bars). Estimating the magnitude in EEW applications is a well-established task, with a large number of operational, reliable algorithms and a wide literature, at least for earthquakes with magnitude smaller than  $M_w$  7.5. For example, Mousavi and Beroza (2020) showed that by ML approaches reliable estimation of earthquake magnitude from raw waveforms recorded at single stations can be obtained (standard deviation  $\sim 0.2$ ). We thus foresee similar achievements in EEW in the next future. Here, we considered suitable to set corrections for our models be magnitude dependent. Therefore, for the sake of simplicity, we assume that magnitude estimates are provided in real-time by other EEW systems and are available as input for our Dr predictions.

It is worth noting that for very large earthquakes ( $M_w > 7.5$ ) the 3-second P-wave windows considered in our study do not include enough information to estimate the magnitude (Hoshiya et al., 2011; Chung et al., 2020). Therefore, the proposed magnitude dependent correction is considered valid only for events smaller than  $M_w$  7.5.

The  $\Delta Dr_M$  terms computed using the EEW magnitude estimates as input can thus be subtracted to the predicted Dr in order to set at zero the mean residual in each magnitude range:  $\log_{10} Dr^{corr} = \log_{10} Dr - \Delta Dr_M$ .

Table 3-9 shows the  $R^2$  scores for all the models and time windows after that we have applied the  $\Delta Dr_M$  corrections on the testing dataset. We observe that, in this case, the 2s predicting models performs better than the 3s ones. Moreover, LSR<sub>3s</sub> has still negative  $R^2$  and so the correction in this case is ineffective. It is difficult to understand if this effect is due to the correction or to the window that can include more S-wave content at 3s for these events. The most interesting aspect is that the LSR methods with single feature perform now better than combined LSR, and ML models. This result is probably connected to the characteristics of ML techniques. In fact, ML algorithms are typically less able than LSR ones to extrapolate the predictions outside the features' domain of the training set. In addition, some of them, like RF or KNN, cannot predict target values outside the target domain for the training set by construction. Probably, combined LSR models also suffer of the same problems of ML techniques because of their complexity.

The best model after the  $\Delta Dr_M$  correction is the LSR with  $IV_{2s}^2$ . As anticipated, this is the reason why we plotted the result for this model in Figure 3-6.

By construction, after the magnitude correction, the error-bars (green) have all zero-mean, but we can see that also the residuals for the test set are consistent with zero (Figure 3-6c). Figure 3-6a now shows that residuals for the training set have the same number of buildings with underestimated and overestimated predictions. Moreover, the residuals for the testing set are consistent the training one, but for three buildings (i.e., "14654", "54341", and "58776"). This variability well agrees with Figure 3-5a, and as discussed, it depends on site and buildings effects. In Figure 3-6b, for both training and testing set, we find again the difference in mean residuals for low-rise and high-rise buildings, but this effect is present especially for ST buildings. Moreover, the drift for high-rise ST buildings is now meanly overestimated. In the end, in Figure 3-6d, we see that, despite some oscillation, the residuals have not any more dependence with distance, as seen for Japanese buildings in Figure 3-5d.

### 3. Earthquake Early Warning System for Structural Drift Prediction using Machine Learning and Linear Regressors

As conclusion of this analysis, we can state that when the models retrieved considering the Japanese dataset are applied to the U.S. dataset, the Dr predictions present a severe bias. However, by including a magnitude dependent correction term seems a relatively simple and practice solution to solve the problem. We have also found that the LSR models, after the correction, perform better than ML models. The best model, in this case, is the LSR with  $IV_{2s}^2$ .

Table 3-9:  $R^2$  scores for US dataset corrected drift prediction.

Model	1s	2s	3s
LSR-ID <sup>2</sup>	0,21	0,26	0,25
LSR-IV <sup>2</sup>	0,27	<b>0,30</b>	0,27
LSR-Pd	0,20	0,24	0,20
Combined LSR	0,22	0,21	-0.03
RF	0,21	0,19	0,09
GB	0,23	0,21	0,08
SVM	0,16	0,21	0,18
KNN	0,10	0,15	0,16

### 3.6 Conclusions

In this work, we tested the performance of several predicting models for building drift using three different EEW P-wave parameters computed considering three time-window lengths, for a total of nine features. We used a dataset of almost 6,000 waveforms from in-building sensors recorded in Japan and California. We compared linear least square and non-linear machine learning regressions for a total of 21 different models. We set up four different case-studies to understand how the data variability affects the predictions.

Our results can be summarized as follow:

Analyzing a single building (“ANX”) with a very long history of records, then all the data for the steel-reinforced concrete buildings (which contains “ANX”), and finally the entire Japanese dataset, we show that the training and the testing set have the same kind of variability and ML models perform always better than least square regression. In particular, ML models result more efficient in dealing with the non-linearity of the problem, likely because they are able to get more information from features combining them together. Moreover, the results prove that the increasing of the time window always improves the predictions. The results showed us that it is possible to retrieve building specific EEW models for Dr prediction. This result is probably also related to the large size and good quality of the ANX dataset.

The results for the steel-reinforced concrete buildings dataset show that we can retrieve reliable models also grouping data from similar buildings. Having a lot of data from more buildings can help to overcome the problems of a few data from a single building, but at the price of a decrease in the accuracy of the predictions. Indeed, we observed a further reduction in accuracy when we used the

### 3. Earthquake Early Warning System for Structural Drift Prediction using Machine Learning and Linear Regressors

entire Japanese dataset. So, increasing in variability of the dataset lead to models prone to precision of the predictions problems that should be considered accurately.

To better understand this issue, we used models retrieved on the entire dataset to explore the residuals correlation with buildings, types of construction, magnitude, and distance. This analysis has shown that the prediction residuals are strongly dependent from buildings and magnitude. In particular, we have found that some buildings are not well described by the models. This effect can be considered as a site-effects, which is in this application due to effects of many combined factors (e.g., 1D-to-3D soil amplification, soil-structure interaction, building resonance). Instead, looking at the magnitude, we observed a drift overestimation at lower magnitude ( $M < 4$ ) and an underestimation at higher magnitude ( $M > 7$ ). Such latter effect is the more worrying for EEW applications and it is likely due to both the lack of data in this range of larger magnitude, and to the time window length of 3s that does not contain enough information about the source size.

We have applied the Japanese models to predict the Dr in U.S. buildings, and we have found that in this case the predictions are biased leading Dr being underestimated. An important warning from our study is that EEW models for drift prediction are not directly exportable. This bias may be mainly due to geological and seismological differences between Japan and California. An analysis of residuals decomposed for different factors has shown a strong dependency from site-effects and magnitude.

We proposed a method to correct the prediction bias resulting from exporting EEW model to other regions from those of calibration. We showed that by applying a magnitude dependent correction terms to the predictions the biases can be removed. Hence, we showed that by the suggested method, the predictions become reliable again.

Finally, an interesting result is that, in the particular case of exporting models to another region, the linear models perform better than machine learning. This result, despite is not very surprising since it is well-known that the non-linear models are less able to extrapolate predictions outside the features' domain of the training set, can be a useful warning for the EEWS community approaching to ML regressors.

Future studies will explore the application of the proposed methodology considering dataset from different regions. For those areas characterized by very large earthquakes, as Japan or Chile, we will explore the use of larger P-wave time-windows. We believe that this study can stimulate applications of non-linear ML models in the onsite EEW framework. Indeed, future studies can use similar approaches for the computation of ground motion parameters (i.e., PGV, PGA, etc.), as well as of other engineering demand parameters.

A final key point coming out from our analysis is the importance to better understand how the inner variability of a dataset affects the predictions. Our results suggest in fact that by increasing the datasets, we can improve the characterization of the prediction variability ascribed to site effects (e.g., soil-conditions, building response, soil to structure interaction, etc.).

## 4. Forecasting the Preparatory Phase of Induced Earthquakes by Recurrent Neural Network

Antonio Giovanni Iaccarino<sup>1</sup> and Matteo Picozzi<sup>1</sup>

<sup>1</sup> Università degli studi di Napoli, Federico II, Dipartimento di Fisica "Ettore Pancini", Napoli, Italia

Published in: Forecasting (Picozzi and Iaccarino, 2021)

doi: 10.3390/forecast3010002.

## 4. Forecasting the Preparatory Phase of Induced Earthquakes by Recurrent Neural Network

### 4.1. Introduction

The physics of earthquake initiation is a challenging research field with severe implications for modern society in terms of earthquake forecasting and seismic risk mitigation.

Pioneering studies (Rikitake, 1975; Dieterich, 1978; Jones and Molnar, 1979; Jones, 1985; Abercrombie and Mori, 1996; Dodge et al., 1996; Lapusta and Rice, 2003) have shown that large magnitude earthquakes can be anticipated by foreshocks and slip instabilities. However, the non-systematic foreshock appearance and the lack of systematic precursory patterns led the background physical processes generating foreshocks and the preparatory phase being not fully understood and matter of debate (Kanamori, 1981; Mignan, 2012).

Two main contrasting models have been proposed concerning foreshocks generations. According to some authors (Das and Scholz, 1981; Ohnaka, 1992; Mignan, 2012), foreshocks are related to a tectonic loading process associated to aseismic slip, which represents a deviation from the normal behavior of seismicity (Mignan, 2014). This model would support the existence of a preparatory phase for large earthquakes, leaving us with the hope that in future earthquakes will be predictable.

By contrast, for other authors (Helmstetter and Sornette, 2003; Felzer et al., 2004) foreshocks result from a triggering process that is part of the normal behavior of seismicity (i.e., following the concept of Self-Organized Criticality), for which events can cascade into a larger one without any clear, yet, background driving process. The key practical aspect of this model is that the probability of a large event in a short period (e.g., one week) following to the occurrence of foreshocks is very low, and therefore of limited use (Mignan, 2014).

Over the last decade, significant advances have been obtained in this research field thanks to the availability of high-resolution seismic catalogs, which resulted from efforts done by the seismological community in increasing the number of dense seismic networks deployed nearby active faults and in the development of advanced event detection techniques. A recent study (Trugman and Ross, 2019) has shown, indeed, that thanks to enriched catalogues foreshock activity in California is much more common than previously understood, with foreshocks that have been found in 72% of cases for a sample of 46 mainshocks.

However, it must keep in mind that 'foreshocks' is a label assigned to earthquakes retrospectively. Instead of trying to single out if an event is a foreshock or not, a promising route seems observing the collective spatial and temporal behavior of small magnitude earthquakes for unveiling if seismic or aseismic preparatory processes are underway.

As result of the scientific developments in infrastructures and data-mining strategies, systematic patterns in seismicity preceding large earthquakes have started to emerge (Hauksson et al., 2011; Kato et al., 2012; Bouchon et al., 2013; Ruiz et al., 2017; Socquet et al., 2017; Ellsworth and Bulut, 2018; Malin et al., 2018; Piña-Valdés et al., 2018; Ross et al., 2019; Yoon et al., 2019), showing that micro and small magnitude events before large earthquake show temporal and spatial peculiar patterns in their evolution. These observations support the idea that, at least in some cases, the interpretative model for which foreshocks are related to a tectonic loading process associated to aseismic slip (Das and Scholz, 1981; Ohnaka, 1992; Mignan, 2012) is reliable.

A recent, systematic review on the initiation of large earthquakes (Kato and Ben-Zion, 2021) has highlighted that their generation is the result of complex, multiscale processes where the tectonic environment and external factors (e.g., natural and/or anthropogenic inputs that impact on the local stress-field) interact. The resultant integrated generation model (Kato and Ben-Zion, 2021) proposes a progressive localization of shear deformation around a rupture zone, which evolves into a final rapid loading (i.e., generating

#### 4. Forecasting the Preparatory Phase of Induced Earthquakes by Recurrent Neural Network

foreshocks) of a localized volume nearby the hypocenter of the major dynamic rupture. Such kind of process might be universal. Indeed, similar patterns of damage evolution across a fault zone have been found also studying the temporal and spatial distribution and characteristics of acoustic emissions during triaxial tests on rock samples (Dresen et al., 2020).

We outline the generation processes of large earthquakes model in Figure 4-1. Here, we summarize the spatio-temporal evolution of small events before and after a large earthquake together with the expected seismic parameters trend (i.e., see below for their explanation), which have been identified as good indicators for the damage evolution (see Dresen et al., 2020; Kato and Ben-Zion, 2021; and the references therein).

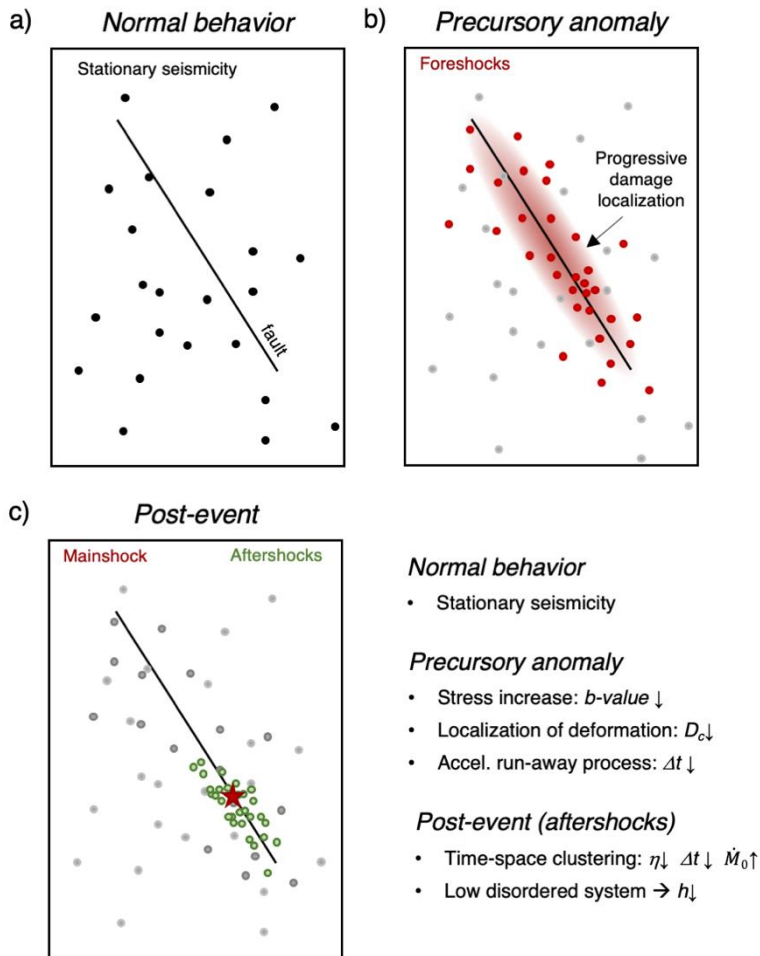


Figure 4-1: Schematic illustration of the processes anticipating and following a large earthquake. (a) Normal behavior phase, during which the seismicity shows a spatio-temporal stationary nature. (b) Precursory anomaly phase, during which the localization of deformation proposed by Kato and Ben-Zion (2021), occurs. Seismicity can show  $b$ -value, fractal dimension ( $D_c$ ), and seismic-rate ( $\Delta t$ ) decrease. (c) Post-event phase, during which the seismicity is characterized by time-space clustering (i.e.,  $\Delta t$  and generalized-distance,  $\eta$ , decrease, while moment-rate,  $\dot{M}_0$ , increase) and the system shows high order (Shannon entropy,  $h$ , decrease).

In view of these studies (Dresen et al., 2020; Kato and Ben-Zion, 2021), monitoring the spatio-temporal evolution of microseismicity could lead recognizing the preparatory phase of moderate to large earthquakes a reachable goal.

A meta-analysis of seismic sequences preceding large earthquakes (Mignan, 2014) has highlighted that when observed in nature, the preparatory phase is potentially identifiable if the detected seismic events are more than three orders of magnitude lower than the mainshock. This justifies why the preparatory phase is generally difficult to detect and observe for moderate size earthquake, unless enriched catalogues are available (Durand et al., 2020; Sánchez-Reyes et al., 2021).

#### 4. Forecasting the Preparatory Phase of Induced Earthquakes by Recurrent Neural Network

Recent works explored the use of machine learning (ML) to predict the time remaining before rupture in laboratory experiments (Rouet-Leduc et al., 2017), the spatial distribution of aftershocks (DeVries et al., 2018), or the magnitude (González et al., 2019).

We propose here, for the first time, the use of Recurrent neural networks (RNN) to capture the preparatory phase of moderate earthquakes by studying the spatio-temporal evolution of micro-seismicity.

To this aim, we focus on data relevant to The Geysers geothermal field in California (Figure 4-2). The crustal volume below The Geysers can be seen as a complex physical system whose stress field evolves due to the interaction of tectonic processes and industrial operations in a chaotic way. Our aim is to verify if larger events are anticipated by transients in features sensitive to the evolution of the crustal damage process.

The Geysers hosts a high quality, dense seismic network to monitor the high seismicity rate since 2003 (Viegas and Hutchings, 2011). Considering the period between 2003 and 2016, indeed, the official catalogue (NCEDC, <https://ncedc.org/egs>) includes ~460.000 events in the magnitude range between  $M - 0.7$  and  $M 4.3$  (Figure 4-2a). Within this dataset, we have identified 8 events with moment magnitude larger than  $M_w 3.9$  (hereinafter,  $M4$  events) occurred between 2006 and 2014 within the geothermal field (Figure 4-2a, d), and we have estimated the completeness magnitude,  $M_c$ , being equal to  $M 0.5$  (Figure 4-1c), which, according to Mignan (2014), makes us hopeful to observe their preparatory phase. In this work, the available local magnitude,  $M_L$ , estimates available in the NCEDC seismic catalogue have converted in moment magnitude scale,  $M_w$  (Hanks and Kanamori, 1979; see section Methods for more details).

The seismic catalogue has been analyzed to extract nine features describing different aspects of the temporal and spatial evolution of seismicity. The considered features are: the  $b$ -value and completeness magnitude,  $M_c$ , of the Gutenberg-Richter law (Gutenberg and Richter, 1942, 1956); the fractal dimension of hypocenters,  $D_c$  (Grassberger and Procaccia, 1983, 2004); the generalized distance between pairs of earthquakes,  $\eta$  (Zaliapin and Ben-Zion, 2013); the Shannon's information entropy,  $h$  (Shannon, 1948; Telesca et al., 2004; Bressan et al., 2017); the moment magnitude,  $M_w$ , and moment rate,  $\dot{M}_0$ ; the total duration of event groups,  $\Delta T$ , and the inter-event time,  $\Delta t$  (see section Methods for more details about the seismic features).

The crustal volume below The Geysers can be seen as a complex physical system which stress field evolves due to the interaction of tectonic processes and industrial operations in a chaotic way. In similar conditions, our aim is to verify if larger events are anticipated by transients in features sensitive to the evolution of the crustal damage process.

We look for transients with respect to the stationary occurrence in seismicity that could hints for the preparation process of larger earthquakes. So, besides the typical features related to the rate, inter-event time and seismic moment rate of events, we have explored the use of features carrying information on the stress condition of the crust and on the evolving characteristics of earthquake patterns.

Laboratory studies (Goebel et al., 2012; Kwiatek et al., 2014) have shown that variations in the frequency-magnitude earthquakes distribution, expressed in terms of the  $b$ -value of the Gutenberg-Richter law (Gutenberg and Richter, 1942, 1956), were connected to higher density of fractures and moment release. Recently, it has been shown (Gulia and Wiemer, 2019) that transients in  $b$ -value in aftershock zones can be used to foresee if after a large event an even stronger one yet to come. These observations are related to the connection existing between  $b$ -value and the stress conditions associated to ruptures (Amitrano, 2003; Scholz, 2015).

#### 4. Forecasting the Preparatory Phase of Induced Earthquakes by Recurrent Neural Network

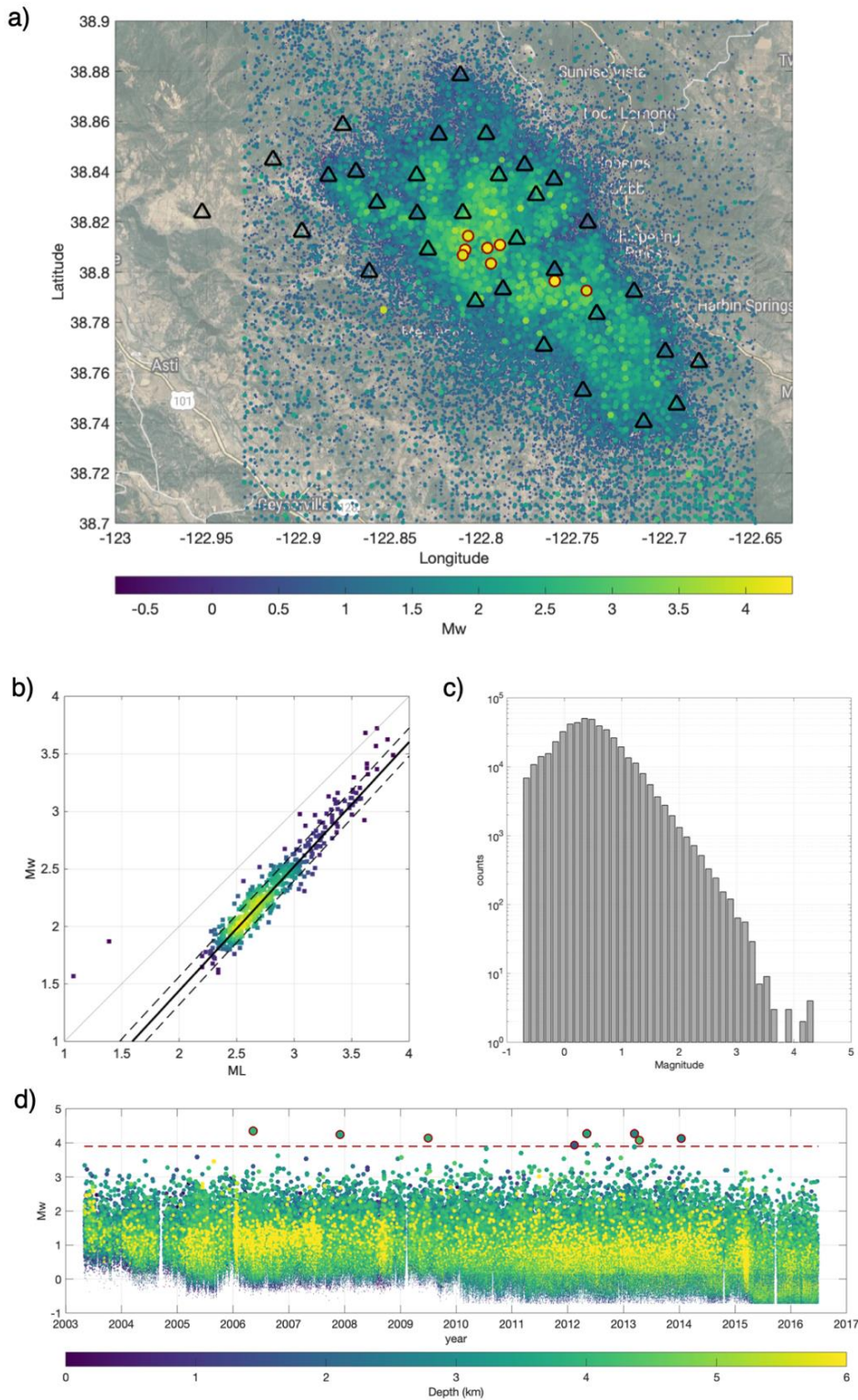


Figure 4-2: (a) Locations of the earthquakes considered in this study (data are colored and have size varying per  $M_w$ ) and seismic stations of the Berkeley-Geysers, BG code, seismic network (black triangles).  $M_4$  earthquakes are identified by a red contour. The map was made using MATLAB (R2019b; <https://it.mathworks.com/>, last accessed May 2021). (b) Local magnitude, ML, versus moment magnitude,  $M_w$  scatter plot (viridis color scale with yellow for higher density of data). The trend lines defined by linear regression is shown in black (thick black line) along with their  $\pm 1$  standard deviation (upper and lower dashed black lines). The 1:1 scaling line is also reported (thin black line). (c) Histogram showing the distribution of magnitude for the considered events. (d) Temporal distribution of magnitude (data are colored and have size varying per hypocentral depth).  $M_4$  earthquakes are identified by a red contour.  $M_{3.9}$  threshold (red dashed line).

A further point of view in studying microseismicity is provided by the fractal dimension of hypocenters (Grassberger and Procaccia, 1983, 2004),  $D_c$ , which has been reported to vary before large earthquakes (De

#### 4. Forecasting the Preparatory Phase of Induced Earthquakes by Recurrent Neural Network

Rubeis et al., 1993; Legrand et al., 1996; Murase, 2004). As discussed by many authors on both theoretical and experimental basis (Aki, 1981; King, 1983; Henderson and Main, 1992; Main, 1992; Wyss et al., 2004; Goebel et al., 2017), b-value and  $D_c$  are strongly correlated, especially when the self-similar scaling assumption for earthquakes holds. Following the computation of b-value and  $D_c$ , we have estimated the generalized distance between pairs of earthquakes (Zaliapin and Ben-Zion, 2013),  $\eta$ , which includes the contribution of both of them.

Finally, we have quantified the level of organization of the earthquakes population in our complex dynamic system by the Shannon's information entropy (Shannon, 1948; Telesca et al., 2004; Bressan et al., 2017).

The sequential data (features) have been analyzed by the Gated Recurrent Units (GRU) (Cho et al., 2014), an advanced RNN with strong capability of analyzing data non-linearly correlated and characterized by long-term trends that classic RNN algorithms are not able to handle. Throughout the last years, applications of similar algorithms (i.e., the LSTM, Hochreiter and Schmidhuber, 1997) and other neural network (Panakkat and Adeli, 2007; Reyes et al., 2013) for earthquake prediction have been proposed, but the literature survey proposed by Mignan and Broccardo (2020) led the authors to conclude that "the potential of deep learning to improve earthquake forecasting remains unproven".

In our work, we explored if RNN can detect and exploit the complex pattern of different potential seismic precursors to unveil the preparatory processes of larger magnitude induced earthquakes.

Our sensitivity analysis highlighted that among the selected features, some are more efficient in detecting the preparatory phase, while others performed better for the automatic identification of aftershocks. For these reasons, we trained two RNNs on five series of hundreds to thousands of earthquakes around M4 events occurred at The Geysers in the period 2006-2012.

Our cutting-edge outcome, from the application of the RNNs to three earthquakes series occurred in the same area after 2013 and including M4 events, is that for all of them several hours of preparatory phase can be automatically identified. Our results demonstrate that machine learning approaches have high potential of catching complex pattern in seismic features and assisting operators in the induced seismicity management.

The monitoring of induced seismicity is a peculiar context, where the availability of high quality and dense seismic networks lead to enriched catalogues that in turns can allow high quality training of artificial intelligence approaches. And yet, we believe our study will also stimulate other researchers to explore similar multi-parameters machine-learning approaches to areas where natural large magnitude earthquakes occur.

## 4. Forecasting the Preparatory Phase of Induced Earthquakes by Recurrent Neural Network

### 4.2. Features

#### 4.2.1. Features computation and general working outline

Information extracted from the seismic catalogue (i.e., hypocenter coordinates, local magnitude, and occurrence date and time) are used to compute the series of features used by RNNs.

We followed the same analysis scheme for all features (Figure 4-3a) but for  $M_w$  and  $\Delta t$  that are computed for each single event. That is to say, the features are computed on windows of  $n$  events (with  $n = 200$ ) and their value is assigned to the  $n$ th event at the time  $t_i$  and windows move of one event at time [i.e., each feature represents a time series]. Here,  $n$  equal to 200 was selected considering that this parameter is important for obtaining robust estimates of the  $b$ -value (Marzocchi et al., 2020). For instance, Dresen et al. (2020), used  $n$  equal to 150.

In the following, we detail the computation of features (sections from 4.2.2 to 4.2.7), while we describe in section 4.3 the RNN algorithm and the step-by-step procedure implemented in our study.

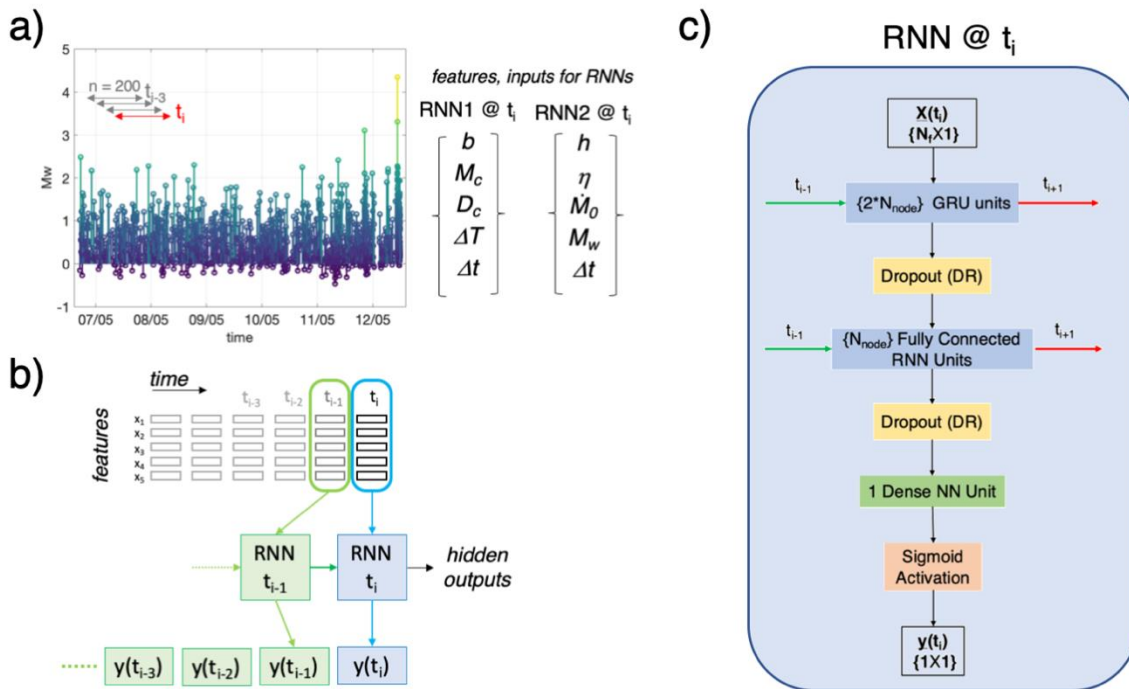


Figure 4-3: Overview of the RNN-based preparatory phase prediction. (a) Computation of features on moving windows of  $n$  events. (b) Outline of the RNNs algorithms. (c) Outline of the RNN architecture at time  $t_i$ .

#### 4.2.2. Duration of event groups and inter-event time

We compute for each window of  $n$  events the total duration of event groups ( $\Delta T = t_n - t_{1st}$ ) and the inter-event time ( $\Delta t = t_n - t_{n-1}$ ).

## 4. Forecasting the Preparatory Phase of Induced Earthquakes by Recurrent Neural Network

### 4.2.3. Moment Magnitude and Moment rate

We converted the local magnitude ( $M_L$ ) in moment magnitude scale ( $M_w$ ) benefiting from the characterization of around six hundred earthquakes at The Geysers (M. Picozzi et al., 2017)(i.e., characterized in terms of seismic moment,  $M_0$ , and corner frequency, Figure 4-2b). The  $M_0$  values have been thus converted in  $M_w$ , and we parameterized the following  $M_L$  vs  $M_w$  relationship:

$$M_w = 1.08 \cdot M_L - 0.72, \quad \sigma = 0.12, \quad (1)$$

The moment rate,  $\dot{M}_0$  is then computed for each analysis window of  $n$  events (i.e.,  $n = 200$ ) and temporal length ( $\Delta T$ ) as:

$$\dot{M}_0 = \frac{\sum_{i=1}^n M_{0i}}{\Delta T} \quad (2)$$

### 4.2.4. b-value and completeness magnitude $M_c$

The analysis of the cumulative frequency-magnitude distributions to estimate the b-value of the Gutenberg-Richter law (Gutenberg and Richter, 1942, 1956)

$$\log N = a - b \cdot M_w, \quad (3)$$

where  $N$  is the cumulative number of earthquakes,  $a$  and  $b$  values are parameters describing the productivity and relative event size distribution, is carried out exploiting the entire-magnitude-range method (Woessner and Wiemer, 2005) implemented in the software package ZMAP (Wiemer, 2001) and allows for the simultaneous estimate of the completeness magnitude  $M_c$  and the parameters  $a$  and  $b$  (i.e., this latter obtained by the maximum likelihood approach, Aki, 1965).

### 4.2.5. Fractal Dimension

The fractal dimension of earthquake hypocenters,  $D_c$ , is computed applying the correlation integral method (Grassberger and Procaccia, 1983, 2004; Henderson et al., 1999):

$$D_c = \lim_{r \rightarrow 0} \frac{\log C_r}{\log(r)} \quad (4)$$

where  $r$  is the radius of a sphere of investigation and  $C_r$  is the correlation integral:

$$C_r = \lim_{n \rightarrow \infty} \frac{1}{n^2} \sum_{i=1}^n \sum_{j=1}^n H(r - |x_i - x_j|) \quad (5)$$

#### 4. Forecasting the Preparatory Phase of Induced Earthquakes by Recurrent Neural Network

with  $n$  indicating the number of data in the analysis window (i.e.,  $n = 200$  events),  $x$  the hypocenter coordinates, and  $H$  the Heaviside step function  $H(x) = 0$  for  $x \leq 0$  and  $H(x) = 1$  for  $x > 0$ . In other words,  $C_r$  is a function of the probability that two points will be separated by a distance less than  $r$  (Henderson et al., 1999).

The fractal dimension  $D_c$  is therefore the slope of the best fit straight line of  $C_r$  versus the distance  $r$  in a bi-logarithmic diagram.

##### 4.2.6. Nearest-neighbor distance, $\eta$ , analysis

The nearest-neighbor approach (Zaliapin et al., 2008; Zaliapin and Ben-Zion, 2016) is based on the computation of the generalized distance between pairs of earthquakes,  $\eta$ , from the analysis of the time-space distances between pairs of earthquakes. The parameter  $\eta$  is derived computing the distances in time (i.e., rescaled time,  $T$ ) and space (i.e., rescaled distance,  $R$ ) between an event  $i$  and its parent  $j$  normalized by the magnitude of the parent event:

$$T_{ij} = t_{ij} 10^{-bm_i/2} \quad (6)$$

$$R_{ij} = (r_{ij})^{D_c} 10^{-bm_i/2} \quad (7)$$

where,  $m$  is the magnitude ( $M_w$ ),  $b$  is the parameter of the Gutenberg-Richter law (see Section 4.2.4),  $t$  is the earthquake interoccurrence time,  $r$  is the earthquake distance, and  $D_c$  is the fractal dimension. The values of  $b$  and  $D_c$  are changed according to the estimates obtained for the considered window of events.

Finally,  $\eta$  is defined as:

$$\log \eta_{ij} = \log R_{ij} + \log T_{ij} \quad (8)$$

(see (Zaliapin and Ben-Zion, 2016) for further details).

##### 4.2.7. Shannon's Information Entropy

The Shannon entropy, also known as information entropy (Shannon, 1948) provides a measure of the disorder level in a system. We compute the Shannon entropy using a regular 2-D grid ( $m = 441$  cells, each  $1.1 \text{ km} \times 1.5 \text{ km}$ ).

We compute the Shannon entropy as:

$$H = - \sum_{k=1}^m \frac{e_k}{E_R} \left[ \ln \frac{e_k}{E_R} \right] \quad (9)$$

where  $e_k$  represents a fraction of the total seismic energy  $E_R$  radiated within the  $k^{\text{th}}$  cell (Bressan et al., 2017). The  $e_k / E_R$  ratio is assumed to represent an empirical approximation of the probability of the seismic energy radiated in the  $k^{\text{th}}$  cell,  $P_k(E_R)$ , with respect to the total radiated seismic energy, conditioned on the total energy radiated.

## 4. Forecasting the Preparatory Phase of Induced Earthquakes by Recurrent Neural Network

Eq. (9) can therefore be rewritten as:

$$H = - \sum_{k=1}^m P_k(E_R) [\ln P_k(E_R)] \quad (10)$$

Therefore, computing  $H$  at a given temporal interval consists of summing up the  $e_k / E_R$  ratio for the entire grid.

We computed the radiated seismic energy  $E_R$  using the relation between local magnitude  $ML$  and seismic energy proposed for California by Kanamori et al. (1993):

$$ER = 1.96 \cdot ML + 2.05 \quad (11)$$

To allow comparison between different time intervals and to ensure unity total probability,  $H$  is generally normalized to the equipartition entropy  $H_E$ , which corresponds to the case where  $E_R$  is uniformly distributed in the cells (i.e., Eq. 9 with  $e_k = E/m$ ). The normalized information entropy  $h = H/H_E$  ranges between 1 and 0, which correspond to the total disorder of the system and the extreme concentration of events, respectively.

The Shannon entropy concept provides hence a useful quantification of the system predictability; where  $h = 0$  suggests the highest level of predictability and  $h = 1$ , on the contrary, suggests high disorder and low predictability.

### 4.3. Methods

In this section, we describe the RNN method that we developed to identify the preparatory phase of M4 earthquakes in The Geysers region and the aftershocks. For both goals, we used the same RNN algorithm, but we considered different sets of features as input and different targets. Each RNNs exploits five features, whereas only  $\Delta t$  is used by both algorithms (Figure 4-3a). We call the configuration used to distinguish the preparatory phase RNN1, while we refer at the one used for the aftershocks phase as RNN2.

As said, we selected eight series of events including M4 earthquakes as case study. Hereinafter, each set of earthquakes is referred to as M4 series. The first five M4 series, in chronological order, were exploited as train sets and to optimize the method through different validation techniques. Conversely, the test sets, consisting of the three more recent M4 series, was used downstream from all the other analyses to evaluate the methods performance and reliability.

#### 4.3.1. Recurrent Neural Networks and ML layers

Before going into details with the ML scheme, it is important to fix some ideas. An artificial neuron is a mathematical function that can be linear or not between input and output, which depends on coefficients whose optimization is done by a training. As example, a fully connected neuron gives as output a linear combination of all the inputs, also adding a bias. A neural network (NN) is an ensemble of neurons

#### 4. Forecasting the Preparatory Phase of Induced Earthquakes by Recurrent Neural Network

organized in various layers, each one with a certain number of neurons (also called nodes or units). The final model, in any case, will be a very complex mathematical function that can be very difficult to enroll and to understand. Despite that, the model will be almost completely data driven and so, if well trained, trustworthy.

Usually, NN layers are controlled by a set of hyperparameters that allows the model to fit the data. These hyperparameters are tuned by users, generally through a validation procedure. One of the most common hyperparameters is the learning rate. This latter is a small positive number that controls how much the model changes at each iteration, when a gradient descent technique is used to fit the data. Choosing a proper learning rate value is an important issue, because too small values can increase the computation time, conversely a too big one can hinder the model convergence.

In Figure 4-3b, we outline the functioning of an RNN. A key issue is that the RNNs see the data as connected sequential information. In our analysis, the data are time-connected, so the method looks at the information available at a given instant (i.e., used by RNN at  $t_i$ , Figure 4-3b) and at the same time it keeps also that one from the previous step (i.e., that from RNN at  $t_{i-1}$ ). This working strategy with memory of the past makes the output causal, and so particularly suitable for real-time applications. Despite that, the procedure proposed in this work is to be intended as off-line application; nevertheless, we will try to put it in real-time testing in future studies.

As we said, the NNs are organized in layers, so that they form the RNNs too. However, as can be seen in Figure 4-3c, the NN layers are usually different each other. In this study, we use two different kind of recurrent layers: fully connected RNN (Rumelhart et al., 1986) and GRU (Cho et al., 2014). Each RNN node (or unit, or neuron) has two inputs and two outputs. One of the RNN inputs comes from the previous layer, while the other input comes from the same unit at the previous instant. Similarly, one output goes to the same unit at next instant (hidden output), while the other output goes to the next layer. In a fully connected RNN unit, the hidden output is a linear combination of the two inputs, instead, the output towards the next layer is a linear combination of the inputs and of the hidden output. GRU is a more complex model than the previous one; it exploits logical gates to avoid the “vanishing gradient problem” (Hochreiter, 1998).

Like we said, NN are formed by layers of multiple neurons. Since each neuron of a layer is connected with all the neurons of the next layer through the output, this enormous number of relations can cause redundancy in the model, which can result into too deep models and overfitting. The dropout layers help to reduce the problem of overfitting (Srivastava et al., 2014). These layers cut a certain number of connections between other two layers forcing the model to train in the simpler possible way. Each dropout layer is controlled by a dropout rate (DR), which represents the fraction of clipped connections.

Finally, our RNN includes an activation layer that simply transforms the input in an output through a mathematical operator (i.e., a sigmoid function, Figure 4-3c), and it is generally used to add non-linearity to the model.

Figure 4-3c provides a comprehensive view of the RNN scheme implemented in this work. The entire input dataset is a matrix  $\{N_f \times N_e\}$ , where  $N_f$  is the number of features and  $N_e$  is the number of events for each M4 series. At each step, the model is fed with the features vector  $\{N_f \times 1\}$  that contains the values computed at the current instant  $t_i$ . The first hidden layer is formed by  $2 \cdot N_{node}$  GRUs. The outputs of this layer go through a dropout layer (characterized by a DR value). The third hidden layer is made by  $N_{node}$  fully connected RNN nodes. After this latter layer, we put another dropout layer with the same DR as the one before. The fifth hidden layer is formed by a single fully connected NN node; this yields the final output through a sigmoid activation layer that allows the output to vary between 0 and 1. The output has a single value for each instant, so it will be a vector  $\{1 \times N_e\}$ .

## 4. Forecasting the Preparatory Phase of Induced Earthquakes by Recurrent Neural Network

### 4.3.2. Step-by-step description of data-analysis by RNN

1. Once the spatial-temporal characteristics (features) of seismicity have been extracted, we selected windows of data for the RNN analyses (i.e., 750 and 2000 earthquakes around the five M4 events for RNN1 and RNN2, respectively). In particular, for each M4 series in RNN1, we consider 499 events before the M4 event, the M4 itself, and 250 events after it. For RNN2, instead, we consider 1500 events before the M4, the M4 itself, and 499 after it. The different amount of data in the M4 series for RNN1 and RNN2 has been tuned for optimizing the training performance.
2. Each M4 series has been standardized, which consist of, for each selected window, removing the mean and dividing for the standard deviation. This procedure is necessary since features span varying degrees of magnitude and units and these aspects can degrade the RNN performance (Shanker et al., 1996). After the standardization, each feature is distributed as a standard normal distribution,  $N(0,1)$ .
3. In order to train the models, we assigned a label to each earthquake. Indeed, being RNN used here for sequential data classification, it is necessary train it with a simple binary (0/1) classification scheme. Therefore, in RNN1, the one aiming to identify the preparatory phase, we assigned value 1 to those events preceding the M4s that have been interpreted based on expert opinion as belonging to the preparatory phase and label 0 to all the others (background and aftershocks). In RNN2, aiming to identify aftershocks, we assigned label 1 to aftershocks and label 0 to the others (background and foreshocks). In particular, in RNN1, for each M4 series, we selected a different number of events as belonging to the preparatory phase (i.e., ranging from 175 to 350 events) looking at the trend of parameters like  $b$ -value,  $M_c$  and  $D_c$  that we know likely related to the preparatory phase (Dresen et al., 2020). In RNN2, we decided to label all the 499 events following a M4 as aftershocks.

The rationale of our choice is that all features except two ( $M_w$  and  $\Delta t$ ) are computed on group of events (i.e., each window  $n = 200$ ). Therefore, the features value at a given instant represents the collective behavior of a group of earthquakes, and it becomes not straightforward to single out, on this basis, if the last event of each window (i.e., the event at  $t_i$ ) is a foreshock, or it belongs to the background seismicity (and similarly for aftershocks and background seismicity). Moreover, these considerations brought us also to avoid considering the location of these events (i.e., latitude, longitude and depth of the earthquakes are not used directly as features, but indirectly through  $D_c$ ,  $\eta$  and  $h$  as collective characteristic of the seismicity), both for RNN1 and RNN2. Our aim during the training phase is to push RNN1 and RNN2 to find coherent correlation among features and to detect changes in the stationary character of the seismicity, which can correspond to the preparatory phase of a large earthquake and to aftershocks, respectively. It is important to note also that our strategy can be a two-edged sword, since the presence of misled background seismicity in both the preparatory and aftershock phases can lead to an underestimation of the performances falsely enhancing the number of missed events. In both cases, we thus make the RNNs work more challenging, and we test its capability to mine and detect coherent correlation among seismic features.

4. The event catalogue is therefore transformed into two datasets (train and test) for RNN, in which lines contain the features and the labels (i.e., for line  $i$ , corresponding the at origin time of  $i$ th event, we have  $\{b\text{-value}_i, M_{ci}, D_{ci}, \Delta T_i, \dot{M}_{0i}, \Delta t_i, \eta_i, h_i, M_{wi}, label_{1i}, label_{2i}\}$ ).
5. We split the dataset in training and testing sets. The train set consists of the first five M4 series, while the testing one consists of the last three M4 series.

## 4. Forecasting the Preparatory Phase of Induced Earthquakes by Recurrent Neural Network

6. We trained the model to find the best hyperparameters, which of course, could change between RNN1 and RNN2.
7. The model has been validated on the train set separately (with the proper label) for RNN1 and RNN2 using a trial-and-error procedure to select the best features for the two models, and a Leave-One-Out (LOO) cross-validation to tune the hyperparameters. The LOO is performed leaving one M4 series per time and training the model on the other four. Hence, each model resulting from four M4 series is used to predict the target on the excluded M4 series. We decided to use AUC (Area Under the Curve) as validation score because it is independent from the threshold selection. The mean of the five AUC values from the LOO validation is used to evaluate the hyperparameters configuration. We chose to explore three hyperparameters, which are Nnode (in the range 3-20), DR (between 0 and 0.5), and the learning rate LR (between  $1e-5$  and  $1e-3$ ) with which the model is fitted.
8. A similar Leave-One-Out (LOO) approach has been carried out also to perform a feature importance analysis. In this case, considering the five M4 series, we proceeded at removing one by one features and checking the performance with respect to the case with all features. On one hand, our tuning led to select for RNN1 the features *b-value*,  $M_c$ ,  $D_c$ ,  $\Delta T$ , and  $\Delta t$ . On the other hand, we selected for RNN2 to features  $\dot{M}_0$ ,  $\Delta t$ ,  $\eta$ ,  $h$ , and  $M_w$ .
9. The performance of the RNN1 and RNN2 models has been assessed using the testing dataset of three M4 series.

### 4.4 Results

#### 4.4.1 Observing seismicity occurrence from features perspective

As discussed, we took advantage of the information on event date and time of occurrence, location, depth, and local magnitude extracted from The Geysers' seismic catalogue to observe the temporal and spatial evolution of seismicity. To study the frequency magnitude events distribution in terms of the Gutenberg-Richter relationship (i.e., *b-value* and  $M_c$ ), we converted the local magnitude,  $M_L$ , in moment magnitude scale,  $M_w$ . The ML scale has also been used to derive estimates of the radiated energy,  $E_R$ , which in turn has been utilized to compute the Shannon's information entropy,  $h$ . These pieces of information were transformed in data time features: *b-value*,  $M_c$ , Shannon's information entropy ( $h$ ), fractal dimension ( $D_c$ ), generalized distance between pairs of earthquakes ( $\eta$ ), Moment rate ( $\dot{M}_0$ ), inter-event time ( $\Delta t$ ), total duration of event groups ( $\Delta T$ ), and  $M_w$ .

The first M4 event recorded in the area occurred in May 2006. The temporal evolution of features associated to earthquakes preceding this event shows, approximately the day before, peculiar trends with respect to the preceding background seismicity, which for the sake of simplicity have been highlighted (Figure 4-4, red values). For most of features, these trends correspond to a more-or-less pronounced decrease (e.g., *b-value*,  $M_c$ ,  $D_c$ ,  $\Delta T$ ,  $h$ ,  $\eta$ ,  $\Delta t$ ), while  $\dot{M}_0$  it increases.

Besides the events preceding the M4, we found peculiar also the features trend after it (Figure 4-4, blue values). The features show, indeed, considerable decrease or increase also for aftershocks.

The standardized features for the first five M4 earthquakes (Figure 4-5), occurred between 2006 and 2012, show coherent trends (i.e., *b-value*,  $M_c$ ,  $D_c$ ,  $\Delta T$ , and  $\Delta t$  for the phase preceding the mainshocks, while  $\dot{M}_0$ ,  $\Delta t$ ,  $\eta$ ,  $h$ , and  $M_w$  for the period following it).

#### 4. Forecasting the Preparatory Phase of Induced Earthquakes by Recurrent Neural Network

Following these observations, we decided to explore the capability of RNN in capturing the long-term trends in data and the, likely non-linear, correlation among features.

With respect to the trend associated to background seismicity, both what we assume being the preparatory phase and the aftershocks occurrence represent transients. While the automatic discrimination of aftershocks is for monitoring systems interesting in itself, this is especially true for us. As a matter of fact, the occurrence of transients associated to aftershocks might be confusing for the identification of transients associated to the preparatory phase of large earthquakes from background seismicity. For this reason, as discussed in Section 4.3, we decided to train two RNNs: one dedicated to the preparatory phase (RNN1), and another aiming to identify the aftershocks (RNN2). In the following, we describe first how RNNs have been trained and tested. Finally, we discuss how they could be combined for induced seismicity monitoring purpose at The Geysers.

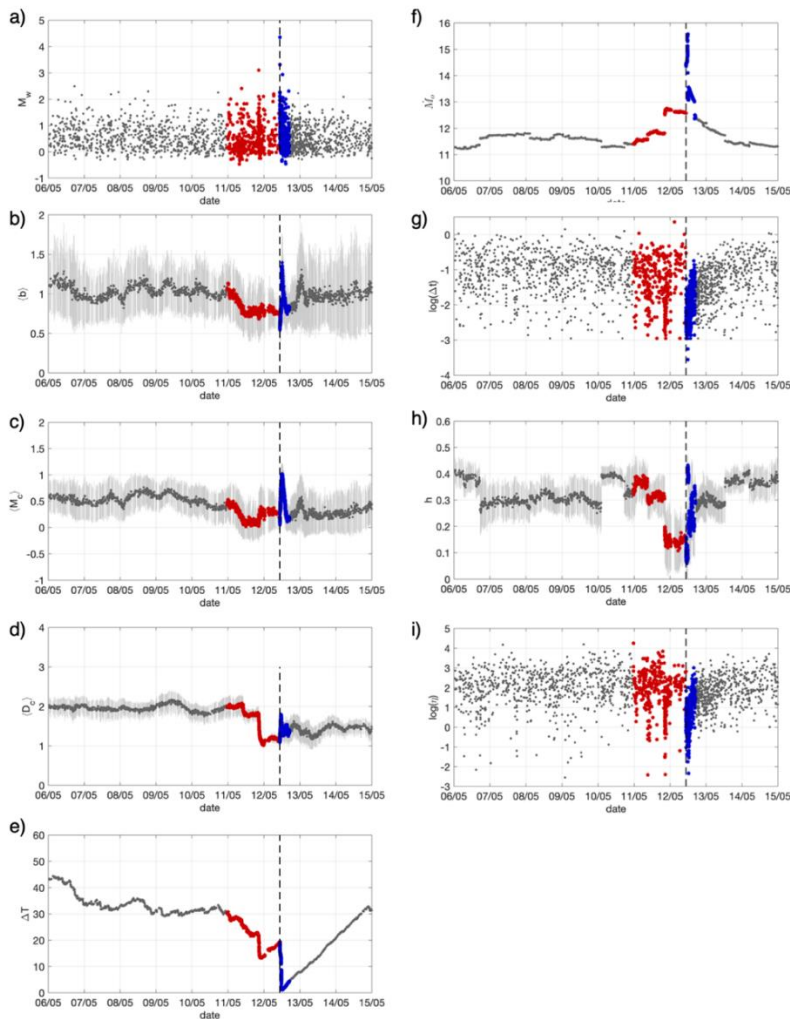


Figure 4-4: (a) Distribution of events before and after the first  $M_4$  earthquake (occurred the 12<sup>th</sup> of May 2006, vertical dashed line). Background seismicity (grey dots), foreshocks (red), main-event and aftershocks (blue). All the other plots are the same as (a), but for: (b) average  $b$ -values and  $\pm 1$  st.dev. bars (grey); (c) average completeness magnitude,  $M_c$ , and  $\pm 1$  st.dev. bars; (d) average fractal dimension,  $D_c$ , and  $\pm 1$  st.dev. bars; (e) total duration,  $\Delta T$ , of the events group; (f) Moment rate,  $\dot{M}_0$ ; (g) inter-event time,  $\Delta t$ ; (h) Shannon entropy,  $h$ ; (i) Logarithm (base 10) of the generalized distance between pairs of earthquakes,  $\eta$ . The uncertainty associated to  $b$ -value,  $M_c$ ,  $D_c$  and Shannon entropy  $h$  is computed by means of a bootstrap approach (Efron, 2007), whereas for each dataset 1,000 realizations of random sampling with replacement were performed.

#### 4. Forecasting the Preparatory Phase of Induced Earthquakes by Recurrent Neural Network

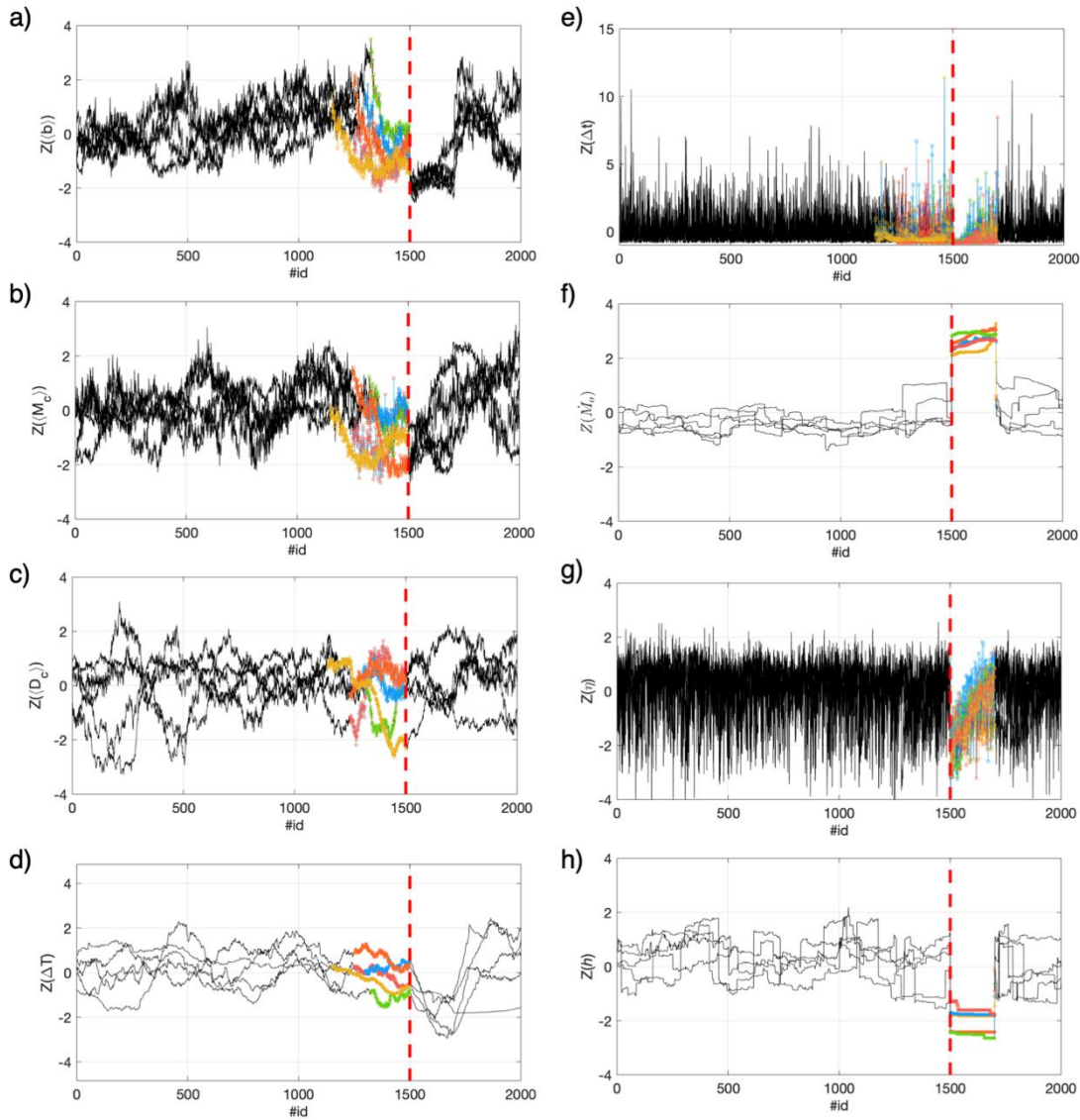


Figure 4-5: Features belonging to the training M4 series after standardization. Background seismicity (black), foreshocks and aftershocks (colored per event). Time of the M4s occurrence (vertical, dashed red line). Subplots show different features according to Figure 4-4.

##### 4.4.2 RNNs tuning through cross-validation on a training dataset

Figure 4-6a shows the events labelled 0 (i.e., belonging to stationary seismicity and aftershocks sequence, black dots) and 1 (i.e., belonging to the preparatory phase, green dots). Similarly, in Figure 4-6b, we show for the first five M4 series the events labelled 0 (i.e., background and foreshocks, black dots) and 1 (i.e., aftershocks, green dots)

To tune the RNNs parameters, we have carried out a leave-one-out (LOO) analysis using the 5-training series (i.e., each run, four M4 series are in and one is out). As discussed in section 4.3.2, we avoided to select a priori a threshold value, and we decided to study the variation of the AUC parameter (i.e., the area under the receiver operating characteristic, ROC, curve) as score of performance. The average of the five AUC values from the LOO has been used to select the best RNN1 and RNN2 models.

#### 4. Forecasting the Preparatory Phase of Induced Earthquakes by Recurrent Neural Network

We also performed a features importance analysis following an approach similar to LOO for assessing which features were optimizing the capability of RNN1 and RNN2 in identifying their targets. The results indicate that for RNN1 the best features are *b-value*,  $M_c$ ,  $D_c$ ,  $\Delta T$ , and  $\Delta t$ ; while for RNN2 it is better to use while  $\dot{M}_0$ ,  $\Delta t$ ,  $\eta$ ,  $h$ , and  $M_w$ .

##### 4.4.3 Training RNN1 and RNN2

In Figure 4-6c and Figure 4-6d, we show the trends of different performance criteria with the respect of the threshold used in the binary classification for RNN1 and RNN2, respectively. The ensemble of these criteria gives us a comprehensive statement on the model performances. To better understand why, let us introduce these criteria using the binary classification (positive/negative event): Recall represents how many positive events are well-classified; Precision, instead, is the rate of true positive on all the events classified as positive; Accuracy represents the rate of true predictions on the total of the predictions; Balanced Accuracy is the mean between the recall and the rate of negative events well-classified (also called selectivity, it is similar to Accuracy, but it does not suffer the unbalanced dataset); MCC, Matthew Correlation Coefficient (Matthews, 1975; Chicco and Jurman, 2020) is related to the general quality of the classification (we will dedicate more space to this specific parameter in the following).

Selecting the threshold equal to 0.7 for both RNN models, we think to have found a best compromise in terms of different performance criteria (Figure 4-6c and Figure 4-6d). Therefore, we used this threshold for both the RNN1 and RNN2 best models applied again to the five M4 training series (Figure 4-6a, b, e, and f).

Concerning the preparatory phase, we observe that a significant portion of the events with label 1 are correctly identified (i.e., for series '1', '2' and '3' the score overcome 0.7 in 74%, 53% and 68% of the cases, respectively). Only for the third and fourth time series the number events considered as belonging to a preparatory phase is reduced, but still the 14% and 18%, respectively (Figure 4-6a).

Similarly, also the RNN2 performance is convincing, since a high number of aftershocks has been correctly identified for all data series (Figure 4-6b). In this case, success rate varies between the 40% and the 66%. To assess the quality of our binary classification, we also exploited the Matthews correlation coefficient (MCC), which taking into account the rate of negatives and positives provides a measure of the correlation coefficient between the observed and predicted classifications (Matthews, 1975; Chicco and Jurman, 2020). MCC assumes value ranging between -1 and +1; whereas MCC equal to +1 represents a perfect prediction, equal to 0 indicates no better than a random prediction, and finally equal to -1 indicates total disagreement between prediction and observation.

For RNN1, we obtain MCC equal to 0.74, 0.60, 0.29, 0.26, and 0.66 for the testing M4 series number from 1 to 5, respectively. For RNN2, we obtain MCC equal to 0.77, 0.57, 0.57, 0.57 and 0.40 for M4 series number 1 to 5, respectively. These results indicate that RNN1 and RNN2 show, with respect to our labels assignment, a good prediction capability.

Besides the MCC scores, interestingly, we note that both before and after the mainshock a continuous set of events are classified as preparatory and aftershock phases, but for a total number smaller than the one considered by us. This means that the selected seismic features lead RNN1 and RNN2 be able to autonomously declare the preparatory phase be initiated and the aftershock sequence concluded, respectively.

#### 4. Forecasting the Preparatory Phase of Induced Earthquakes by Recurrent Neural Network

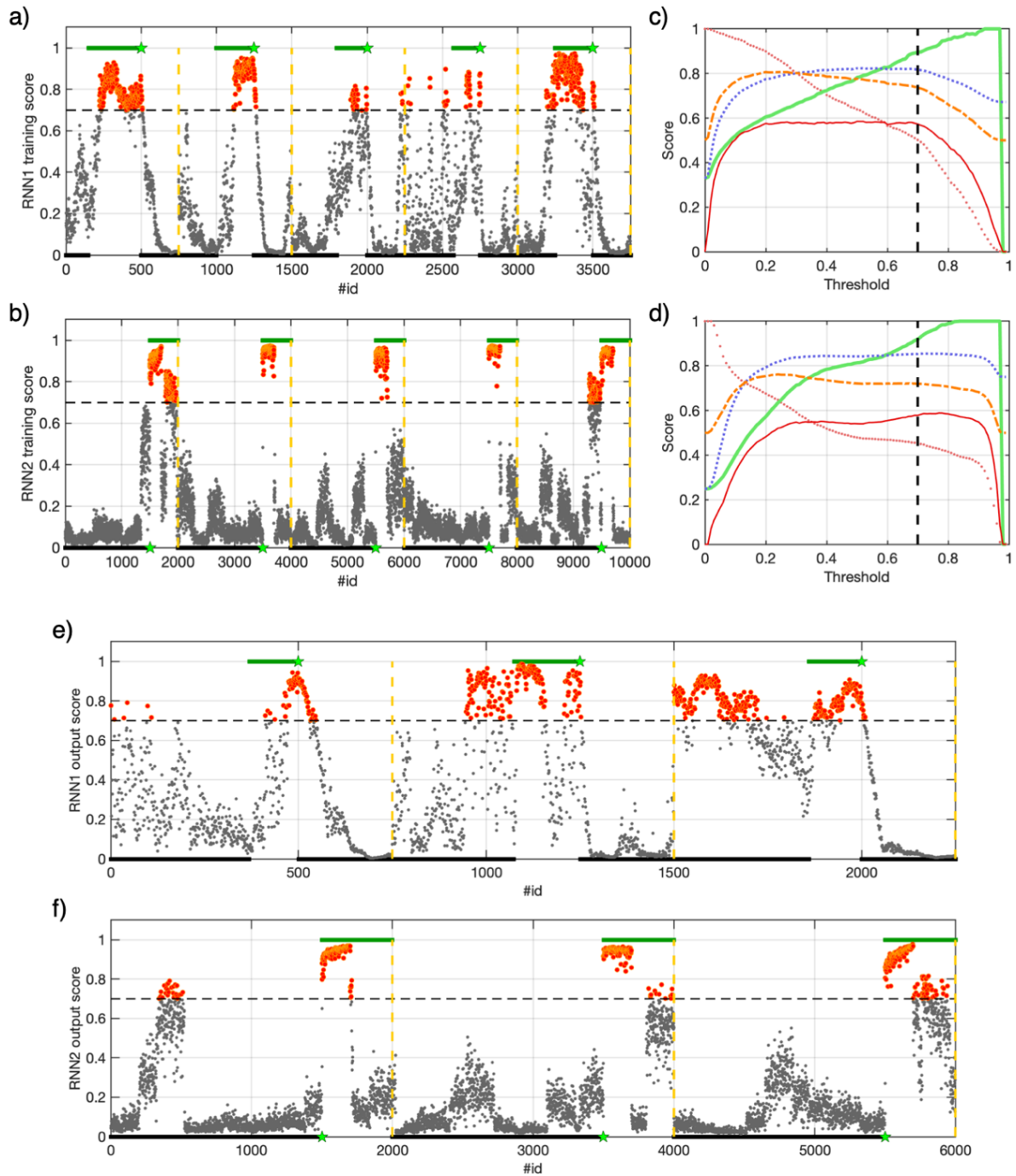


Figure 4-6: (a) RNN1 training. Labels for background and aftershocks (black), while for preparatory events (green), M4 events (green stars), end of the M4 series (vertical, dashed yellow line), selected threshold (horizontal, dashed black line), RNN1 output below the threshold (grey) and above it (orange). (b) The same as (a), but for RNN2 and with label for background and foreshocks (black), while for aftershocks (green). (c) Performance criteria versus threshold: recall (red dotted line), precision (thick green line), accuracy (blue square dotted line), balanced accuracy (dashed orange line) and MCC (thin red line) for RNN1. Selected threshold (vertical, dashed black line). (d) The same as (c), but for RNN2. (e) The same (a) but for the testing dataset and RNN1 (three M4 testing series). (f) The same as (b) but for the testing dataset and RNN2.

## 4. Forecasting the Preparatory Phase of Induced Earthquakes by Recurrent Neural Network

### 4.4.4 Testing RNN1 and RNN2

Intrigued by the training outcomes, we tested our RNNs on the remaining three M4 series, which have occurred between 2013 and 2014.

RNN1 results capable of identifying all three preparatory phases (success rate is 28%, 58% and 77% for events with label 1, respectively, Figure 4-6e). It is worth noting that RNN1 assigns score larger than the threshold also to events before what we defined from visual inspection as preparatory phase, but we will come back to this point later.

RNN2 provides good classification results too (Figure 4-6f); indeed, in this case the success rate in identifying aftershocks is 42% for the first two M4 testing series and 50% for the third one.

For RNN1, we obtain MCC equal to 0.251, 0.42 and 0.346 for the testing M4 series number 1, 2, and 3, respectively. For RNN2, we obtain MCC equal to 0.534, 0.597 and 0.653 for M4 series number 1, 2, and 3, respectively.

These results indicate that RNN1 and RNN2 provide good, not random predictions. We consider worth to remember, that the MCC scores is computed with respect to our labels assignment, which we kept large on purpose and could include together with earthquakes of the preparatory phase and aftershocks also events belonging to the background seismicity (see section 4.3.2 issue #3).

Similarly to the training case, we observe that RNN1 and RNN2 lead the preparatory phase and aftershock sequences start after and conclude before, respectively, with respect our labels assignment. However, once a non-stationary phenomenon is detected, the classification does not jump from 0 to 1 randomly, but RNNs hold it stably; indicating that the RNNs are able to autonomously discriminate the events belonging to the preparatory phase and aftershocks sequence from those of the stationary, background seismicity.

### 4.4.5 Conceptualization of an alert algorithm

The goal of our study is to show that the identification of the preparatory phase of large earthquakes is becoming an achievable task when the temporal and spatial evolution of seismicity is monitored by dense local networks. Although we are only moving the first steps towards the possibility of implementing an operational algorithm for earthquake forecasting, here we conceptualize an application of our RNN models for detecting when the seismicity is evolving along the preparatory phase of large magnitude event at The Geysers.

Our scheme considers the RNN scores as probability values (i.e., in RNN1 the score represents the probability for the event of belonging to the preparatory phase, while in RNN2 it means the probability of being an aftershock).

We thus combine the two RNN probabilities in an alert probability ( $P_{ALERT}$ ) as follows:

$$P_{ALERTi} = P_{RNN1i} \cdot (1 - \langle P_{RNN2(i-9:i)} \rangle) \quad (12)$$

where  $P_{RNN1i}$  is the probability associate to event  $i$  and  $\langle P_{RNN2(i-9:i)} \rangle$  is the average of probabilities associated to  $i$  and the previous nine events. The need to consider the average of ten  $P_{RNN2}$  is related to the aim of stabilizing the  $P_{ALERT}$  for a given event. Indeed, as can be seen in Figure 4-6b or Figure 4-6f, even if for background seismicity and foreshocks RNN2's outputs are very small (i.e., between 0 and 0.4), every change in  $P_{RNN2}$  would lead to oscillation in  $P_{ALERT}$ . It is worth to remember that Eq. (12) represents just a simple example of possible criteria for combining the RNNs' outputs. The proposed alert system outline is

#### 4. Forecasting the Preparatory Phase of Induced Earthquakes by Recurrent Neural Network

just an example which aims to show a potential future application of a similar research RNN products and to stimulate the debate about strategies for identifying the preparatory of induced and natural large earthquakes.

The temporal evolution of  $P_{ALERT}$  for the three M4 testing series shows interesting results (Figure 4-7). For the first M4 series, before the 14<sup>th</sup> of March, the selected probability threshold (i.e.,  $P_{thr} = 0.7$ ) is overcome by  $P_{ALERT}$  only rarely. Then, interestingly,  $P_{ALERT}$  overcomes stably the selected probability threshold around four hours before the mainshock (Figure 4-7a). For the second and third M4 series,  $P_{ALERT}$  overcome rather stably  $P_{thr}$  two and four days before the mainshocks, respectively. Moreover, in both cases, there is a drop in  $P_{ALERT}$  which is followed by a rapid increase above  $P_{thr}$  few hours before the mainshock (Figure 4-7b and Figure 4-7c).

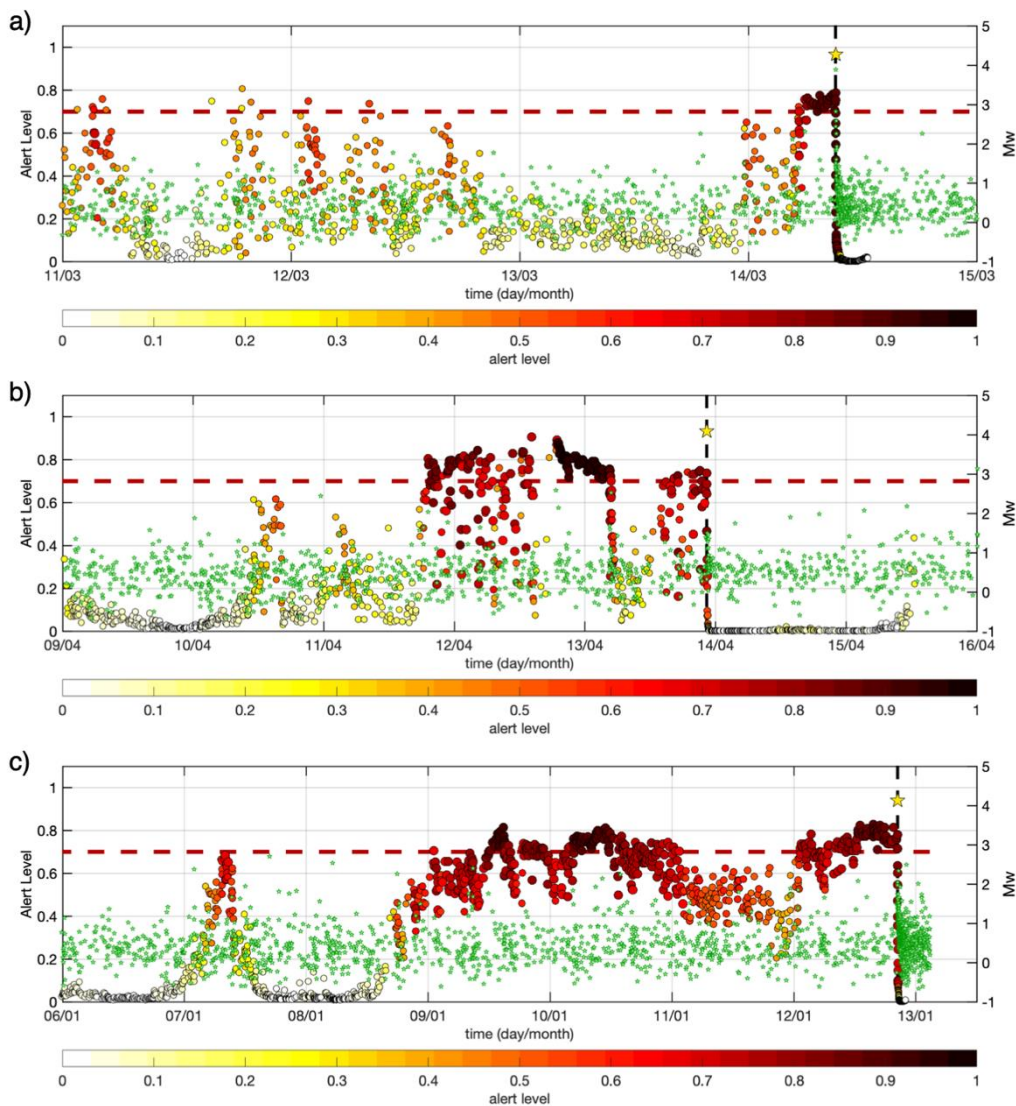


Figure 4-7: Application of RNN1 and RNN2 combined into a prototype of alert system to the three M4 testing series. (a) Distribution of event magnitude in time (green stars and right-side y-axis) for the M4 that occurred on the 14<sup>th</sup> of March 2013 (yellow star). The threshold alert level (dashed red line) and alert probability ( $P_{ALERT}$ ) refer to the left-side y-axis.  $P_{ALERT}$  are dots colored and with size varying according to their values (i.e., from white, no alert, to dark red for events above the threshold alert level). (b) The same as (a), but for the M4 that occurred on the 14<sup>th</sup> of April 2013. (c) The same as (a), but for the M4 that occurred on the 13<sup>th</sup> of January 2014.

## 4. Forecasting the Preparatory Phase of Induced Earthquakes by Recurrent Neural Network

### 4.5 Discussion

Given the very high rate of seismicity (>10,000 earthquakes/year) and the high-quality seismic network, The Geysers represents a perfect natural laboratory for studying the rupture processes and nucleation of induced earthquakes. The interaction of industrial activities associated to many injection wells with the tectonic stress suggests a complex stress-field, a puzzle difficult to resolve with standard approaches. Our results indicate that the spatial and temporal evolution of seismicity can be unveiled by benefiting of only information obtainable from seismic catalogue and using machine learning.

The seismicity in the area occurs mostly at shallow depth in relation to the ~70 water injection wells and predominantly related to thermal stress (Martínez-Garzón et al., 2014). However, the largest events (M4) occur confined in the deepest portion of the reservoir, have relatively high stress drop values, and result spatially distributed in agreement with the regional fault trend (M. Picozzi et al., 2017), characterized by right-lateral strike-slip faults. Their occurrence is therefore interpreted as due to the reactivation of deep structures linked to regional tectonics (Kwiatek et al., 2015). It is out of the scope of this work to investigate the physical mechanism driving the generation of M4 events and settle the controversy between earthquake foreshock theories.

Our application at The Geysers suggests, however, that the M4 earthquakes are preceded by preparatory process of the mainshocks compatible with the loading view (Das and Scholz, 1981; Ohnaka, 1992; Mignan, 2014; Kato and Ben-Zion, 2021).

Our results show that the preparatory phase for the three testing M4 earthquakes lasted from few hours to few days, in agreement with the short-time preparation process (~1 day) observed for a similar magnitude natural earthquake (Mw 4.4) occurred recently in Italy (Sánchez-Reyes et al., 2021). Future work will explore the application of RNN to the real-time identification of the preparatory phase at The Geysers and other areas where induced seismicity occurs.

Furthermore, we will test whether seismic derived features as those used in this study can allow to identify the preparatory phase of large magnitude natural earthquakes too. Our approach can potentially set marked advances in the earthquake predictability research.

## 5. Conclusions

During my PhD, I studied the implementation of new techniques in onsite EEW framework. I focused, in particular, on the prediction of parameters of engineering interest: the acceleration response spectra (RSA) and the structural drift. The second topic of my research was the detection of the preparatory phase of induced events through the use of ML techniques.

In the first work, we trained different models for the prediction of the RSA at 9 periods using the mixed-effect regression from P-wave parameters. Here, we showed how the use of non-ergodic linear model can lower the uncertainties of the prediction accounting for site-effects. Moreover, the analysis of the station correction terms is important as itself because they can be used to evaluate the quality of the stations in terms of site-amplification. An important result of this technique is that the decreasing of the uncertainties in the predictions can lead to a decreasing in both false and missed alarms for a single station onsite EEW system.

In the second work, we compared the performances of 24 different models (compare 12 linear LSR, and 12 non-linear ML regressors) for the prediction of structural drift. We measured a total of 9 P-wave features on waveforms recorded from sensors in Japanese and US buildings. We proved that the complexity of the dataset plays an important role in the prediction uncertainties. Hence, we showed that non-linear machine learning models perform better than linear models. The residual analysis showed that our predictions suffer of under-estimation for events with  $M > 7.5$ , this is probably due to the 3s window that is too small to account for the entire rupture duration of these events. While this can seem limiting, it is important to note that many countries (e.g., Italy, Greece, and Turkey) suffer from destructive seismicity with lower magnitude and they would benefit also from these kinds of models. In the end, we tried to export the Japanese models to the US buildings finding that the predictions are obtained with a bias that can be overcome only introducing magnitude information.

In the last work, we proposed a method to detect the preparatory phase of induced earthquakes in The Geysers, California. We used 9 features related to the physics and the behaviour of the seismicity as input for two RNNs, one to highlight the pre-event phase, the other for the post-event phase. Indeed, we showed that, while the aftershocks are easier to detect, the model for the preparatory phase tend to alert also for the aftershocks. Despite that, when we combined the two RNNs the resultant model is able to highlight a change in the seismicity from hours to days before the main event, suggesting the presence of a preparatory phase for induced seismicity at The Geysers.

The work presented in these thesis shows some important pathways for onsite EEW. The first is the possibility to include parameters of engineering interest in order to make the methods more suitable for direct application.

Another important message that comes out from our analysis is the importance to account for site-effects. As matter of fact, the site-effect are usually not considered or considered as ineffective for EEW laws. This opinion is based on the fact we can consider the P-wave and the S-wave as affected by the same site-effect and so there should not be any effect on the scaling laws between P and S parameters. Nonetheless, we showed not only that this effect is present, but also that when we consider it, we improve the results of our methods.

In general, we demonstrated as the ergodicity of the datasets are often overrated. In the second work, we proved that the complexity of the dataset in terms of buildings and classes of buildings plays an important role in the performances of the methods. This means that the more data we will have in the future the more we must be careful into putting all of them as input for ergodic models, while we should prefer more

## 5. Conclusions

specific model (e.g., single building, single region, etc..) or non-ergodic model as the mixed-effect regression.

Furthermore, the machine learning techniques represent a powerful instrument able to improve the models and to manage the huge amount of data that we will have in the next future.

So, next steps of my research will be to find new and more ambitious ways to use the gained knowledge in EEW field and beyond. As example, we could try to include our EEW systems for building into a Big Data framework or towards an operational system implemented on the Internet of Things. Moreover, we could apply feature-based machine learning regressors to more complex problem, such as magnitude estimation or earthquake location for onsite EEW. Furthermore, another interesting challenge would be to upgrade the work on the preparatory phase towards the short-term earthquake forecasting.

## 6. References

- Abercrombie, R. E., and J. Mori, 1996, Occurrence patterns of foreshocks to large earthquakes in the western United States, *Nature*, 381, no. 6580, 303–307, doi: 10.1038/381303a0.
- Aki, K., 1981, A probabilistic synthesis of precursory phenomena., *Earthq. Predict. an Int. Rev.*, 566–574, doi: 10.1029/me004p0566.
- Aki, K., 1965, Maximum likelihood estimate of b in the Gutenberg-Richter formula and its confidence limits, *Bull. Earthq. Res. Inst.*, 43, 237–239.
- Allen, R. M., and H. Kanamori, 2003, The potential for earthquake early warning in Southern California, *Science (80-. )*, 300, no. 5620, 786–789, doi: 10.1126/science.1080912.
- Allen, R., Q. Kong, and R. Martin-Short, 2019, The MyShake Platform: A Global Vision for Earthquake Early Warning, *Pure Appl. Geophys.*, doi: 10.1007/s00024-019-02337-7.
- Allen, R. M., and D. Melgar, 2019, Earthquake early warning: Advances, scientific challenges, and societal needs, *Annual Reviews Inc.*, 361–388.
- Altman, N. S., 1992, An introduction to kernel and nearest-neighbor nonparametric regression, *Am. Stat.*, doi: 10.1080/00031305.1992.10475879.
- Amitrano, D., 2003, Brittle-ductile transition and associated seismicity: Experimental and numerical studies and relationship with the b value , *J. Geophys. Res. Solid Earth*, 108, no. B1, doi: 10.1029/2001jb000680.
- Anderson, J. G., and J. N. Brune, 1999, Probabilistic seismic hazard analysis without the ergodic assumption, *Seismol. Res. Lett.*, 70, no. 1, 19–28, doi: 10.1785/gssrl.70.1.19.
- Astorga, A., P. Guéguen, S. Ghimire, and T. Kashima, 2020, NDE1.0: a new database of earthquake data recordings from buildings for engineering applications, *Bull. Earthq. Eng.*, doi: 10.1007/s10518-019-00746-6.
- Astorga, A., P. Guéguen, and T. Kashima, 2018, Nonlinear elasticity observed in buildings during a long sequence of earthquakes, *Bull. Seismol. Soc. Am.*, doi: 10.1785/0120170289.
- Astorga, A. L., P. Guéguen, J. Rivière, T. Kashima, and P. A. Johnson, 2019, Recovery of the resonance frequency of buildings following strong seismic deformation as a proxy for structural health, *Struct. Heal. Monit.*, doi: 10.1177/1475921718820770.
- Al Atik, L., N. Abrahamson, J. J. Bommer, F. Scherbaum, F. Cotton, and N. Kuehn, 2010, The variability of ground-motion prediction models and its components, *Seismol. Res. Lett.*, 81, no. 5, 794–801, doi: 10.1785/gssrl.81.5.794.
- Bates, D., M. Mächler, B. M. Bolker, and S. C. Walker, 2015, Fitting linear mixed-effects models using lme4, *J. Stat. Softw.*, 67, no. 1, doi: 10.18637/jss.v067.i01.
- Bindi, D., L. Luzi, F. Pacor, and R. Paolucci, 2011, Identification of accelerometric stations in ITACA with distinctive features in their seismic response, *Bull. Earthq. Eng.*, 9, no. 6, 1921–1939, doi: 10.1007/s10518-011-9271-5.
- Bito, Y., and Y. Nakamura, 1986, URGENT EARTHQUAKE DETECTION AND ALARM SYSTEM., *Civ. Eng. Japan*.
- Bolton, D. C., C. Marone, P. Shokouhi, J. Rivière, B. Rouet-Leduc, C. Hulbert, and P. A. Johnson, 2019, Characterizing acoustic signals and searching for precursors during the laboratory seismic cycle using unsupervised machine learning, *Seismological Society of America*, 1088–1098.

## 6. References

- Böse, M., E. Hauksson, K. Solanki, H. Kanamori, and T. H. Heaton, 2009, Real-time testing of the on-site warning algorithm in southern California and its performance during the July 29 2008 Mw5.4 Chino Hills earthquake, *Geophys. Res. Lett.*, 36, no. 5, doi: 10.1029/2008GL036366.
- Böse, M., T. Heaton, and E. Hauksson, 2012, Rapid estimation of earthquake source and ground-motion parameters for earthquake early warning using data from a single three- component broadband or strong-motion sensor, *Bull. Seismol. Soc. Am.*, doi: 10.1785/0120110152.
- Böse, Maren, T. H. Heaton, and E. Hauksson, 2012, Real-time Finite Fault Rupture Detector (FinDer) for large earthquakes, *Geophys. J. Int.*, 191, no. 2, 803–812, doi: 10.1111/j.1365-246X.2012.05657.x.
- Böse, M., D. E. Smith, C. Felizardo, M. A. Meier, T. H. Heaton, and J. F. Clinton, 2018, FinDer v.2: Improved real-time ground-motion predictions for M2-M9 with seismic finite-source characterization, *Geophys. J. Int.*, 212, no. 1, 725–742, doi: 10.1093/gji/ggx430.
- Bouchon, M., V. Durand, D. Marsan, H. Karabulut, and J. Schmittbuhl, 2013, The long precursory phase of most large interplate earthquakes, *Nat. Geosci.*, 6, no. 4, 299–302, doi: 10.1038/ngeo1770.
- Breiman, L., 2001, Random forests, *Mach. Learn.*, doi: 10.1023/A:1010933404324.
- Bressan, G., C. Barnaba, S. Gentili, and G. Rossi, 2017, Information entropy of earthquake populations in northeastern Italy and western Slovenia, *Phys. Earth Planet. Inter.*, 271, 29–46, doi: 10.1016/j.pepi.2017.08.001.
- Brondi, P., M. Picozzi, A. Emolo, A. Zollo, and M. Mucciarelli, 2015, Predicting the macroseismic intensity from early radiated P wave energy for on-site earthquake early warning in Italy, *J. Geophys. Res. Solid Earth*, doi: 10.1002/2015JB012367.
- Caruso, A., S. Colombelli, L. Elia, M. Picozzi, and A. Zollo, 2017, An on-site alert level early warning system for Italy, *J. Geophys. Res. Solid Earth*, 122, no. 3, 2106–2118, doi: 10.1002/2016JB013403.
- Chan, R. W. K., Y. S. Lin, and H. Tagawa, 2019, A smart mechatronic base isolation system using earthquake early warning, *Soil Dyn. Earthq. Eng.*, doi: 10.1016/j.soildyn.2019.01.019.
- Cheng, M. H., S. Wu, T. H. Heaton, and J. L. Beck, 2014, Earthquake early warning application to buildings, *Eng. Struct.*, 60, 155–164, doi: 10.1016/J.ENGSTRUCT.2013.12.033.
- Chicco, D., and G. Jurman, 2020, The advantages of the Matthews correlation coefficient (MCC) over F1 score and accuracy in binary classification evaluation, *BMC Genomics*, 21, no. 1, doi: 10.1186/s12864-019-6413-7.
- Cho, K., B. Van Merriënboer, C. Gulcehre, D. Bahdanau, F. Bougares, H. Schwenk, and Y. Bengio, 2014, Learning phrase representations using RNN encoder-decoder for statistical machine translation, in *EMNLP 2014 - 2014 Conference on Empirical Methods in Natural Language Processing, Proceedings of the Conference*, Association for Computational Linguistics (ACL), 1724–1734.
- Chung, A. I., M. A. Meier, J. Andrews, M. Böse, B. W. Crowell, J. J. McGuire, and D. E. Smith, 2020, Shakealert earthquake early warning system performance during the 2019 ridgecrest earthquake sequence, *Bull. Seismol. Soc. Am.*, doi: 10.1785/0120200032.
- Colombelli, S., R. M. Allen, and A. Zollo, 2013, Application of real-time GPS to earthquake early warning in subduction and strike-slip environments, *J. Geophys. Res. Solid Earth*, doi: 10.1002/jgrb.50242.
- Colombelli, S., F. Carotenuto, L. Elia, and A. Zollo, 2020, Design and implementation of a mobile device app for network-based earthquake early warning systems (EEWSs): application to the PRESTo EEWS in southern Italy, *Nat. Hazards Earth Syst. Sci.*, 20, 921–931, doi: 10.5194/nhess-20-921-2020.
- Colombelli, S., A. Caruso, A. Zollo, G. Festa, and H. Kanamori, 2015, A P wave-based, on-site method for earthquake early warning, *Geophys. Res. Lett.*, 42, no. 5, 1390–1398, doi: 10.1002/2014GL063002.

## 6. References

- Colombelli, S., and A. Zollo, 2015, Fast determination of earthquake magnitude and fault extent from real-time P-wave recordings, *Geophys. J. Int.*, 202, no. 2, 1158–1163, doi: 10.1093/gji/ggv217.
- Convertito, V., I. Iervolino, A. Zollo, and G. Manfredi, 2008, Prediction of response spectra via real-time earthquake measurements, *Soil Dyn. Earthq. Eng.*, 28, no. 6, 492–505, doi: 10.1016/j.soildyn.2007.07.006.
- Cooper, J. D., 1868, Earthquake indicator.
- Corbi, F., F. Funicello, S. Brizzi, L. Sandri, J. Bedford, M. Rosenau, and S. Lallemand, 2019, Machine Learning Can Predict the Timing and Size of Analog Earthquakes, *Geophys. Res. Lett.*, 46, no. 3, doi: 10.1029/2018GL081251.
- Cornell, C. A., and H. Krawinkler, 2000, Progress and challenges in seismic performance assessment. PEER Center News 3, Univ. California, Berkeley.
- Cortes, C., and V. Vapnik, 1995, Support-vector networks, *Mach. Learn.*, doi: 10.1007/bf00994018.
- Cremen, G., and C. Galasso, 2021, A decision-making methodology for risk-informed earthquake early warning, *Comput. Civ. Infrastruct. Eng.*, 36, no. 6, 747–761, doi: 10.1111/MICE.12670.
- Crowell, B. W. et al., 2016, Demonstration of the Cascadia G-FAST Geodetic Earthquake Early Warning System for the Nisqually, Washington, *Earthquake, Seismol. Res. Lett.*, 87, no. 4, 930–943, doi: 10.1785/0220150255.
- Crowell, B. W., Y. Bock, and M. B. Squibb, 2009, Demonstration of earthquake early warning using total displacement waveforms from real-time gps networks, *Seismol. Res. Lett.*, 80, no. 5, 772–782, doi: 10.1785/gssrl.80.5.772.
- D'Errico, L., F. Franchi, F. Graziosi, A. Marotta, C. Rinaldi, M. Boschi, and A. Colarieti, 2019, Structural health monitoring and earthquake early warning on 5g urllc network, in *IEEE 5th World Forum on Internet of Things, WF-IoT 2019 - Conference Proceedings*.
- Das, S., and C. H. Scholz, 1981, Theory of time-dependent rupture in the Earth., *J. Geophys. Res.*, 86, no. B7, 6039–6051, doi: 10.1029/JB086iB07p06039.
- DeVries, P. M. R., F. Viégas, M. Wattenberg, and B. J. Meade, 2018, Deep learning of aftershock patterns following large earthquakes, *Nature*, 560, no. 7720, 632–634, doi: 10.1038/s41586-018-0438-y.
- Dieterich, J. H., 1978, Preseismic fault slip and earthquake prediction, *J. Geophys. Res.*, 83, no. B8, 3940, doi: 10.1029/jb083ib08p03940.
- Dietterich, T., 1995, Overfitting and Undercomputing in Machine Learning, *Comput. Surv.*, 27, 326–327.
- Dodge, D. A., G. C. Beroza, and W. L. Ellsworth, 1996, Detailed observations of California foreshock sequences: Implications for the earthquake initiation process, *J. Geophys. Res. Solid Earth*, 101, no. B10, 22371–22392, doi: 10.1029/96jb02269.
- Dresen, G., G. Kwiatek, T. Goebel, and Y. Ben-Zion, 2020, Seismic and Aseismic Preparatory Processes Before Large Stick–Slip Failure, *Pure Appl. Geophys.*, 177, no. 12, 5741–5760, doi: 10.1007/s00024-020-02605-x.
- Durand, V., S. Bentz, G. Kwiatek, G. Dresen, C. Wollin, O. Heidbach, P. Martínez-Garzòn, F. Cotton, M. Nurlu, and M. Bohnhoff, 2020, A two-scale preparation phase preceded an Mw 5.8 earthquake in the Sea of Marmara Offshore Istanbul, Turkey, *Seismol. Res. Lett.*, 91, no. 6, 3139–3147, doi: 10.1785/0220200110.
- Efron, B., 2007, Bootstrap Methods: Another Look at the Jackknife, *Ann. Stat.*, 7, no. 1, doi: 10.1214/aos/1176344552.

## 6. References

- Elenas, A., 2000, Correlation between seismic acceleration parameters and overall structural damage indices of buildings, *Soil Dyn. Earthq. Eng.*, 20, nos. 1–4, 93–100, doi: 10.1016/S0267-7261(00)00041-5.
- Elenas, A., and K. Meskouris, 2001, Correlation study between seismic acceleration parameters and damage indices of structures, *Eng. Struct.*, doi: 10.1016/S0141-0296(00)00074-2.
- Ellsworth, W. L., and F. Bulut, 2018, Nucleation of the 1999 Izmit earthquake by a triggered cascade of foreshocks, *Nat. Geosci.*, 11, no. 7, 531–535, doi: 10.1038/s41561-018-0145-1.
- Espinosa-Aranda, J. M., A. Cuellar, A. Garcia, G. Ibarrola, R. Islas, S. Maldonado, and F. H. Rodriguez, 2009, Evolution of the Mexican seismic alert system (SASMEX), *Seismol. Res. Lett.*, doi: 10.1785/gssrl.80.5.694.
- European Committee for Standardization, 2004, Eurocode 8: Design of structures for earthquake resistance - Part 1 : General rules, seismic actions and rules for buildings, *Eur. Comm. Stand.*, 1, no. English, 231.
- Felzer, K. R., R. E. Abercrombie, and G. Ekström, 2004, A common origin for aftershocks, foreshocks, and multiplets, *Bull. Seismol. Soc. Am.*, 94, no. 1, 88–98, doi: 10.1785/0120030069.
- Fleming, K. et al., 2009, The self-organizing seismic early warning information network (SOSEWIN), *Seismol. Res. Lett.*, doi: 10.1785/gssrl.80.5.755.
- Friedman, J. H., 2001, Greedy function approximation: A gradient boosting machine, *Ann. Stat.*, doi: 10.1214/aos/1013203451.
- Gasparini, P., G. Manfredi, and J. Zschau, 2011, Earthquake early warning as a tool for improving society's resilience and crisis response, *Soil Dyn. Earthq. Eng.*, doi: 10.1016/j.soildyn.2010.09.004.
- van de Geer, J. P., 1995, Some Aspects of Minkowski Distance, Leiden University, Department of Data Theory, Department of Data Theory, University of Leiden: Esearch report.
- Ghimire, S., P. Guéguen, and A. Astorga, 2021, Analysis of the efficiency of intensity measures from real earthquake data recorded in buildings, *Soil Dyn. Earthq. Eng.*, 106751, doi: 10.1016/j.soildyn.2021.106751.
- Goebel, T. H. W., T. W. Becker, D. Schorlemmer, S. Stanchits, C. Sammis, E. Rybacki, and G. Dresen, 2012, Identifying fault heterogeneity through mapping spatial anomalies in acoustic emission statistics, *J. Geophys. Res. Solid Earth*, 117, no. 3, doi: 10.1029/2011JB008763.
- Goebel, T. H. W., G. Kwiatek, T. W. Becker, E. E. Brodsky, and G. Dresen, 2017, What allows seismic events to grow big?: Insights from b-value and fault roughness analysis in laboratory stick-slip experiments, *Geology*, 45, no. 9, 815–818, doi: 10.1130/G39147.1.
- Goebel, T. H. W., D. Schorlemmer, T. W. Becker, G. Dresen, and C. G. Sammis, 2013, Acoustic emissions document stress changes over many seismic cycles in stick-slip experiments, *Geophys. Res. Lett.*, 40, no. 10, 2049–2054, doi: 10.1002/grl.50507.
- González, J., W. Yu, and L. Telesca, 2019, Earthquake Magnitude Prediction Using Recurrent Neural Networks, *Proceedings*, 24, no. 1, 22, doi: 10.3390/iecg2019-06213.
- Gorini, A., M. Nicoletti, P. Marsan, R. Bianconi, R. De Nardis, L. Filippi, S. Marcucci, F. Palma, and E. Zambonelli, 2010, The Italian strong motion network, *Bull. Earthq. Eng.*, 8, no. 5, 1075–1090, doi: 10.1007/s10518-009-9141-6.
- Grapenthin, R., I. A. Johanson, and R. M. Allen, 2014, Operational real-time GPS-enhanced earthquake early warning, *J. Geophys. Res. Solid Earth*, 119, no. 10, 7944–7965, doi: 10.1002/2014JB011400.
- Grassberger, P., and I. Procaccia, 1983, Characterization of strange attractors, *Phys. Rev. Lett.*, 50, no. 5, 346–349, doi: 10.1103/PhysRevLett.50.346.

## 6. References

- Grassberger, P., and I. Procaccia, 2004, Measuring the Strangeness of Strange Attractors, in *The Theory of Chaotic Attractors*, Springer New York, 170–189.
- Grasso, V. F., 2005, Seismic Early Warning Systems: Procedure for Automated Decision Making, Università di Napoli Federico II.
- Guéguen, P., L. F. Bonilla, and J. Douglas, 2019, Comparison of soil nonlinearity (in situ stress-strain relation and G/G max Reduction) observed in strong-motion databases and modeled in ground-motion prediction equations, *Bull. Seismol. Soc. Am.*, 109, no. 1, 178–186, doi: 10.1785/0120180169.
- Guéguen, P., P. Johnson, and P. Roux, 2016, Nonlinear dynamics induced in a structure by seismic and environmental loading, *J. Acoust. Soc. Am.*, doi: 10.1121/1.4958990.
- Gulia, L., and S. Wiemer, 2019, Real-time discrimination of earthquake foreshocks and aftershocks, *Nature*, 574, no. 7777, 193–199, doi: 10.1038/s41586-019-1606-4.
- Gupta, A. K., 1993, Response Spectrum Method in seismic analysis and design of structures, *Bull. New Zeal. Soc. Earthq. Eng.*, 26, no. 3, 369, doi: 10.5459/bnzsee.26.3.369.
- Gutenberg, B., and C. F. Richter, 1942, Earthquake magnitude, intensity, energy, and acceleration\*, *Bull. Seismol. Soc. Am.*, 32, no. 3, 163–191, doi: 10.1785/BSSA0320030163.
- Gutenberg, B., and C. F. Richter, 1956, Earthquake magnitude, intensity, energy, and acceleration, *Bull. Seismol. Soc. Am.*, 46, no. 2, 105–145, doi: 10.1785/BSSA0460020105.
- Hanks, T. C., and H. Kanamori, 1979, A moment magnitude scale, in *Journal of Geophysical Research B: Solid Earth*, 2348–2350.
- Hauksson, E., J. Stock, K. Hutton, W. Yang, J. A. Vidal-Villegas, and H. Kanamori, 2011, The 2010 Mw 7.2 El mayor-cucapah earthquake sequence, Baja California, Mexico and Southernmost California, USA: Active seismotectonics along the Mexican pacific margin, *Pure Appl. Geophys.*, 168, nos. 8–9, 1255–1277, doi: 10.1007/s00024-010-0209-7.
- Hawkins, D. M., 2004, The Problem of Overfitting.
- Helmstetter, A., and D. Sornette, 2003, Foreshocks explained by cascades of triggered seismicity, *J. Geophys. Res. Solid Earth*, 108, no. B10, doi: 10.1029/2003jb002409.
- Henderson, J. R., D. J. Barton, and G. R. Foulger, 1999, Fractal clustering of induced seismicity in The Geysers geothermal area, California, *Geophys. J. Int.*, 139, no. 2, 317–324, doi: 10.1046/j.1365-246X.1999.00939.x.
- Henderson, J., and I. Main, 1992, A simple fracture-mechanical model for the evolution of seismicity, *Geophys. Res. Lett.*, 19, no. 4, 365–368, doi: 10.1029/92GL00274.
- Hochreiter, S., 1998, The vanishing gradient problem during learning recurrent neural nets and problem solutions, *Int. J. Uncertainty, Fuzziness Knowledge-Based Syst.*, 6, no. 2, 107–116, doi: 10.1142/S0218488598000094.
- Hochreiter, S., and J. Schmidhuber, 1997, Long Short-Term Memory, *Neural Comput.*, 9, no. 8, 1735–1780, doi: 10.1162/neco.1997.9.8.1735.
- Hoshiya, M., 2013, Real-time prediction of ground motion by Kirchhoff-Fresnel boundary integral equation method: Extended front detection method for Earthquake Early Warning, *J. Geophys. Res. Solid Earth*, 118, no. 3, 1038–1050, doi: 10.1002/jgrb.50119.
- Hoshiya, M., and S. Aoki, 2015, Numerical shake prediction for earthquake early warning: Data assimilation, real-time shake mapping, and simulation of wave propagation, *Bull. Seismol. Soc. Am.*, 105, no. 3, 1324–1338, doi: 10.1785/0120140280.

## 6. References

- Hoshiba, M., K. Iwakiri, N. Hayashimoto, T. Shimoyama, K. Hirano, Y. Yamada, Y. Ishigaki, and H. Kikuta, 2011, Outline of the 2011 off the pacific coast of tohoku earthquake (M w 9.0) -earthquake early warning and observed seismic intensity, *Earth, Planets Sp.*, 63, no. 7, 547–551, doi: 10.5047/eps.2011.05.031.
- Hoshiba, M., O. Kamigaichi, M. Saito, S. Tsukada, and N. Hamada, 2008, Earthquake early warning starts nationwide in Japan, *Eos (Washington. DC.)*, 89, no. 8, 73–74, doi: 10.1029/2008EO080001.
- Hoshiba, M., and T. Ozaki, 2014, Earthquake Early Warning and Tsunami Warning of the Japan Meteorological Agency, and Their Performance in the 2011 off the Pacific Coast of Tohoku Earthquake (  $M_{\text{w}}$  9.0), Springer, Berlin, Heidelberg, 1–28.
- Hsu, T. Y., S. K. Huang, Y. W. Chang, C. H. Kuo, C. M. Lin, T. M. Chang, K. L. Wen, and C. H. Loh, 2013, Rapid on-site peak ground acceleration estimation based on support vector regression and P-wave features in Taiwan, *Soil Dyn. Earthq. Eng.*, doi: 10.1016/j.soildyn.2013.03.001.
- Iaccarino, A. G., P. Gueguen, M. Picozzi, and S. Ghimire, 2021, Earthquake Early Warning System for Structural Drift Prediction Using Machine Learning and Linear Regressors, *Front. Earth Sci.*, 9, doi: 10.3389/FEART.2021.666444.
- Iaccarino, A. G., M. Picozzi, D. Bindi, and D. Spallarossa, 2020, Onsite earthquake early warning: Predictive models for acceleration response spectra considering site effects, *Bull. Seismol. Soc. Am.*, 110, no. 3, 1289–1304, doi: 10.1785/0120190272.
- Iervolino, I., 2011, Performance-based earthquake early warning, *Soil Dyn. Earthq. Eng.*, 31, no. 2, 209–222, doi: 10.1016/J.SOILDYN.2010.07.010.
- Iervolino, I., V. Convertito, M. Giorgio, G. Manfredi, and A. Zollo, 2006, Real-time risk analysis for hybrid earthquake early warning systems, *J. Earthq. Eng.*, 10, no. 6, 867–885, doi: 10.1142/S1363246906002955.
- Iervolino, I., G. Manfredi, and E. Cosenza, 2007, Earthquake Early Warning and Engineering Application Prospects, *Earthq. Early Warn. Syst.*, 233–247, doi: 10.1007/978-3-540-72241-0\_12.
- Johnson, P. A. et al., 2021, Laboratory earthquake forecasting: A machine learning competition, *National Academy of Sciences*, 2011362118.
- Jones, L. M., 1985, Foreshocks and time-dependent earthquake hazard assessment in southern California, *Bull. Seismol. Soc. Am.*, 75, no. 6, 1669–1679.
- Jones, L. M., and P. Molnar, 1979, Some characteristics of foreshocks and their possible relationship to earthquake prediction and premonitory slip on faults., *J. Geophys. Res.*, 84, no. B7, 3596–3608, doi: 10.1029/JB084iB07p03596.
- Jozinović, D., A. Lomax, I. Štajduhar, and A. Michelini, 2020, Rapid prediction of earthquake ground shaking intensity using raw waveform data and a convolutional neural network, *Geophys. J. Int.*, 222, no. 2, 1379–1389, doi: 10.1093/gji/ggaa233.
- Kanamori, H., 2005, Real-time seismology and earthquake damage mitigation, *Annu. Rev. Earth Planet. Sci.*, 33, 195–214, doi: 10.1146/annurev.earth.33.092203.122626.
- Kanamori, H., 1981, The Nature of Seismicity Patterns Before Large Earthquakes, in *Earthquake prediction: an international review*, American Geophysical Union, Maurice Ewing Series 4, 1–19.
- Kanamori, H., J. Mori, E. Hauksson, T. H. Heaton, L. K. Hutton, and L. M. Jones, 1993, Determination of earthquake energy release and ML using TERRAscope, *Bull. - Seismol. Soc. Am.*, 83, no. 2, 330–346.
- Kato, A., and Y. Ben-Zion, 2021, The generation of large earthquakes, *Nat. Rev. Earth Environ.*, 2, no. 1, 26–39, doi: 10.1038/s43017-020-00108-w.

## 6. References

- Kato, A., K. Obara, T. Igarashi, H. Tsuruoka, S. Nakagawa, and N. Hirata, 2012, Propagation of slow slip leading up to the 2011 Mw 9.0 Tohoku-Oki earthquake, *Science* (80-. ), 335, no. 6069, 705–708, doi: 10.1126/science.1215141.
- King, C. Y., 1983, Earthquake prediction: Electromagnetic emissions before earthquakes, 377.
- Kodera, Y., Y. Yamada, K. Hirano, K. Tamaribuchi, S. Adachi, N. Hayashimoto, M. Morimoto, M. Nakamura, and M. Hoshihara, 2018, The propagation of local undamped motion (PLUM) method: A simple and robust seismic wavefield estimation approach for earthquake early warning, *Bull. Seismol. Soc. Am.*, 108, no. 2, 983–1003, doi: 10.1785/0120170085.
- Kong, Q., R. M. Allen, L. Schreier, and Y.-W. Kwon, 2016, MyShake: A smartphone seismic network for earthquake early warning and beyond, *Sci. Adv.*, 2, no. 2, e1501055, doi: 10.1126/sciadv.1501055.
- Kong, Q., D. Trugman, Z. Ross, M. Bianco, P. Gerstoft, and B. Meade, 2019, Machine learning in seismology: Turning data into insights, *Seismol. Res. Lett.*, 90, no. 1, doi: 10.1785/0220180259.
- Konno, K., and T. Ohmachi, 1998, Ground-motion characteristics estimated from spectral ratio between horizontal and vertical components of microtremor, *Bull. Seismol. Soc. Am.*, 88, no. 1, 228–241.
- Kotha, S. R., F. Cotton, and D. Bindi, 2018, A new approach to site classification: Mixed-effects Ground Motion Prediction Equation with spectral clustering of site amplification functions, *Soil Dyn. Earthq. Eng.*, 110, 318–329, doi: 10.1016/j.soildyn.2018.01.051.
- Kubo, T., Y. Hisada, M. Murakami, F. Kosuge, and K. Hamano, 2011, Application of an earthquake early warning system and a real-time strong motion monitoring system in emergency response in a high-rise building, *Soil Dyn. Earthq. Eng.*, doi: 10.1016/j.soildyn.2010.07.009.
- Kuyuk, H. S., and R. M. Allen, 2013, Optimal seismic network density for earthquake early warning: A case study from California, *Seismol. Res. Lett.*, 84, no. 6, 946–954, doi: 10.1785/0220130043.
- Kwiatek, G., T. H. W. Goebel, and G. Dresen, 2014, Seismic moment tensor and b value variations over successive seismic cycles in laboratory stick-slip experiments, *Geophys. Res. Lett.*, 41, no. 16, 5838–5846, doi: 10.1002/2014GL060159.
- Kwiatek, G., P. Martínez-Garzón, G. Dresen, M. Bohnhoff, H. Sone, and C. Hartline, 2015, Effects of long-term fluid injection on induced seismicity parameters and maximum magnitude in northwestern part of the Geysers geothermal field, *J. Geophys. Res. Solid Earth*, 120, no. 10, 7085–7101, doi: 10.1002/2015JB012362.
- Lancieri, M., and A. Zollo, 2008, A Bayesian approach to the real-time estimation of magnitude from the early *P* and *S* wave displacement peaks, *J. Geophys. Res.*, 113, no. B12, B12302, doi: 10.1029/2007JB005386.
- Lapusta, N., and J. R. Rice, 2003, Nucleation and early seismic propagation of small and large events in a crustal earthquake model, *J. Geophys. Res. Solid Earth*, 108, no. B4, doi: 10.1029/2001jb000793.
- Legrand, D., A. Cisternas, and L. Dorbath, 1996, Multifractal analysis of the 1992 Erzincan Aftershock Sequence, *Geophys. Res. Lett.*, 23, no. 9, 933–936, doi: 10.1029/96GL00725.
- Lin, Y. S., R. W. K. Chan, and H. Tagawa, 2020, Earthquake early warning-enabled smart base isolation system, *Autom. Constr.*, doi: 10.1016/j.autcon.2020.103203.
- Lloyd, S. P., 1982, Least Squares Quantization in PCM, *IEEE Trans. Inf. Theory*, 28, no. 2, 129–137, doi: 10.1109/TIT.1982.1056489.
- Lomax, A., C. Satriano, and M. Vassallo, 2012, Automatic picker developments and optimization: Filterpicker-A robust, broadband picker for real-time seismic monitoring and earthquake early warning, *Seismol. Res. Lett.*, 83, no. 3, 531–540, doi: 10.1785/gssrl.83.3.531.

## 6. References

- Luco, N., 2002, Probabilistic seismic demand analysis, SMRF connection fractures, and near-source effects, Stanford University.
- Luzi, L. et al., 2017, The central Italy seismic sequence between August and December 2016: Analysis of strong-motion observations, *Seismol. Res. Lett.*, 88, no. 5, 1219–1231, doi: 10.1785/0220170037.
- Luzi, L., D. Bindi, G. Franceschina, F. Pacor, and R. R. Castro, 2005, Geotechnical site characterisation in the Umbria-Marche area and evaluation of earthquake site-response, *Pure Appl. Geophys.*, 162, no. 11, 2133–2161, doi: 10.1007/s00024-005-2707-6.
- Luzi, L., S. Hailemichael, D. Bindi, F. Pacor, F. Mele, and F. Sabetta, 2008, ITACA (Italian ACcelerometric Archive) : A web portal for the dissemination of Italian strong-motion data, *Seismol. Res. Lett.*, 79, no. 5, 716–722, doi: 10.1785/gssrl.79.5.716.
- Luzi, L., R. Puglia, F. Pacor, M. R. Gallipoli, D. Bindi, and M. Mucciarelli, 2011, Proposal for a soil classification based on parameters alternative or complementary to  $V_s$ , *Bull. Earthq. Eng.*, 9, no. 6, 1877–1898, doi: 10.1007/s10518-011-9274-2.
- Main, I. G., 1992, Damage mechanics with long-range interactions: correlation between the seismic b-value and the fractal two-point correlation dimension, *Geophys. J. Int.*, 111, no. 3, 531–541, doi: 10.1111/j.1365-246X.1992.tb02110.x.
- Malin, P. E. et al., 2018, Microearthquakes preceding a M4.2 Earthquake Offshore Istanbul, *Sci. Rep.*, 8, no. 1, doi: 10.1038/s41598-018-34563-9.
- Martínez-Garzón, P., G. Kwiatek, H. Sone, M. Bohnhoff, G. Dresen, and C. Hartline, 2014, Spatiotemporal changes, faulting regimes, and source parameters of induced seismicity: A case study from the Geysers geothermal field, *J. Geophys. Res. Solid Earth*, 119, no. 11, 8378–8396, doi: 10.1002/2014JB011385.
- Marzocchi, W., I. Spassiani, A. Stallone, and M. Taroni, 2020, How to be fooled searching for significant variations of the b-value, *Geophys. J. Int.*, 220, no. 3, 1845–1856, doi: 10.1093/gji/ggz541.
- Marzorati, S., C. Ladina, E. Falcucci, S. Gori, M. Saroli, G. Ameri, and F. Galadini, 2011, Site effects “on the rock”: The case of Castelvechio Subequo (L’Aquila, central Italy), *Bull. Earthq. Eng.*, 9, no. 3, 841–868, doi: 10.1007/s10518-011-9263-5.
- Matthews, B. W., 1975, Comparison of the predicted and observed secondary structure of T4 phage lysozyme, *BBA - Protein Struct.*, 405, no. 2, 442–451, doi: 10.1016/0005-2795(75)90109-9.
- Meier, M. A., 2017, How “good” are real-time ground motion predictions from Earthquake Early Warning systems?, *J. Geophys. Res. Solid Earth*, 122, no. 7, 5561–5577, doi: 10.1002/2017JB014025.
- Mignan, A., 2012, Functional shape of the earthquake frequency-magnitude distribution and completeness magnitude, *J. Geophys. Res. Solid Earth*, 117, no. 8, doi: 10.1029/2012JB009347.
- Mignan, A., 2014, The debate on the prognostic value of earthquake foreshocks: A meta-analysis, *Sci. Rep.*, 4, doi: 10.1038/srep04099.
- Mignan, A., and M. Broccardo, 2020, Neural network applications in earthquake prediction (1994-2019): Meta-analytic and statistical insights on their limitations, *Seismol. Res. Lett.*, 91, no. 4, 2330–2342, doi: 10.1785/0220200021.
- Mignan, A., and M. Broccardo, 2019, One neuron versus deep learning in aftershock prediction.
- Minson, S. E., A. S. Baltay, E. S. Cochran, T. C. Hanks, M. T. Page, S. K. McBride, K. R. Milner, and M. A. Meier, 2019, The Limits of Earthquake Early Warning Accuracy and Best Alerting Strategy, *Sci. Rep.*, 9, no. 1, doi: 10.1038/s41598-019-39384-y.
- Minson, S. E., M. A. Meier, A. S. Baltay, T. C. Hanks, and E. S. Cochran, 2018, The limits of earthquake early

## 6. References

- warning: Timeliness of ground motion estimates, *Sci. Adv.*, 4, no. 3, doi: 10.1126/sciadv.aag0504.
- Minson, S. E., J. R. Murray, J. O. Langbein, and J. S. Gombert, 2014, Real-time inversions for finite fault slip models and rupture geometry based on high-rate GPS data, *J. Geophys. Res. Solid Earth*, 119, no. 4, 3201–3231, doi: 10.1002/2013JB010622.
- Mousavi, S. M., and G. C. Beroza, 2020a, A Machine-Learning Approach for Earthquake Magnitude Estimation, *Geophys. Res. Lett.*, doi: 10.1029/2019GL085976.
- Mousavi, S. M., and G. C. Beroza, 2020b, Bayesian-Deep-Learning Estimation of Earthquake Location from Single-Station Observations, *IEEE Trans. Geosci. Remote Sens.*, doi: 10.1109/TGRS.2020.2988770.
- Mucciarelli, M., M. R. Gallipoli, C. Lizza, and L. Vignola, 2017, Site condition at accelerometric stations in Southern Italy: observations gained from peculiar cases, *Bull. Earthq. Eng.*, 15, no. 6, 2367–2376, doi: 10.1007/s10518-017-0133-7.
- Münchmeyer, J., D. Bindi, U. Leser, and F. Tilmann, 2021, The transformer earthquake alerting model: a new versatile approach to earthquake early warning, *Geophys. J. Int.*, 225, no. 1, 646–656, doi: 10.1093/gji/ggaa609.
- Murase, K., 2004, A Characteristic Change in Fractal Dimension Prior to the 2003 Tokachi-oki Earthquake ( $M_w=8.0$ ), Hokkaido, Northern Japan, *Earth, Planets Sp.*, 56, no. 3, 401–405, doi: 10.1186/BF03353072.
- Nakamura, Y., and J. Saita, 2007, UrEDAS, the earthquake warning system: Today and tomorrow, in *Earthquake Early Warning Systems*.
- Nazeri, S., Z. Shomali, S. Colombelli, L. Elia, and A. Zollo, 2017, Magnitude estimation based on integrated amplitude and frequency content of the initial p wave in earthquake early warning applied to Tehran, Iran, *Bull. Seismol. Soc. Am.*, 107, no. 3, doi: 10.1785/0120160380.
- Ohnaka, M., 1992, Earthquake source nucleation: A physical model for short-term precursors, *Tectonophysics*, 211, nos. 1–4, 149–178, doi: 10.1016/0040-1951(92)90057-D.
- Ohta, Y. et al., 2012, Quasi real-time fault model estimation for near-field tsunami forecasting based on RTK-GPS analysis: Application to the 2011 Tohoku-Oki earthquake ( $M_w$  9.0), *J. Geophys. Res. Solid Earth*, 117, no. B2, n/a-n/a, doi: 10.1029/2011JB008750.
- Olivieri, M., R. M. Allen, and G. Wurman, 2008, The potential for earthquake early warning in Italy using ElarmS, *Bull. Seismol. Soc. Am.*, 98, no. 1, 495–503, doi: 10.1785/0120070054.
- Pacor, F., R. Paolucci, L. Luzi, F. Sabetta, A. Spinelli, A. Gorini, M. Nicoletti, S. Marcucci, L. Filippi, and M. Dolce, 2011, Overview of the Italian strong motion database ITACA 1.0, *Bull. Earthq. Eng.*, 9, no. 6, 1723–1739, doi: 10.1007/s10518-011-9327-6.
- Panakkat, A., and H. Adeli, 2007, Neural network models for earthquake magnitude prediction using multiple seismicity indicators, *Int. J. Neural Syst.*, 17, no. 1, 13–33, doi: 10.1142/S0129065707000890.
- Paolucci, R., F. Pacor, R. Puglia, G. Ameri, C. Cauzzi, and M. Massa, 2011, Record processing in ITACA, the New Italian strong-motion database, *Geotech. Geol. Earthq. Eng.*, 14, 99–113, doi: 10.1007/978-94-007-0152-6\_8.
- Parolai, S., D. Bindi, T. Boxberger, C. Milkereit, K. Fleming, and M. Pittore, 2015, On-Site early warning and rapid damage forecasting using single stations: Outcomes from the REAKT project, *Seismological Society of America*, 1393–1404.
- Pedregosa, F. et al., 2011, *Scikit-learn: Machine Learning in Python*, Microtome Publishing.
- Peng, H., Z. Wu, Y. M. Wu, S. Yu, D. Zhang, and W. Huang, 2011, Developing a prototype earthquake early warning system in the Beijing capital region, *Seismol. Res. Lett.*, 82, no. 3, 394–403, doi: 10.1785/gssrl.82.3.394.

## 6. References

- Petrovic, B., and S. Parolai, 2016, Joint deconvolution of building and downhole strong-motion recordings: Evidence for the seismic wavefield being radiated back into the shallow geological layers, *Bull. Seismol. Soc. Am.*, 106, no. 4, 1720–1732, doi: 10.1785/0120150326.
- Picozzi, M., 2012, An attempt of real-time structural response assessment by an interferometric approach: A tailor-made earthquake early warning for buildings, *Soil Dyn. Earthq. Eng.*, 38, 109–118, doi: 10.1016/j.soildyn.2012.02.003.
- Picozzi, Matteo, D. Bindi, P. Brondi, D. Di Giacomo, S. Parolai, and A. Zollo, 2017, Rapid determination of P wave-based energy magnitude: Insights on source parameter scaling of the 2016 Central Italy earthquake sequence, *Geophys. Res. Lett.*, 44, no. 9, 4036–4045, doi: 10.1002/2017GL073228.
- Picozzi, M., and A. G. Iaccarino, 2021, Forecasting the Preparatory Phase of Induced Earthquakes by Recurrent Neural Network, *Forecasting*, 3, no. 1, 17–37, doi: 10.3390/forecast3010002.
- Picozzi, M., A. Oth, S. Parolai, D. Bindi, G. De Landro, and O. Amoroso, 2017, Accurate estimation of seismic source parameters of induced seismicity by a combined approach of generalized inversion and genetic algorithm: Application to The Geysers geothermal area, California, *J. Geophys. Res. Solid Earth*, 122, no. 5, 3916–3933, doi: 10.1002/2016JB013690.
- Picozzi, M., S. Parolai, M. Mucciarelli, C. Milkereit, D. Bindi, R. Ditommaso, M. Vona, M. R. Gallipoli, and J. Zschau, 2011, Interferometric analysis of strong ground motion for structural health monitoring: The example of the L'Aquila, Italy, seismic sequence of 2009, *Bull. Seismol. Soc. Am.*, 101, no. 2, 635–651, doi: 10.1785/0120100070.
- Piña-Valdés, J., A. Socquet, F. Cotton, and S. Specht, 2018, Spatiotemporal variations of ground motion in northern Chile before and after the 2014 mw8.1 iquique megathrust event, *Bull. Seismol. Soc. Am.*, 108, no. 2, 801–814, doi: 10.1785/0120170052.
- Pinheiro, J. C., and D. M. Bates, 2000, *Mixed-Effects Models in S and S-Plus: Statistics and Computing*.
- Pitilakis, K., S. Karapetrou, D. Bindi, M. Manakou, B. Petrovic, Z. Roumelioti, T. Boxberger, and S. Parolai, 2016, Structural monitoring and earthquake early warning systems for the AHEPA hospital in Thessaloniki, *Bull. Earthq. Eng.* 2016 149, 14, no. 9, 2543–2563, doi: 10.1007/S10518-016-9916-5.
- Raschka, S., and V. Mirjalili, 2017, *Python Machine Learning: Machine Learning and Deep Learning with Python, scikit-learn, and TensorFlow*.
- Reyes, J., A. Morales-Esteban, and F. Martínez-Álvarez, 2013, Neural networks to predict earthquakes in Chile, *Appl. Soft Comput. J.*, 13, no. 2, 1314–1328, doi: 10.1016/j.asoc.2012.10.014.
- Rikitake, T., 1975, Earthquake precursors, *Bull. Seismol. Soc. Am.*, 65, no. 5, 1133–1162.
- Ross, Z. E., D. T. Trugman, E. Hauksson, and P. M. Shearer, 2019, Searching for hidden earthquakes in Southern California, *Science (80-. )*, doi: 10.1126/science.aaw6888.
- Rouet-Leduc, B., C. Hulbert, N. Lubbers, K. Barros, C. J. Humphreys, and P. A. Johnson, 2017, Machine Learning Predicts Laboratory Earthquakes, *Geophys. Res. Lett.*, 44, no. 18, 9276–9282, doi: 10.1002/2017GL074677.
- Rovelli, A., A. Caserta, F. Marra, and V. Ruggiero, 2002, Can seismic waves be trapped inside an inactive fault zone? The case study of Nocera Umbra, Central Italy, *Bull. Seismol. Soc. Am.*, 92, no. 6, 2217–2232, doi: 10.1785/0120010288.
- De Rubeis, V., P. Dimitriu, E. Papadimitriou, and P. Tosi, 1993, Recurrent patterns in the spatial behaviour of Italian seismicity revealed by the fractal approach, *Geophys. Res. Lett.*, 20, no. 18, 1911–1914, doi: 10.1029/93GL01889.
- Ruhl, C. J., D. Melgar, A. I. Chung, R. Grapenthin, and R. M. Allen, 2019, Quantifying the Value of Real-Time

## 6. References

- Geodetic Constraints for Earthquake Early Warning Using a Global Seismic and Geodetic Data Set, *J. Geophys. Res. Solid Earth*, 124, no. 4, 3819–3837, doi: 10.1029/2018JB016935.
- Ruiz, S. et al., 2017, Nucleation Phase and Dynamic Inversion of the Mw 6.9 Valparaíso 2017 Earthquake in Central Chile, *Geophys. Res. Lett.*, 44, no. 20, 10,290–10,297, doi: 10.1002/2017GL075675.
- Rumelhart, D. E., G. E. Hinton, and R. J. Williams, 1986, Learning representations by back-propagating errors, *Nature*, 323, no. 6088, 533–536, doi: 10.1038/323533a0.
- Sánchez-Reyes, H., D. Essing, E. Beaucé, and P. Poli, 2021, The Imbricated Foreshock and Aftershock Activities of the Balsorano (Italy) Mw 4.4 Normal Fault Earthquake and Implications for Earthquake Initiation, *Seismol. Res. Lett.*, 92, no. 3, 1926–1936, doi: 10.1785/0220200253.
- Satriano, C., L. Elia, C. Martino, M. Lancieri, A. Zollo, and G. Iannaccone, 2011, PRESTo, the earthquake early warning system for Southern Italy: Concepts, capabilities and future perspectives, *Soil Dyn. Earthq. Eng.*, doi: 10.1016/j.soildyn.2010.06.008.
- Satriano, C., A. Lomax, and A. Zollo, 2008, Real-time evolutionary earthquake location for seismic early warning, *Bull. Seismol. Soc. Am.*, 98, no. 3, 1482–1494, doi: 10.1785/0120060159.
- Satriano, C., Y. M. Wu, A. Zollo, and H. Kanamori, 2011, Earthquake early warning: Concepts, methods and physical grounds, *Soil Dyn. Earthq. Eng.*, doi: 10.1016/j.soildyn.2010.07.007.
- Scholz, C. H., 2015, On the stress dependence of the earthquake b value, *Geophys. Res. Lett.*, 42, no. 5, 1399–1402, doi: 10.1002/2014GL062863.
- Shanker, M. S., M. Y. Hu, and M. S. Hung, 1996, Effect of data standardization on neural network training, *Omega*, 24, no. 4, 385–397, doi: 10.1016/0305-0483(96)00010-2.
- Shannon, C. E., 1948, A Mathematical Theory of Communication, *Bell Syst. Tech. J.*, 27, no. 4, 623–656, doi: 10.1002/j.1538-7305.1948.tb00917.x.
- Socquet, A., J. P. Valdes, J. Jara, F. Cotton, A. Walpersdorf, N. Cotte, S. Specht, F. Ortega-Culaciati, D. Carrizo, and E. Norabuena, 2017, An 8 month slow slip event triggers progressive nucleation of the 2014 Chile megathrust, *Geophys. Res. Lett.*, 44, no. 9, 4046–4053, doi: 10.1002/2017GL073023.
- Spallarossa, D., S. R. Kotha, M. Picozzi, S. Barani, and D. Bindi, 2019, On-site earthquake early warning: A partially non-ergodic perspective from the site effects point of view, *Geophys. J. Int.*, 216, no. 2, 919–934, doi: 10.1093/gji/ggy470.
- Srivastava, N., G. Hinton, A. Krizhevsky, I. Sutskever, and R. Salakhutdinov, 2014, Dropout: A simple way to prevent neural networks from overfitting, *J. Mach. Learn. Res.*
- Stafford, P. J., 2014, Crossed and nested mixed-effects approaches for enhanced model development and removal of the ergodic assumption in empirical ground-motion models, *Bull. Seismol. Soc. Am.*, doi: 10.1785/0120130145.
- Stone, M., 1974, Cross-validation and multinomial prediction, *Biometrika*, doi: 10.1093/biomet/61.3.509.
- Strauss, J., and R. Allen, 2016, Benefits and costs of earthquake early warning, *Seismol. Res. Lett.*, 87, no. 3, doi: 10.1785/0220150149.
- Tarantino, S., S. Colombelli, A. Emolo, and A. Zollo, 2019, Quick determination of the earthquake focal mechanism from the azimuthal variation of the initial P-wave amplitude, *Seismol. Res. Lett.*, 90, no. 4, 1642–1649, doi: 10.1785/0220180290.
- Telesca, L., V. Lapenna, and M. Lovallo, 2004, Information entropy analysis of seismicity of Umbria-Marche region (Central Italy), *Nat. Hazards Earth Syst. Sci.*, 4, no. 5/6, 691–695, doi: 10.5194/nhess-4-691-2004.

## 6. References

- Trugman, D. T., I. W. McBrearty, D. C. Bolton, R. A. Guyer, C. Marone, and P. A. Johnson, 2020, The Spatiotemporal Evolution of Granular Microslip Precursors to Laboratory Earthquakes, *Geophys. Res. Lett.*, 47, no. 16, e2020GL088404, doi: 10.1029/2020GL088404.
- Trugman, D. T., and Z. E. Ross, 2019, Pervasive Foreshock Activity Across Southern California, *Geophys. Res. Lett.*, 46, no. 15, 8772–8781, doi: 10.1029/2019GL083725.
- Tubaldi, E., E. Ozer, J. Douglas, and P. Gehl, 2021, Examining the contribution of near real-time data for rapid seismic loss assessment of structures, *Struct. Heal. Monit.*, doi: 10.1177/1475921721996218.
- Viegas, G., and L. Hutchings, 2011, Characterization of induced seismicity near an injection well at the Northwest Geysers Geothermal field, California, in *Transactions - Geothermal Resources Council*, Geothermal Resources Council, 1773–1780.
- Wang, J. P., and Y. M. Wu, 2014, Epistemic uncertainty in on-site earthquake early warning on the use of PGV-PD3 empirical models, *Soil Dyn. Earthq. Eng.*, 65, 126–130, doi: 10.1016/j.soildyn.2014.06.003.
- Weber, E. et al., 2007, An advanced seismic network in the southern Apennines (Italy) for seismicity investigations and experimentation with earthquake early warning, *Seismol. Res. Lett.*, 78, no. 6, 622–634, doi: 10.1785/gssrl.78.6.622.
- Wiemer, S., 2001, A software package to analyze seismicity: ZMAP, *Seismol. Res. Lett.*, 72, no. 3, 373–382, doi: 10.1785/gssrl.72.3.373.
- Woessner, J., and S. Wiemer, 2005, Assessing the quality of earthquake catalogues: Estimating the magnitude of completeness and its uncertainty, *Bull. Seismol. Soc. Am.*, 95, no. 2, 684–698, doi: 10.1785/0120040007.
- Wright, T. J., N. Houlié, M. Hildyard, and T. Iwabuchi, 2012, Real-time, reliable magnitudes for large earthquakes from 1 Hz GPS precise point positioning: The 2011 Tohoku-Oki (Japan) earthquake, *Geophys. Res. Lett.*, 39, no. 12, n/a-n/a, doi: 10.1029/2012GL051894.
- Wu, Y. M., and H. Kanamori, 2008, Development of an earthquake early warning system using real-time strong motion signals, *Sensors*, doi: 10.3390/s8010001.
- Wu, Y. M., and H. Kanamori, 2005, Experiment on an onsite early warning method for the Taiwan early warning system, *Bull. Seismol. Soc. Am.*, doi: 10.1785/0120040097.
- Wu, Y. M., H. Y. Yen, L. Zhao, B. S. Huang, and W. T. Liang, 2006, Magnitude determination using initial P waves: A single-station approach, *Geophys. Res. Lett.*, 33, no. 5, doi: 10.1029/2005GL025395.
- Wyss, M., C. G. Sammis, R. M. Nadeau, and S. Wiemer, 2004, Fractal dimension and b-value on creeping and locked patches of the San Andreas fault near Parkfield, California, *Bull. Seismol. Soc. Am.*, 94, no. 2, 410–421, doi: 10.1785/0120030054.
- Yamada, M., and J. Mori, 2009, Using  $\tau_c$  to estimate magnitude for earthquake early warning and effects of near-field terms, *J. Geophys. Res. Solid Earth*, 114, no. 5, B05301, doi: 10.1029/2008JB006080.
- Yoon, C. E., N. Yoshimitsu, W. L. Ellsworth, and G. C. Beroza, 2019, Foreshocks and Mainshock Nucleation of the 1999 M w 7.1 Hector Mine, California, *Earthquake, J. Geophys. Res. Solid Earth*, 124, no. 2, 1569–1582, doi: 10.1029/2018JB016383.
- Zaliapin, I., and Y. Ben-Zion, 2016, Discriminating characteristics of tectonic and human-induced seismicity, *Bull. Seismol. Soc. Am.*, 106, no. 3, 846–859, doi: 10.1785/0120150211.
- Zaliapin, I., and Y. Ben-Zion, 2013, Earthquake clusters in southern California I: Identification and stability, *J. Geophys. Res. Solid Earth*, 118, no. 6, 2847–2864, doi: 10.1002/jgrb.50179.
- Zaliapin, I., A. Gabrielov, V. Keilis-Borok, and H. Wong, 2008, Clustering analysis of seismicity and aftershock identification, *Phys. Rev. Lett.*, 101, no. 1, doi: 10.1103/PhysRevLett.101.018501.

## 6. References

- Zhao, C., and J. X. Zhao, 2019, S- and P-wave spectral ratios for on-site earthquake early warning in Japan, *Bull. Seismol. Soc. Am.*, 109, no. 1, 395–412, doi: 10.1785/0120180116.
- Zollo, A., O. Amoroso, M. Lancieri, Y. M. Wu, and H. Kanamori, 2010, A threshold-based earthquake early warning using dense accelerometer networks, *Geophys. J. Int.*, 183, no. 2, 963–974, doi: 10.1111/j.1365-246X.2010.04765.x.
- Zollo, A., S. Colombelli, L. Elia, A. Emolo, G. Festa, G. Iannaccone, C. Martino, and P. Gasparini, 2014, An Integrated Regional and On-Site Earthquake Early Warning System for Southern Italy: Concepts, Methodologies and Performances.

## Appendix

### Work done in STELTEL S.R.L.

As said, during the PhD I worked in STELTEL S.R.L. In fact, the very first title of my PhD project was “Design development and implementation of an embedded software and hardware system for Earthquake Early Warning”. The main aim of the project was the realization and the testing of a low-cost seismic station embedded with a digitizer. This all-in-one station should be able to analyze in real-time the data from two different sensors, an accelerometer, and a velocimeter, always included in the station. Another important goal for the project was the realization of an app capable to alert the user of the incoming shaking in an Early Warning framework. On the other hand, the research objectives were the development of innovative Earthquake Early Warning techniques.

Despite the project was well structured, when the PhD started most of the work on the station and on the app was already done. In particular, the all-in-one station was been already designed, built, and partially tested on the field. Moreover, the app was also already in development and then presented in the paper Colombelli et al. (2020).

So, my work in STELTEL has been mainly focused on stress tests and hardware debug of the seismic station. On the other hand, we updated and improved the software of the system. One important improvement of the software of the embedded station is the implementation of an EEW system, SAVE (on-Site Alert level; Caruso et al., 2017). The procedure is able to analyze the data stream in real-time, and to pick upcoming transient. After the pick, the system measures two P-wave parameters:  $P_d$  and  $\tau_c$ . Then, using scaling laws, the method can predict PGV at the target (from  $P_d$ ) and the magnitude of the event (from  $\tau_c$ ). Moreover, the system predicts the macroseismic intensity ( $I_M$ ) from PGV. In the end, given  $M$  and  $I_M$ , the system issues an alert with 4 different intensities: 0, low magnitude ( $M < 5$ ) event with low intensity ( $I_M < VI$ ); 1, strong event ( $M \geq 5$ ) with low intensity; 2, low magnitude event with high intensity ( $I_M \geq VI$ ); 3, high magnitude event with high intensity.

Another work done in STELTEL S.R.L. is the implementation, in an operative version of SAVE, of the procedures developed in Iaccarino et al. (2020) (Chapter 2). So, we included in the system a module for the prediction of the RSA for nine different periods with the relations obtained in the work. The updated system is also able to provide the real values for RSA after the event ended.

## Curriculum vitae

**Name:** Antonio Giovanni Iaccarino

### CURRENT POSITION

- From 01/01/2018: Phd candidate in Structural Engineering, Geotechnics, and Seismic Risk at Università di Napoli “Federico II” with project: “Design, development and implementation of an embedded hardware-software system for Earthquake Early Warning”. Tutor: Prof. Matteo Picozzi

### DEGREES

- 10/19/2016: Master’s degree in Physics, Università di Napoli “Federico II”. Mark: 107/110. Thesis: “Resolution of the back-projection methods from synthetic tests: application to Tohoku-Oki earthquake, March 11, 2011”. Tutor: Gaetano Festa.
- 10/24/2014: Bachelor’s Degree in Physics, Università di Napoli “Federico II”. Mark: 99/110. Titolo: “Modelli complessi di sorgente sismica per il terremoto de L’Aquila”. Tutor: Gaetano Festa.

### PUBLICATIONS

1. Iaccarino, A. G., M. Picozzi, D. Bindi, and D. Spallarossa, 2020, Onsite Earthquake Early Warning: Predictive Models for Acceleration Response Spectra Considering Site Effects, *Bull. Seismol. Soc. Am.*, 110, no. 3, 1289–1304, doi: 10.1785/0120190272.
2. Festa, G. et al., 2021, Insights into Mechanical Properties of the 1980 Irpinia Fault System from the Analysis of a Seismic Sequence, *Geosciences*, 11, no. 1, 28, doi: 10.3390/geosciences11010028.
3. Picozzi, M., and A. G. Iaccarino, 2021, Forecasting the Preparatory Phase of Induced Earthquakes by Recurrent Neural Network, *Forecasting*, 3, no. 1, 17–37, doi: 10.3390/forecast3010002.
4. Iaccarino, A. G., P. Gueguen, M. Picozzi, and S. Ghimire, 2021, Earthquake Early Warning System for Structural Drift Prediction Using Machine Learning and Linear Regressors, *Front. Earth Sci.*, 9, doi: 10.3389/FEART.2021.666444.

### CONFERENCE PARTICIPATIONS

1. Iaccarino, A. G., M. Picozzi, D. Bindi, and D. Spallarossa, 2019, Onsite Earthquake Early Warning: Predictive Models for Acceleration Response Spectra Including Site-Effects, in AGU Fall Meeting Abstracts. <https://ui.adsabs.harvard.edu/abs/2019AGUFM.S52B..01I>
2. Iaccarino, A. G., Picozzi, M., Bindi, D., and Spallarossa, D.: Onsite Earthquake Early Warning: Predictive Models for Acceleration Response Spectra Considering Site-Effects, EGU General Assembly 2020, Online, 4–8 May 2020, EGU2020-8939, <https://doi.org/10.5194/egusphere-egu2020-8939>, 2020
3. Iaccarino, A. G. and Picozzi, M.: Forecasting the Preparatory Phase of Induced Earthquakes by Recurrent Neural Network, EGU General Assembly 2021, online, 30 Apr 2021, EGU21-4321, <https://doi.org/10.5194/egusphere-egu21-4321>, 2021.

## Appendix

4. Iaccarino, A. G., Gueguen P., Picozzi M., and Ghimires S.: Earthquake Early Warning System for Structural Drift Prediction using Machine Learning and Linear Regressors. 37th General Assembly of the European Seismological Commission 2021, online. **Accepted abstract.**

## TECHNIQUE SKILLS

I started to work on Seismology during the bachelor's degree in Physics. In particular, during the writing of the thesis, I improved my programming skills with Matlab.

During the master's degree, I participated to training activities within the RISSCLab research group into the Physics Department at Università di Napoli "Federico II" under the supervision of professors Aldo Zollo and Gaetano Festa. Many of these activities involved the analysis of seismic waveforms recorded at ISNet (Irpinia Seismic Network, <http://isnet.fisica.unina.it/>). During the training many technical programs have been used (i.e., SAC, PQL, SeisGram).

As part of the course "Physics Laboratory", under the supervision of the Prof. Gaetano Festa, I participated to the RICEN (Repeated InduCed Earthquakes and Noise, <http://www.rissclab.unina.it/it/esperimenti/670-ricen-experiment>) experiment into the Solfatara crater, in Pozzuoli, Napoli. During this experiment and the following RICEN data analysis, I used several tools such as, NLLoc (Non-Linear Location) and Matlab.

As part of the course "Applied Geophysics", under the supervision of Prof. Domenico Patella, I took part to many small experiments consisting in field measurement of geoelectrical exploration and magnetotellurics tomography.

During the writing of the Master's Thesis, I improved my skills in Matlab and learnt the use of AXITRA.

During the PhD course, I experienced the use of programming tools such as R and Python, implementing statistical analysis and machine learning techniques.

## LANGUAGE SKILLS

English: excellent reading and writing skills, good verbal skills.

Certificate: Cambridge English Certificate, level C1-B